Master's thesis

NTNU
Norwegian University of Science and Technology

Eirik Ishol Skogan

# Modelling and Safety-based Path Planning of Fixed-Wing Unmanned Aerial Vehicle in Icing Conditions

Master's thesis in Cybernetics and Robotics
Supervisor: Kristoffer Gryte
Co-supervisor: Tor Arne Johansen
June 2023

NTNU
Norwegian University of
Science and Technology

Eirik Ishol Skogan

# Modelling and Safety-based Path Planning of Fixed-Wing Unmanned Aerial Vehicle in Icing Conditions

Master's thesis in Cybernetics and Robotics
Supervisor: Kristoffer Gryte
Co-supervisor: Tor Arne Johansen
June 2023

Norwegian University of Science and Technology

NTNU
Norwegian University of
Science and Technology

# Modelling and Safety-based Path Planning of Fixed-Wing Unmanned Aerial Vehicle in Icing Conditions

Eirik Ishol Skogan

June 9, 2023

Supervisor: Kristoffer Gryte
Co-supervisor: Tor Arne Johansen

Norwegian University of Science and Technology
Faculty of Information Technology and Electrical Engineering
Department of Engineering Cybernetics

Master thesis

# Abstract

As Unmanned Aerial Vehicles (UAVs) continue to rise in popularity, their range of applications expands. Challenges associated with operating in harsh weather conditions, particularly icing, arise along with new applications and stricter reliability demands. This thesis confronts this concern by developing a comprehensive mathematical model of a specific fixed-wing UAV named Falk, which includes the effects of icing on aerodynamics and weight distribution.

The Falk model is simulated in different icing scenarios: no ice, iced wing, iced tail, and fully iced (both wing and tail iced) in various icing conditions. The icing conditions are primarily determined by temperature, liquid water content (LWC) in the air, and water droplet size (MVD). Various weather conditions contribute to the accretion of different ice formations. This study focuses on understanding how different ice formations affect the UAV's flight performance and stability. From pitch and roll step responses, the model's limitations due to ice accumulation are investigated, particularly control surface saturation. The study finds that in a pitch maneuver, distinct ice formations affect performance significantly differently. In some conditions, ice only on the tail reduces the stability margins the most, while in others, ice on the wing and tail is the most serious. Most importantly, in very severe icing conditions, the elevator will go into saturation.

The rolling step is done in a steady coordinated turn to maintain altitude. In such turn is an iced tail most influential and can lead to sudden aileron saturation and instabilities. Interestingly, ice on just the wing leads to less reduction of control surface saturation margins. However, an iced wing significantly increases drag and propulsion power. The pitch and roll maneuvers in icing conditions underscore the complexity of ice formations and flight dynamics.

The model is then integrated into a path planner that utilizes a Rapidly-exploring Random Tree algorithm, specifically the RRT* algorithm. The planner aims to find a near-optimal, energy-effective path that limits exposure to icing conditions and avoids any icing hazards. It also considers winds, which significantly affect flight performance. Additional capabilities like obstacle avoidance and terrain following are incorporated into the planner. The resulting path is the most cost-effective that is safe to fly without the use of an ice protection system (IPS). The path planner is limited to the fact that there must be a feasible path that does not violate any constraints. Further work on implementing IPS will expand the versatility of the path planner.

The path planner is tested in both artificial and real-world environments, demonstrating its ability to avoid icing hazards and find a safe path. While the planner is still in a conceptual phase, it shows considerable potential for further development and application. This research provides valuable insights into addressing icing problems in UAV operation, promoting safety and efficiency in a growing field.

# Sammendrag

Etter hvert som ubemannede luftfartøyer (UAV) fortsetter å øke i popularitet, utvides bruksområdet deres. Utfordringer knyttet til operasjoner under harde værforhold, spesielt ising, dukker opp sammen med nye bruksområder og strengere krav til pålitelighet. Denne avhandlingen konfronterer disse utfordringene ved å utvikle en omfattende matematisk modell av en spesifikk fastvinget UAV, kalt Falk, som inkluderer påvirkningen av ising på aerodynamikk og vektfordeling.

Falk-modellen er simulert i forskjellige isingsscenarier: ingen is, iset vinge, iset hale og fullt iset (både vinge og hale er iset) under ulike isingsforhold. Isingsforholdene bestemmes først og fremst av temperatur, absolutt luftfuktighet (LWC) og vanndråpestørrelse (MVD). Ulike værforhold bidrar til akkumulering av forskjellige isformasjoner. Fokuset i denne studien er å forstå hvordan ulike isdannelser påvirker Falks flyegenskaper og stabilitet. Fra stamp og rull sprangresponser undersøkes modellens begrensninger på grunn av isakkumulering, spesielt kontrollflatemetning. Studien finner at i en stampmanøver påvirker distinkte isdannelser flyegenskapene betydelig forskjellig. I noen forhold kan is kun på halen redusere stabilitetsmarginene mest, mens i andre er is på vingen og halen mest alvorlig. Viktigst av alt, under svært alvorlige isforhold vil høyderoret gå i metning.

Spranget i rull gjøres i en koordinert sving for å opprettholde høyden. I en slik sving er en isete hale mest innflytelsesrik på flyegenskapene, og kan føre til plutselig metning av balanseroret og dermed ustabiliteter. Interessant nok fører is på bare vingen til mindre reduksjon av styrerorenes metningsmarginer. En iset vinge øker imidlertid luftmotstanden og dermed energiforbruket betydelig. Stamp og rull-manøvrene under isingsforhold understreker kompleksiteten til isdannelser og flydynamikk.

Modellen blir deretter integrert i en baneplanlegger som bruker en Rapidly-exploring Random Tree-algoritme, nærmere bestemt RRT* algoritmen. Planleggeren tar sikte på å finne en nesten optimal, energieffektiv bane som begrenser eksponeringen for isforhold og unngår farer forårsaket av ugjestmildt vær. Den tar også hensyn til vind, som påvirker flyegenskapene betydelig. Ytterligere funksjoner som unngåelse av hindringer og terrengfølging er integrert i planleggeren. Resultatet fra baneplanleggeren er den mest energieffektive banen som er trygg å fly uten bruk av et avisingssystem (IPS). Store områder med isende forhold kan begrense baneplanleggeren på den måten at den ikke kan finne en gjennomførbar bane. Videre arbeid med å implementere en avisingsmodell vil utvide bruksområdet til baneplanleggeren.

Baneplanleggeren er testet i både kunstige og virkelige miljøer, og den demonstrerer sin evne til å unngå isingsfarer og finne en sikker bane. Mens planleggeren fortsatt er i en konseptuell fase, viser den et betydelig potensial for videreutvikling og anvendelser. Denne avhandlingen gir verdifull innsikt i isingsproblematikken hos UAVer, og fremmer sikkerhet og effektivitet i et voksende bruksområde.

# Preface

My five-year-long educational adventure at the Norwegian University of Science and Technology (NTNU) ends with this thesis. The educational journey started with a Bachelor's degree in Automation, and then progressed to a Master's degree in Cybernetics and Robotics. Luckily, I've had the opportunity to focus my final studies on a topic that has always fascinated me, Unmanned Aerial Vehicles (UAVs). It has been exciting to tackle a real-world problem that is easily visualized.

This thesis extends a smaller project that I've worked on previously, the details of which are explained in the introduction. This previous experience on the topic gave me a satisfactory head start on my Master's thesis.

I want to give special honors to my main supervisor Kristoffer Gryte. He also supervised my previous project and has been an impressive help from the beginning, helping to guide the thesis in the right direction.

I'd also like to thank Markus Lindner for his strong support, especially when it came to understanding aerodynamics and how it's affected by icing. At the final sprint of the thesis, Tor Arne Johansen and Michael Cheung provided necessary assistance, for which they deserve the honor.

Eirik Ishol Skogan
June 9, 2023
Trondheim

# Contents

# Nomenclature

**Acronyms**

| | |
|---|---|
| AOA | Angle of Attack |
| CFD | Computational Fluid Dynamics |
| CG | Center of Gravity |
| HTP | Horizontal Tail Plane |
| LWC | Liquid Water Content |
| MET | Norwegian Meteorological Institute |
| MVD | Median Droplet Diameter |
| TWC | Total water collection |
| VTP | Vertical Tail Plane |
| W | Main Wing |

**Symbols**

| | |
|---|---|
| $(\overrightarrow{x}_b, \overrightarrow{y}_b, \overrightarrow{z}_b)$ | Body frame |
| $(\overrightarrow{x}_s, \overrightarrow{y}_s, \overrightarrow{z}_s)$ | Stability frame |
| $\alpha$ | Angle of Attack |
| $\bar{q}$ | Dynamic pressure |
| $\beta$ | Side slip angle |
| $\delta_a$ | Aileron deflection, positive when right aileron downward |
| $\delta_e$ | Elevator deflection, positive downward |
| $\delta_r$ | Rudder deflection, positive towards port side |
| $\epsilon_H$ | Downwash angle at HTP |
| $\epsilon_{s,\beta}$ | Sidewash gradient |
| $\eta_H$ | HTP trim angle wrt. $\overrightarrow{x}^b$ |
| $\eta_H$ | Ratio of dynamic pressure on HTP to the freestream dynamic pressure |
| $\Gamma$ | Main wing dihedral |
| $\kappa_\beta$ | Tail sidewash factor |
| $\kappa_\Gamma$ | Dihedral factor |
| $\kappa_b$ | Vortex span factor |

| | |
|---|---|
| $\kappa_l$ | Dihedral factor |
| $\kappa_p$ | Tail position factor |
| $\kappa_s$ | Wing sweep factor |
| $\kappa_v$ | Vortex strength factor |
| $\Lambda$ | Wing sweep angle |
| $\overrightarrow{P_G P_H}$ | Vector from $P_H$ to CG |
| $\overrightarrow{P_G P_W}$ | Vector from $P_W$ to CG |
| $\overrightarrow{P_H P_W}$ | Vector from $P_W$ to $P_H$ |
| $\rho$ | Air density |
| $\tau_\alpha$ | Downwash delay from main wing to HTP |
| $\zeta$ | Icing level |
| $A$ | Ice accumulation rate |
| $C_D$ | Drag coefficient |
| $c_H$ | HTP mean chord |
| $C_L$ | Lift coefficient |
| $C_m$ | Pitch moment coefficient |
| $C_P$ | Propeller power coefficient |
| $C_T$ | Propeller thrust coefficient |
| $c_W$ | Wing mean chord |
| $J$ | Propeller advance ratio |
| $P_H$ | HTP quarter chord point |
| $P_W$ | Wing quarter chord point |
| $R_A^W$ | Wing aspect ratio |
| $S_H$ | HTP surface area |
| $S_W$ | Wing surface area |
| $T_{i,max}$ | Maximum exposure time in icing condition |
| $V_a$ | Airspeed |
| b | Wing span |
| p | Roll rate |
| q | Pitch rate |
| r | Yaw rate |

**Subscripts**

| | |
|---|---|
| (n) | n'th element of vector |

# Chapter 1

# Introduction

Unmanned Aerial Vehicles (UAVs) are rapidly gaining popularity in numerous new sectors due to their mobility, low cost, and wide range of applications. They are used extensively in agriculture and forestry for crop and forest monitoring, logistics for delivery services, and transportation and energy sector for inspections. With an increasing application in search and rescue missions, UAVs make our lives safer and effortless. It should be noted that this is relevant only in the context of civilian applications. The progress of technology has sparked significant growth in the UAV industry and led to an intensive period of research and development in this industry.

One challenge that UAVs often face is operating in harsh weather conditions. Among the various adverse conditions that UAVs encounter is icing conditions, a particularly troublesome phenomenon. Ice accumulation can affect the aerodynamics and weight distribution of a UAV, potentially leading to loss of control [1]. Ice accumulation on the leading edge of airfoils can lead to a significant lift reduction and drag increase. The lift reduction can happen if the ice formations alter the airfoil's shape, disrupting the airflow over the airfoils [2]. Loss of aerodynamic lift can reduce stability and flight performance. Moreover, compensating for an additional drag due to ice requires more energy to maintain flight height and velocity.

One choice for handling ice accumulation is ice protection systems (IPS). These systems include anti-icing, designed to prevent ice accumulation, and de-icing, aimed at eliminating already accumulated ice. However, these systems demand an increase in energy consumption. Ideally, an understanding of how the ice affects the UAV and how much energy the IPS consumes is needed to optimize the problem of ice handling. Where on the UAV the ice accumulates can impact flight performance, affecting where it is essential to install an IPS.

Simulation is a beneficial tool to safely investigate the impact of icing on the UAV. Simulation allows for the examination of a variety of icing scenarios and icing formations without risking the actual UAV. However, reliable simulation requires a suitable mathematical model representing the physical UAV's characteristics and response with icing. This thesis aims to develop a mathematical model for a specific UAV. The UAV, called Falk, is a fixed-wing UAV with a wing span of 3.2m [3]. The comprehensive model design aims to capture the icing effects on aerodynamics and weight distribution. The modeling is a further work of a secondary task [4] done by the same author as this thesis. This secondary task found a clean (no ice) mathematical model of Falk using the CFD program XFLR5. Furthermore, this task

introduced ice into the static longitudinal coefficients of the wing, and executed some simulations for flight performance investigation.

In this thesis, the model will be extended considerably by using the lift reduction due to ice to calculate the most influential affections of ice on the static lateral coefficients and the longitudinal dynamic coefficients. The most critical control derivatives will also be modeled with regard to icing. Additionally, the weight of the ice will also be included in the inertia matrix of the model, which is essential when the dynamics are to be evaluated. Furthermore, a more dynamic calculation of downwash and sidewash will be implemented, together with an experimental processed propeller model from [5].

By using this model, flight in various icing conditions can be simulated to identify the model's performance and limitations for each icing condition. The primary focus of this study is to obtain insight into how ice accumulation affects Falk's performance and stability. The flight simulations will be done for four icing scenarios: clean (no ice), iced wing, iced tail, and fully iced. These scenarios can represent an IPS that handles airfoils individually.

The simulator that originated in [6] and was further developed by [7], [8], and [4] will be further improved in this thesis. The main improvements will include the ability to simulate flight with different ice structures. Simulating with different ice on the wing and tail will also be possible. Furthermore, the simulator will be able to use real-world weather data to determine some of the icing parameters. In addition, small functionalities will be added, such as controllers for steady-coordinated turn and altitude-hold.

Building on the development of the UAV model, this thesis will further delve into utilizing a path planner for efficient and safe flight. The path planner's objective is to find a safe flight path with the least energy consumption, executed without the need for an ice protection system. With icing conditions posing a significant challenge for UAV operations, the absence of an ice protection system can increase these operational difficulties. Therefore, a path planner that can effectively find a path around such hazardous conditions can be a valuable tool for UAV operations. Such a path planner must consider weather conditions, obstacles, and terrain when searching for paths. The work by Tiller [9] has laid the foundation for the acquisition of historical weather data that are used in this thesis, and Olsen's study [10] provides the fundamental groundwork for the implementation of an RRT* algorithm as path planner.

As a final confirmation, this thesis aims to investigate how ice affects the UAV Falk, and how a path planner can find a safe path for it in icing conditions.

## 1.1 Structure

The thesis consists of three parts:

1. *Falk Modeling and Simulation in Icing Conditions*. This part includes the development of the mathematical model and the results from simulations. The results are further discussed at the end of the part.
2. *Path Planning in Icing Conditions*. The development of the path planner is presented in this part. Further in this part is the path planner testing and discussion presented.
3. *Conclusion and Further Work*. Last are some concluding remarks and suggested further work presented.

# Part I

# Falk Modeling and Simulation in Icing Conditions

# Chapter 2

# Modeling Background Theory

This chapter presents the most important background theory essential to this first part of the thesis.

## 2.1 Previous work and contribution

This thesis is a continuation of a project assignment done earlier by the writing author [4]. The project assignment dealt with creating a simple longitudinal model for the Falk UAV with ice on the wing. In addition, the model was simulated to observe its flight performance. As an inspiration to the previously done modeling, is the master thesis of Gryte [6] used. Gryte developed a simulator to simulate his model of a completely different UAV than the Falk. Furthermore, there are several people who have contributed to further developing the simulator to be able to simulate models that contain icing. The work by Winter [11], Kleiven [7], and Högnadóttir [8] made a major contribution to the further development of the simulator. Together with the recent paper by Lindner [12] dealing with static analyses of Falk's iced airfoils, the basis for this thesis has been established.

This thesis has significantly expanded Falk's model, by the introduction of a highly comprehensive longitudinal and lateral model, along with a model of the propeller in icing conditions. To be clear, only the method of using a two-point model is similar to the modeling in the project assignment[4]. The simulator will become more advanced in this thesis by being able to simulate flight with different types of icing and a greater variety of maneuvers. The simulator has also been further developed to include real weather data obtained from the internet, as well as control the model in more useful trajectories.

## 2.2 Weather conditions

The accumulation of ice on UAVs is significantly influenced by several atmospheric conditions, most notably temperature, Liquid Water Content (LWC), and the Median Volumetric Diameter (MVD) of water droplets [12]. The analyses by Lindner in [12] depend on these parameters. Thus they are the most important parameters to understand before further reading.

### 2.2.1 Temperature

One of the most influential parameters for ice accretion is air temperature. When UAVs operate in temperatures below the freezing point of water, any liquid wa-

ter that the UAV encounters can freeze upon contact with the UAV's surfaces. The liquid water can be in the form of precipitation, fog, or cloud droplets. Supercooled liquid water droplets, those that remain liquid at temperatures below freezing, present a particular challenge. These droplets can rapidly freeze upon contact with the UAV, forming ice accretions [1]. Moreover, different temperatures create different ice formations, which makes the temperature such an influential parameter.

### 2.2.2 Liquid Water Content (LWC)

Liquid Water Content (LWC) is a measure of the mass of liquid water per unit volume of air, expressed typically in $g/m^3$ [13]. Higher LWC values often correspond to denser clouds or heavier precipitation. A greater quantity of liquid water in the air comes with a greater potential for water to freeze on the UAV.

### 2.2.3 Median Volume Diameter (MVD)

Median Volume Diameter (MVD) is a measure of the water droplet size. The water droplets are of various sizes in the air, also within small geometric volumes. The MVD captures the diameter where half of the droplets are smaller, and the other half are larger. In terms of icing, small droplets do have a lower possibility of hitting the UAV's airfoil compared to larger droplets. This is because smaller droplets have an easier time following the airflow that goes on the top and bottom of the airfoil.

## 2.3 Modelling the Flight Mechanics of UAVs

The modeling of a UAV can be efficiently achieved using a set of six equations. These equations are fundamentally constructed from three parts: aerodynamic forces and moments, propulsion forces and moments, and gravitational forces. This section will establish these equations of motion and further expand the conventional model to a more suitable two-point model. Furthermore, an iced propeller model will be presented.

### 2.3.1 Longitudinal and Lateral Perspectives of Flight Mechanics

When a UAV moves through the air, it experiences aerodynamic forces and moments. The design of a UAV exploits these forces and moments to controllable behave as desired, whether it is flying to a specific location or in circles for reconnaissance. Therefore, the equations of motion representing the model are crafted from an aerodynamic perspective.

Dividing the model into two groups, namely longitudinal and lateral, simplifies the model to the more intuitive. Figure 2.1 illustrates the body-axes in Falk, where the $x^b$-axis is called the longitudinal axis. This axis has its origin in the center of gravity and is parallel to a level fuselage. The drag and propulsion forces act along the longitudinal axis. Additionally, the $z^b$-axis is included in the longitudinal model, where the lifting force is composed along it and the pitching moment about it. The longitudinal and $z^b$-axis together make the longitudinal plane, which makes the UAV symmetrical about this plane.

The remaining side force along the $y^b$-axis, rolling moment about the $x^b$-axis, and yawing moment about $z^b$-axis makes the lateral model.

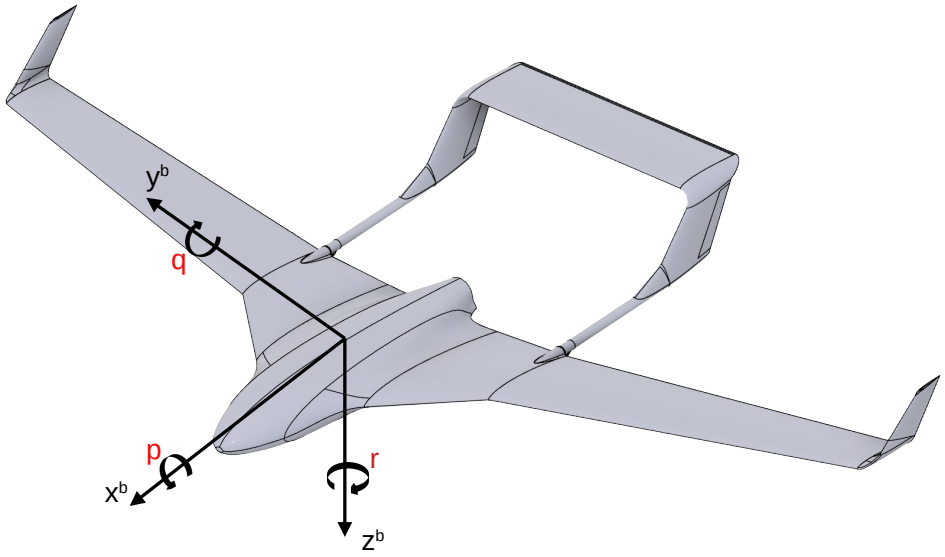


**Figure 2.1:** The Falk illustrated in the body-frame. Illustration from [4]

The mathematical representation of acting forces and moments can be quite complex and nonlinear, making them challenging to handle. As such, control engineers often find it beneficial to use a quasi-linear approximation to simplify these equations. The following equations represent the longitudinal model

$$L = \bar{q}S\left(C_L(\alpha) + C_{L_q}\frac{c}{2V}q + C_{L_{\delta_e}}\delta_e\right) \tag{2.1}$$

$$D = \bar{q}S\left(C_D(\alpha) + C_{D_q}\frac{c}{2V}q + C_{D_{\delta_e}}\delta_e\right) \tag{2.2}$$

$$m = \bar{q}Sc\left(C_m(\alpha) + C_{m_q}\frac{c}{2V}q + C_{m_{\delta_e}}\delta_e\right) \tag{2.3}$$

and the lateral model is represented by

$$Y = \bar{q}S\left(C_Y(\beta) + C_{Y_p}\frac{b}{2V}p + C_{Y_r}\frac{b}{2V}r + C_{Y_{\delta_a}}\delta_a + C_{Y_{\delta_r}}\delta_r\right) \tag{2.4}$$

$$l = \bar{q}Sb\left(C_l(\beta) + C_{l_p}\frac{b}{2V}p + C_{l_r}\frac{b}{2V}r + C_{l_{\delta_a}}\delta_a + C_{l_{\delta_r}}\delta_r\right) \tag{2.5}$$

$$n = \bar{q}Sb\left(C_n(\beta) + C_{n_p}\frac{b}{2V}p + C_{n_r}\frac{b}{2V}r + C_{n_{\delta_a}}\delta_a + C_{n_{\delta_r}}\delta_r\right) \tag{2.6}$$

where the dynamic pressure is $\bar{q} = \frac{1}{2}\rho V^2$.

These models are widely recognized in aircraft literature, for example, in [14], [15], and [16]. All the aerodynamic coefficients are denoted $C$ with a corresponding subscript. These coefficients characterize the model, and they must ensure that the model represents the physical aircraft in the best possible way. The coefficients are well structured in the models where the static coefficients come first, then the stability derivatives, and at last, the control derivatives. The static coefficients are recognized by the single subscript, the stability derivatives are recognized by the double subscript, and the control derivatives by the triple subscript. The longitudinal static coefficients are dependent on the angle of attack $\alpha$, while the lateral static coefficients on the sideslip angle $\beta$. The stability derivatives are multiplied by the angular rates and then represent the dynamics of the model. For instance, the coefficient $C_{m_q}$, called the pitch damping coefficient, does produce a restoring moment if it is a change in pitch and the coefficient is negative. Furthermore, the

control derivatives describe how control inputs affect the UAV's motion. For example, the elevator deflection's influence on the pitching moment is represented by $C_{m_{\delta_e}}$.

Understanding these models and coefficients is crucial, as they quantify the UAV's response to control inputs and disturbances. The understanding is also important when this model without ice is to be further developed to include ice.

### 2.3.2 Two-points longitudinal model

Decomposing of the longitudinal model is suitable for many purposes, for example, for simpler obtaining of aerodynamic coefficients. One method with no commonly recognized name in the community of aircraft modeling, hereafter named the two-point method, is a method for longitudinal decomposing. This method has been widely adopted in the flight dynamics community and is presented in many textbooks. This method is also used in [4]. The method's fundamental concept involves separating the wing from the empennage to compute their forces and moments independently. Furthermore, these isolated computations are integrated into a "two-point longitudinal model," where they are assembled into a full longitudinal model. The following structure, detailed in [17], is utilized to derive a longitudinal two-point model.

When separating the wing and empennage for modeling their forces and moments, it is important to take the change of AoA encountered by the horizontal tail plane (HTP) into account. The HTP AoA is affected by multiple factors, where the downwash from the wing is one factor. The downwash leads to a reduction of AoA at the HTP, subsequently resulting in a lift reduction [16]. The downwash term is a consequence of the main wing lift. Thus its modeling is dependent on the wing lift coefficient. As the lift generated by the wing can be well represented by a linear function well within stall angle, the downwash angle at the HTP, $\epsilon_H$, can be modeled linearly as well [16]. The downwash modeling is somewhat extensive and will be provided in the next section.

Another contribution to the HTP AoA is the relative positioning of the wing quarter chord point, $P_W$, and HTP quarter chord point, $P_H$, which is affected by the rotational pitch rate $q$. This pitch-rate-induced AoA to HTP is described by

$$\alpha_{dyn}^{H} = \arctan\left(\frac{q\,\overrightarrow{P_H P_W}\cdot\overrightarrow{x}^{s}}{V_a}\right) \tag{2.7}$$

Last is the HTP tilt angle, $\eta_H$, and longitudinal axis AoA, $\alpha$, affecting the HTP AoA as well. All these terms together sum the HTP AoA up to

$$\alpha_H = \alpha + \eta_H - \epsilon_H + \alpha_{dyn}^{H} \tag{2.8}$$

which is a necessary estimation for computing forces and moments at the HTP. When the forces from the wing and HTP is to be summed, the angle between the forces has to be taken into account. This angle is estimated by

$$\tilde{\alpha} = \alpha_{dyn}^{H} - \eta_H \tag{2.9}$$

Computation of forces and moments for the two separated parts are carried out with respect to $P_W$ and $P_H$, respectively. For deriving the final longitudinal equations of motion, the isolated forces and moments are transformed to the UAV

center of gravity (CG) and summed. The final longitudinal model equations in CG are then given by

$$\overrightarrow{L} = \left(L^W + L^H \cos(\tilde{\alpha}) + D^H \sin(\tilde{\alpha})\right) \frac{\overrightarrow{L}^W}{L^W} \tag{2.10}$$

$$\overrightarrow{D} = \left(D^W - L^H \sin(\tilde{\alpha}) + D^H \cos(\tilde{\alpha})\right) \frac{\overrightarrow{D}^W}{D^W} \tag{2.11}$$

$$\overrightarrow{M}_{@CG} = \overrightarrow{M}_{@P_W} + \overrightarrow{CG\,P_W} \times \left(\overrightarrow{L} + \overrightarrow{D}\right) \tag{2.12}$$

where the total moment at the wing quarter chord is described by

$$\overrightarrow{M}_{@P_W} = \overrightarrow{M}^W_{@P_W} + \overrightarrow{M}^H_{@P_H} + \overrightarrow{P_W P_H} \times \left(\overrightarrow{L}^H + \overrightarrow{D}^H\right) \tag{2.13}$$

and the lift, drag, and moment at the quarter chord point for the wing and HTP are computed by the following equations

$$\overrightarrow{L}^W = -\bar{q}\, S_W\, C_L^W(\alpha)\, \overrightarrow{z}_s \tag{2.14}$$

$$\overrightarrow{L}^H = -\bar{q}_H\, S_H\, C_L^H(\alpha_H)\, \overrightarrow{z}^H_s \tag{2.15}$$

$$\overrightarrow{D}^W = -\bar{q}\, S_W\, C_D^W(\alpha)\, \overrightarrow{x}_s \tag{2.16}$$

$$\overrightarrow{D}^H = -\bar{q}_H\, S_H\, C_D^H(\alpha_H)\, \overrightarrow{x}^H_s \tag{2.17}$$

$$\overrightarrow{M}^W_{@P_W} = \bar{q}\, S_W\, c_W \left(C^W_{m@P_W}(\alpha) + C^W_{m_q@P_W}\, \frac{c_W}{2\, V_a}\, q\right) \overrightarrow{y}_s \tag{2.18}$$

$$\overrightarrow{M}^H_{@P_H} = \bar{q}_H\, S_H\, c_H \left(C^H_{m@P_H}(\alpha_H) + C^H_{m_q@P_H}\, \frac{c_H}{2\, V_a^H}\, (q + \dot{\eta}_H)\right) \overrightarrow{y}^H_s \tag{2.19}$$

It is reasonable to assume that the airspeed is equal for the HTP and wing, thus $V_a^H = V_a$. Furthermore, it is assumed that the dynamic pressure is equal at the two points, $\bar{q}^H = \bar{q}$.

### 2.3.3 Downwash

The downwash angle at HTP, $\epsilon_H$, can be written as [16]

$$\epsilon_H = \frac{\kappa_v\, \kappa_p\, \kappa_s}{\kappa_b} \frac{C_L^W}{R_A^W} \tag{2.20}$$

where all variables depend on the geometry of the aircraft. Therefore is, this equation quite straightforward when used on an existing wing. All $\kappa$'s are factors that show the wing in question is related to an elliptic wing with no sweep, dihedral, or twist. It is more simple to calculate the aerodynamic equations for an elliptic wing, and then the factors can be used to determine the aerodynamics of the wing in question. The vortex strength factor, $\kappa_v$, is a ratio of the wingtip vortex strength generated by an elliptic wing with the same lift coefficient and aspect ratio. $\kappa_b$ is the vortex span factor, which is determined by dividing the wingtip vertices spacing by the wing span. By knowing the wing taper ratio and aspect ratio, these factors are easily found with table lookup in [16]. It is important to note that these tables do not apply to swept wings, and according to [16], no closed-form solution for these factors has ever been obtained.

The downwash angle at the tail is influenced by the position of the tail relative to the wing. The tail position factor, $\kappa_p$, takes this position into account, along with

the wing planform shape. This factor is given by

$$\kappa_p = \frac{2\kappa_b^2}{\pi^2(\bar{y}^2+\kappa_b^2)}\left(1+\frac{\bar{x}(\bar{x}^2+2\bar{y}^2+\kappa_b^2)}{(\bar{x}^2+\bar{y}^2)\sqrt{\bar{x}^2+\bar{y}^2+\kappa_b^2}}\right) \tag{2.21}$$

where

$$\bar{x} = \frac{\overrightarrow{P_W P_{H(1)}}}{b/2}\,, \quad \bar{y} = \frac{\overrightarrow{P_W P_{H(3)}}}{b/2}\,, \quad \bar{z} = \frac{\overrightarrow{P_W P_{H(2)}}}{b/2} \tag{2.22}$$

For sweep compensation, the wing sweep factor, $\kappa_s$, is introduced. This factor depends on the wing planform shape, position of the tail, and wing sweep angle, $\Lambda$. This factor is given by

$$\kappa_s = \frac{1+\dfrac{\bar{x}-\bar{s}}{\bar{t}}+\dfrac{\bar{x}(\bar{r}+\bar{t})(\bar{t}_0^2-\bar{x}^2)}{\bar{r}\bar{t}(\bar{r}\bar{t}+\bar{r}^2-\bar{x}\bar{s})}}{1+\dfrac{\bar{x}(\bar{r}^2+\bar{t}_0^2-\bar{x}^2)}{\bar{r}^2\bar{t}_0}} \tag{2.23}$$

where

$$\bar{r} = \sqrt{\bar{x}^2+\bar{y}^2} \tag{2.24}$$

$$\bar{s} = \kappa_b \tan\Lambda \tag{2.25}$$

$$\bar{t} = \sqrt{(\bar{x}-\bar{s})^2+\bar{y}^2+\kappa_b^2} \tag{2.26}$$

$$\bar{t}_0 = \sqrt{\bar{x}^2+\bar{y}^2+\kappa_b^2} \tag{2.27}$$

### 2.3.4 Sidewash

Notationally, is the sidewash gradient defined according to [16] as

$$\epsilon_{s,\beta} \equiv \frac{\partial \epsilon_s}{\partial \beta} \tag{2.28}$$

Moreover, can the sidewash gradient induced at an arbitrary point in space be estimated by

$$\frac{\partial \epsilon_s}{\partial \beta}(\bar{x},\bar{y},0) = -\frac{\kappa_v \kappa_\beta}{\kappa_b}\frac{C_L^W}{R_A^W} \tag{2.29}$$

where the tail sidewash factor, $\kappa_\beta$, as all other $\kappa$-variables, depends on the geometry of the aircraft. It is the planform shape of the wing and the position of the tail relative to the wing that determines the value of $\kappa_\beta$, which is expressed by

$$\begin{aligned}\kappa_\beta(\bar{x},\bar{y},0) = {} & \frac{4\bar{y}(\bar{x}-\kappa_b\tan\Lambda)\kappa_b^2}{\pi^2(\bar{y}^2+\kappa_b^2)^2}\left[1+\frac{\bar{x}-\kappa_b\tan\Lambda}{\sqrt{(\bar{x}-\kappa_b\tan\Lambda)^2+\bar{y}^2+\kappa_b^2}}\right] \\ & +\frac{2\,\bar{y}\,\kappa_b}{\pi^2(\bar{y}^2+\kappa_b^2)}\left[\frac{(\bar{x}-\kappa_b\tan\Lambda)^2\kappa_b}{\left[(\bar{x}-\kappa_b\tan\Lambda)^2+\bar{y}^2+\kappa_b^2\right]^{3/2}}\right]\end{aligned} \tag{2.30}$$

### 2.3.5 Propeller model

A study done by Nicolas Müller focuses on developing a fixed-wing UAV propeller model to estimate propeller performance in clean and icing conditions [5]. The

study is based on experimental data from icing wind tunnel tests. The propeller model is composed of three submodels that are based on clean performance, ice accretion, and iced performance. Using a second-order polynomial approximation, the model calculates the correlation between thrust, thrust coefficients, and advance ratio. The same applies to calculating the correlation between power, power coefficients, and advance ratio. In addition, the model does account for ice shedding.

The propeller used in the study is Mejzlik 21x13 2B E, with a radius of 0.53m and pitch of 0.33m.

**The clean performance model** is based on the general equations for evaluating propeller performance. Müller uses [18] to calculate the thrust, where the thrust coefficient $C_T$ is defined as a non-dimensional value obtained from the thrust $T$, the rotation speed $n$, the propeller diameter $d$, and the air density $\rho$. The coefficient is expressed as

$$C_T = \frac{T}{\rho n^2 d^4} \tag{2.31}$$

In aeronautics, the advance ratio $J$ is a useful non-dimensional quantity for propeller theory. The quantity describes the relationship between the forward airspeed of the propeller $V_\infty$ and the rotation speed.

$$J = \frac{V_\infty}{n\,d} \tag{2.32}$$

A propeller used as a propulsion propeller in a UAV will, for instance, have a low advance ratio during take-off since the forward airspeed is low and the rotation speed high.

The advance ratio can be used to derive the thrust coefficient in eq. 2.31. Coates' work in modeling the propulsion system for small fixed-wing UAVs [19] has results that show that the thrust coefficient can be approximated by a second-order polynomial as

$$C_T(J) = C_{T,0} + C_{T,1}J + C_{T,2}J^2 \tag{2.33}$$

where $C_{T,0}$, $C_{T,1}$ and $C_{T,2}$ are parameters found by wind tunnel tests.
When it comes to calculating the propeller power coefficient is Müller using the equation

$$C_P = \frac{P}{\rho n^3 d^5} \tag{2.34}$$

which is similar to the thrust coefficient that comes from [18]. Furthermore, does Coates model the power coefficient [19] as

$$C_P(J) = C_{P,0} + C_{P,1}J + C_{P,2}J^2 \tag{2.35}$$

which also is similar to the modeling of the thrust coefficient. $C_{P,0}$, $C_{P,1}$ and $C_{P,2}$ are parameters found by wind tunnel tests.

**The ice accretion model** estimates the impact of ice accretion on performance. To do this, Müller introduce temperature $T$, icing time $t$, liquid water content ($LWC$) and median droplet diameter ($MVD$) in the calculation of thrust and power coefficients

$$C_{T,\text{ice}} = C_T(T, t, LWC, J, MVD) \tag{2.36}$$

$$C_{P,\text{ice}} = C_P(T, t, LWC, J, MVD) \tag{2.37}$$

The physical ice accretion is modeled as an icing quantity called total water collection ($TWC$). This quantity will influence the thrust and power coefficients, which will be shown later. $TWC$ factors in the variables time $t$, $TWC$ and $\omega$, and is expressed as

$$TWC = t\ LWC\ n\ \frac{d}{2} \tag{2.38}$$

An important aspect of icing on propellers is icing shedding. This is a process where accumulated ice on the propeller breaks off the propeller. The break-off occurs when the forces acting on the ice, such as centrifugal force and aerodynamic forces, overcome the adhesion and cohesion force holding the ice to the propeller's surface. The maximum total water collection ($TWC$) before ice shedding is therefore dependent on maximum adhesion force $A_{\max}$ and rotation speed $n$, and is expressed as

$$TWC_{\max} = \frac{A_{\max}}{\frac{d}{2}\,n^2} \tag{2.39}$$

The maximum adhesion force $A_{\max}$ varies with surface roughness, temperature, and ice shape. In Müllers' study, the surface roughness was assumed constant through all experiments. Furthermore, the ice shape dependency is included in the temperature dependency since temperature and ice shape correspond. Hence, the maximum adhesion force is modeled as

$$A_{\max}(T) = A_{\max,0} + A_{\max,1}\,T^2 \tag{2.40}$$

where $A_{\max,0}$ and $A_{\max,1}$ are parameters found by icing wind tunnel tests.

**The ice performance degradation** is modeled by a factor $\Delta C_T(T)$ that is dependent of the temperature. The performance degradation is expressed as

$$\Delta C_T(T) = \Delta C_{T,0} + \Delta C_{T,1}T + \Delta C_{T,2}T^2 \tag{2.41}$$

where $\Delta C_{T,0}$, $\Delta C_{T,1}$ and $\Delta C_{T,2}$ are parameters found by icing wind tunnel tests.

**As a final result**, is the thrust coefficient equation given by

$$C_T(T, TWC) = C_T(J) \cdot (1 + \min(TWC, TWC_{\max}) \cdot \Delta C_T(T)) \tag{2.42}$$

Similarly, the power coefficient equation is given by

$$C_P(T, TWC) = C_P(J) \cdot (1 + \min(TWC, TWC_{\max}) \cdot \Delta C_P(T)) \tag{2.43}$$

where

$$\Delta C_P(T) = \Delta C_{P,0} + \Delta C_{P,1}T + \Delta C_{P,2}T^2 \tag{2.44}$$

## 2.4 CFD programs

### 2.4.1 XFLR5

XFLR5 is an easy-to-use computational fluid dynamics (CFD) analysis tool designed specifically for UAVs operating in conditions of low Reynolds numbers. Given that most UAVs, including Falk, operate at low Reynolds numbers [1], tools like XFLR5 become valuable. Using information about a UAV's airfoil shape, 3D model, and weight distribution as input, XFLR5 is able to determine the aerodynamic coefficients for a model. Its analyses are fast to execute and fast to evaluate. The program also estimates the inertia of the model. Notably, it is limited to analyses without ice.

### 2.4.2 Ansys FENSAP-ICE

Ansys FENSAP-ICE is one of the most sophisticated and capable CFD analysis tools available today. The software is engineered to conduct CFD analyses on intricate structures, even ice structures accumulated on airfoils. Operating this program necessitates a comprehensive foundational understanding and extensive training because of its complexity. One of the crucial requirements of FENSAP-ICE is the substantial computational power it demands its analyses. This aspect significantly restricts the scope of analyses that can be executed when utilizing a standard computer.

Despite these challenges, the exceptional analytical capabilities offered by Ansys FENSAP-ICE make it a valuable tool in the domain of aerodynamics and icing studies.

## 2.5 Simulation

An effective and extensive simulation is necessary for assessing a UAV model's performance, especially when the model is to be simulated in various weather conditions. The simulator used in this thesis takes the model equation, model coefficients, environmental parameters, icing level, and other data as input, and then returns UAV model states.

The simulator has been developed in Matlab, a high-level language that offers functionalities that are particularly suited to control systems design, which is crucial in UAV simulations. Additionally, the simulations are executed in Simulink, a simulation program made for combination with Matlab. This program makes simulation and analysis of dynamic systems, such as UAVs in flight, efficient and thorough.

The development of this simulator is a cumulative effort of several contributors, where each has independently continued the work, including the author of this thesis. It has been an iterative process that has transformed the simulator into a specialized tool for UAV simulation in icing weather conditions. The simulator takes into account various factors to accurately represent the UAV's behavior in given weather conditions. The inputs to this simulator include model equations and coefficients, which provide the mathematical foundation for the UAV's motion. Furthermore, the simulator considers icing level, a parameter that will be explained later, which significantly impacts the UAV's performance by altering its aerodynamics. Weather data like wind speed, direction, and turbulence, together with air temperature, LWC, and humidity, provide the environmental context.

The main output from the simulator is the states of the UAV model. Moreover, data can be analyzed in more detail by looking at specific forces and moments, as well as how the ice affects specific parts of the aircraft's dynamics. This is just a selection of the capabilities of the simulator.

### 2.5.1 Simulator structure

The structure of the simulator is illustrated in figure 2.2. Each block is explained below.

**Control**. This block represents the control system consisting of several PID controllers. They are designed to manage the pitch, roll, yaw, and motor reference signals to control the UAV model to desired attitude. Moreover, these reference

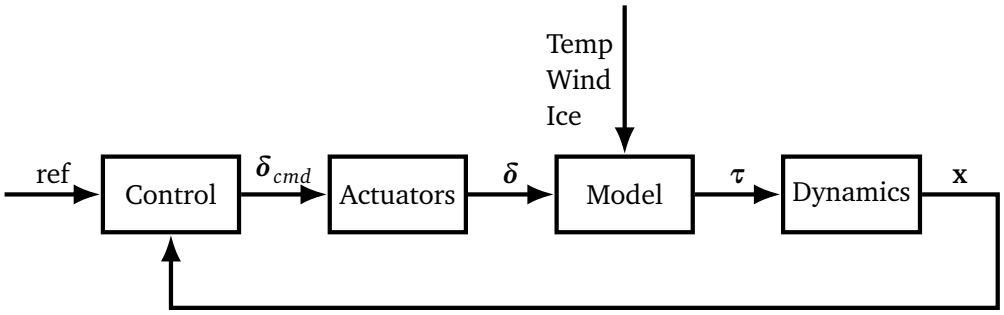


**Figure 2.2:** Block diagram representing an overview of simulator structure

signals are calculated by outer loop controllers, such as altitude, sideslip, or path-following guidance controllers. There is an intricate interplay among these controllers, working together to maintain the stability of the UAV and guide its path. The PID controllers have been approximately tuned to provide reasonable control and performance.

**Actuators**. Actuators are the components that convert the controller commands into physical motion. They are the control surfaces aileron, elevator, and rudder, together with the motor for generating thrust. The control surface dynamics are gained by feeding the commanded control signal through a second-order filter, as done by Gryte [6]

$$\frac{\delta_{actual}}{\delta_{cmd}} = \frac{\omega_0^2}{s^2 + 2\zeta\omega_0 s + \omega_0^2}$$

where the parameters are chosen to be $\omega_0 = 100\text{rad/s}$ and $\zeta = \frac{\sqrt{2}}{2}$. Gryte was inspired by [20] in the actuators modeling. Together with the dynamics is the actuator deflection limit important to include in the simulator. When a control surface reaches its deflection limit, it is said to be in a state of saturation. The specific saturation points for Falk's control surfaces are found in A.1.

**Forces and moments**. The UAV is represented in the simulator by a mathematical model. This model includes equations that describe the UAV's motion. For a clean model without ice, are equations (2.1-2.6) suitable. These equations are based on the forces and moments acting on the UAV. These forces and moments come from the aerodynamic lifts and drags, the actuators, or the environment, such as winds. An essential feature in this block is the inclusion of ice, a crucial factor when considering UAV forces and moments. The effect of ice accumulation on the aerodynamics and performance of the UAV is included in the model.

**Dynamics**. The dynamics block in the simulator is responsible for computing the states of the UAV model based on the forces and moments calculated in the model block. This computation is derived from fundamental principles of dynamics from [21], and is further described in [6]. The states include information about the position, velocity, and orientation of the UAV.

### 2.5.2 Icing

In the simulator, icing is represented in the model coefficients. These coefficients express the flight stability and dynamics of the UAV. As icing occurs, these coefficients change. Thus the stability and dynamics change. Every static longitudinal coefficient correlates with a specific AoA, and every static lateral coefficient corresponds to a sideslip angle. In [11] there is a proposed technique to use interpolation between the angles, aiming to obtain coefficients across the entire span

of angles.

Furthermore, as the coefficients are only available as fully clean or fully iced, a technique proposed in [7] introduces an icing parameter, denoted as $\zeta$, ranging between 0 and 1. This parameter quantifies the degree of icing, where $\zeta = 0$ represents no icing, and $\zeta = 1$ represents fully iced. Any value in between these extremes provides a measure of the degree of icing. The aerodynamic coefficients are calculated with respect to the icing parameter as

$$C_k(\zeta) = \zeta\, C_{k,\text{iced}} + (1-\zeta)\, C_{k,\text{clean}}\,, \quad k \in \{L, D, Y, l, m, n\} \tag{2.45}$$

# Chapter 3

# Falk Model in Icing Conditions

A mathematical Falk model is essential for accurately simulating its flight dynamics and performance. The more accurate the model, the more precisely the simulations match the actual behavior. This chapter aims to create a Falk model that captures both **clean** and **iced** dynamics. Here, a clean model refers to a model without any ice accretion on any of its surfaces.

As written in [4], several approaches exist to obtain a mathematical model. The most used methods include flight testing, wind tunnel testing, analytical techniques, and numerical tools. Each method has its advantage and drawbacks. Briefly summarized, flight tests offer the most realistic model, but it comes with the inherent risk of causing damage to the physical UAV. In order to obtain the iced model, it will be important that ice accretion appears on the UAV. Ice accretion can be challenging to achieve in a controlled manner, especially when a desired type of ice structure is to be examined. Furthermore, it is necessary to have the physical UAV available for flight testing.

Wind tunnel tests allow for more controlled testing, with less risk to the physical UAV. The ice accretion can also take place in a more controlled manner. This is because the testing conditions, such as temperature, humidity, and droplet size, can be controlled. However, the financial and time costs associated with constructing and calibrating a wind tunnel can be prohibitive, especially when dynamic coefficients are to be obtained. Obtaining all stability derivatives with reasonable accuracy in a wind tunnel test can be challenging.

In contrast, analytical methods are the most straightforward, and much literature exists on the subject. This method often demands making certain assumptions, which can sometimes oversimplify the complex nature of real-world aerodynamics. Lastly, the numerical approach that is utilizing the power of computers. Computational tools, such as CFD software, offer a wide range of capabilities. Some CFD programs have the capability to analyze the aerodynamics of surfaces with specific ice structures.

## 3.1 Modelling approach

It is generally beneficial to derive the clean and iced models using the same approach. This ensures that any uncertainties inherent in the modeling process are consistent across both models, making comparisons more reliable. For Falk, a clear choice of modeling approach was made due to certain constraints and resources.

In lack of the physical Falk, but having an accurate 3D CAD model of the entire UAV made the numerical approach applicable. A CFD program with detailed information about the airfoil shapes, control surfaces, and weight distribution has enough information to run both static and stability analyses. The static analysis gives static coefficients, and stability analysis gives derivative coefficients.

Having decided that a numerical method will be used, the next step in the modeling is to obtain a clean model. The clean model will be the base for the iced model. By developing the iced model from the clean model, there will be more validity in comparing them. Falk's clean model is purely obtained from XFLR5 analyses. The simple CFD program XFLR5 is introduced in section 2.4, and the analysis procedure in this thesis is the same as in [4]. The procedure will be repeated in the next section to get a comprehensive understanding of the modeling by just reading this thesis.

Further expansion to the iced model necessitates more sophisticated CFD calculations. One suitable program for this task is Ansys FENSAP-ICE. This program is introduced in section 2.4, where it is said to be powerful and demands significant computational resources. The use of this program is described in more detail in section 3.3.1. However, it is essential to mention that the static longitudinal coefficients for the wing, horizontal- and vertical tailplane are obtained with different ice structures on the airfoils leading edges.

A comprehensive iced longitudinal model can be obtained by combining the results of these separate CFD analyses using the two-point method from section 2.3.2. This is the same approach as in [4]. Further model development includes analytical methods in combination with iced lift coefficients to obtain an iced lateral model. Analytical methods will also be used to model changes in dynamics and stability due to ice.

## 3.2 Clean model

It is previously stated that the clean model is purely obtained from XFLR5 analyses, like in [4]. All analyses are re-done in this thesis with corrections in wing tilts and weight distribution. Furthermore, the model is extended to a two-point model in order to be able to introduce the coefficients for the iced Falk.

### 3.2.1 XFLR5 analysis

Initially, the UAV's physical data needs to be imported into XFLR5, where it is assembled into XFL format. Due to its limitations, XFLR5 is not suitable for analyzing structures other than structures with airfoil-shaped cross-sections. Thus, the fuselage, booms, and other structures are excluded from the program. However, the main wing is designed in the program in a way that somehow matches the length and size of the fuselage to account for the additional induced drag that the fuselage would generate. Figure 3.1 shows how the XFLR5 model is assembled by a wing, and horizontal and vertical tailplane, which are all airfoils. The positions, sizes, tilts, and twists of the airfoils are precisely defined in relation to each other. The specifications of the Falk are reviewed in appendix A.

The execution of XFLR5 analyses takes a relatively short time, and the results enable the acquisition of clean coefficients for the mathematical model. These coefficients inserted in the equation set (2.1-2.6) result in the model, henceforth

referred to as the one-point model. This naming is to distinguish the model from the forthcoming two-point model.

The following steps outline the process for obtaining the one-point model.

1. **Detailed 3D CAD model retrieval**. This model should include airfoil geometries, such as shaping, chord lengths, twists, and surface areas. The inclusion of control surfaces enables the acquisition of dynamic coefficients. The physical geometric details related to the Falk are shown in appendix A.
2. **Detailed weight distribution retrieval**. This information is fundamental for defining the inertia matrix. The program generates an estimated inertia matrix by inserting the position and mass of Falk components in the XFLR5 model.
3. **Airfoil importation into XFLR5**. These airfoils must be imported into XFLR5 as DAT-files, which are easily available online [22]. Once the airfoils are imported, XFLR5 can conduct a series of analyses covering a range of Reynolds numbers and angles of attack. The maximum Reynolds number can be relatively small for small UAV airfoils operating at low speeds ($> 40\ m/s$). In this thesis, the maximum is set to 4 million.
4. **3D model reconstruction in XFLR5**. The 3D mode in XFLR5 allows easy model definition using the information from appendix A. This XFLR5 model should be as similar to the CAD model as possible.
5. **Static analysis execution**. This results in the static longitudinal coefficients $C_L(\alpha), C_D(\alpha), C_m(\alpha)$ and the static lateral coefficients $C_Y(\beta), C_l(\beta), C_n(\beta)$. All these coefficients are crucial for determining the one-point model with equations (2.1-2.6). The analyses are carried out in the range -3 to 7 degrees for AoA, $\alpha$, and -10 to 10 degrees for sideslip, $\beta$.
6. **Stability analysis execution**. Stability analysis involves running a series of analyses by iterating through minor perturbations for the aileron, elevator, and rudder. This process yields the stability and control derivatives, which are characteristic of the dynamics of the Falk.

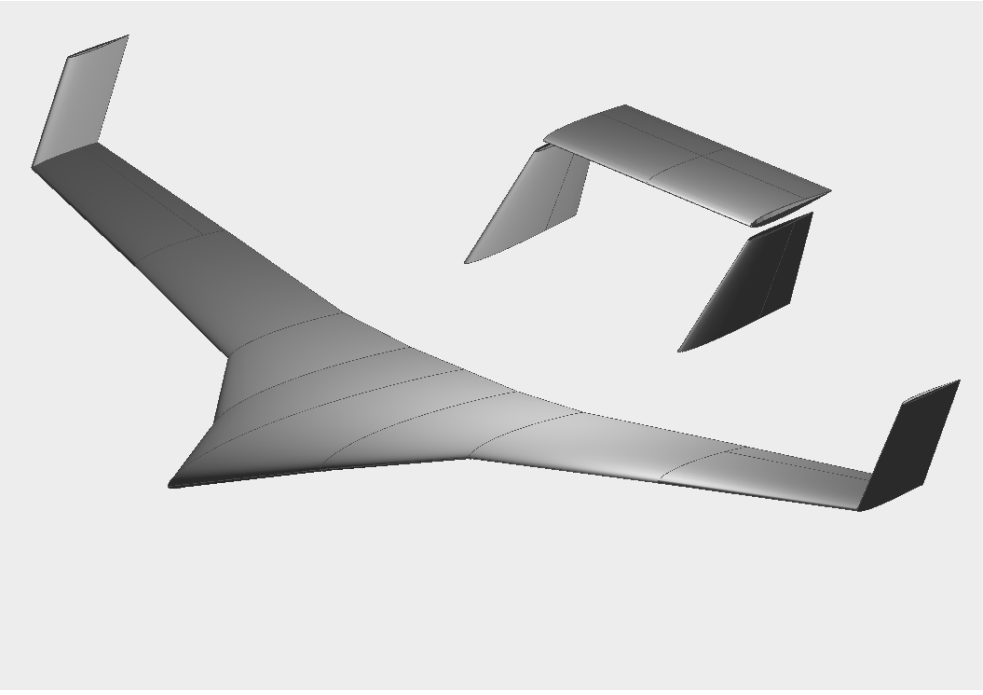

**Figure 3.1:** Falk XFLR5 3D model. Illustration from [4]

### 3.2.2 Extension to two-points model

The clean model includes coefficients for the Falk as a complete entity. Concerning a Falk affected by ice, the computation of these coefficients proves exceptionally computationally intensive when utilizing a CFD program. To make the advanced CFD analyses manageable, they are done for each airfoil separately. This means that the main wing and the stabilizers, which are shaped like RG-15 and SD8020, respectively, are analyzed independently. The results from the advanced CFD analyses provide the static *longitudinal* coefficients for each airfoil.

Now, the two-point model from section 2.3.2, which separates the main wing and horizontal tail plane, is used to form a new longitudinal model. Thus, the new model can be introduced for ice by inserting the new coefficients.

#### Twin-boom configuration

Since the two-point model is based on calculating forces or moments in the wing and HTP separately, it is worth examining that the Falk is a twin-boom aircraft with a high boom tail. Twin-boom aircraft, characterized by a short fuselage and an empennage supported by two tail booms extending from the main wing [23]. Figure 2.1 illustrates Falk's twin-boom construction. Since most UAVs do not need large cargo space, the fuselage can be smaller and shortened, and the twin-boom construction can be used. Thus, this is a common construction for UAVs. An advantage of the smaller and shorter fuselage is reduced parasite drag due to the decreased surface area. Moreover, this construction allows for the motor to be installed at the rear of the fuselage, which not only reduces nacelle drag but also offers a degree of protection for the motor and propeller.

The twin-boom design makes it possible to customize the distance between the wing and tail without it leading to a particularly increased weight and drag. This distance is the lever arm for longitudinal stability. If the distance is extended, the required HTP lifting force to achieve the same trim conditions is less. Less required HTP lifting force allows for a smaller HTP, leading to less weight and drag. This reasoning becomes essential when some assumptions about the longitudinal coefficients must be made.

#### Longitudinal aerodynamic coefficients

Comparing the longitudinal equations of the one-point model (2.1-2.3) and the two-points model (2.14-2.19), they have apparent similarities. Further examination of the two-point model draws attention to the fact that the stability derivatives $C_{L_q}$, $C_{D_q}$ and the control derivatives $C_{L_{\delta_e}}$, $C_{D_{\delta_e}}$, $C_{m_{\delta_e}}$ are absent. The inclusion of these coefficients is desirable for a dynamic model. These coefficients have to be obtained from the one-point model. This is because the wing and HTP are not separately stable, and stability analysis cannot be accomplished separately. Furthermore, these coefficients only apply to the UAV as a whole when forces and moments are calculated in CG. Hence, the terms containing these coefficients are added to the two-point model in CG. This introduces a new stage of forces and moments calculation for the two-point model

$$L = ||\overrightarrow{L}|| + \bar{q}\, S_W \left( C_{L_q} \frac{c}{2V} q + C_{L_{\delta_e}} \delta_e \right) \tag{3.1}$$

$$D = ||\overrightarrow{D}|| + \bar{q}\, S_W \left( C_{D_q} \frac{c}{2V} q + C_{D_{\delta_e}} \delta_e \right) \tag{3.2}$$

$$m = \overrightarrow{M}_{@CG_{(2)}} + \bar{q}\, S_W\, c_W \left( C_{m_{\delta_e}} \delta_e \right) \tag{3.3}$$

Calculating the norm of the lift and drag vector results in the lift and drag magnitude in the stability frame. These forces must be rotated into the body frame before all aerodynamic forces are summed. Extracting the second element in $\overrightarrow{M}_{@CG}$ gives the moment of interest, namely the pitching moment.

Equations (2.18-2.19) requires the pitch damping derivatives $C^W_{m_q@P_W}$ and $C^H_{m_q@P_H}$. The recently mentioned issue of CFD stability analysis for wing and HTP also comes into play when determining these coefficients. Given the twin-boom configuration and the relatively small surface of the HTP is the pitching moment at HTP with respect to HTP quarter chord point, $\overrightarrow{M}^H_{@P_H}$, quite minimal. Furthermore, comparing this moment with the moment generated by the HTP aerodynamic lift and drag, $\overrightarrow{P_W P_H} \times \left(\overrightarrow{L}^H + \overrightarrow{D}^H\right)$, it proves to be of negligible significance. This discrepancy arises primarily due to the significant difference in the lever arms of the two moments. The distance from the HTP lift and drag point of attack to the HTP quarter chord point, $P_H$, is negligible compared to the distance $|\overrightarrow{P_W P_H}|$. Thus, when $\overrightarrow{M}^H_{@P_H}$ is negligible, it is not necessary to determine $C^H_{m_q@P_H}$.

On the other hand, the pitching moment at the main wing with respect to the wing quarter chord point, $\overrightarrow{M}^W_{@P_W}$, does contribute to the overall pitching moment. Thus, it is desirable to calculate the moment contribution, leading to $C^W_{m_q@P_W}$ having to be evaluated. The pitch damping coefficient $C^W_{m_q@P_W}$ is estimated according to [17] as

$$C^W_{m_q@P_W} \approx C^{\text{global}}_{m_q@P_W} + C^H_L(\alpha_H)\,\frac{S_H}{S_W}\,\frac{(\overrightarrow{P_H P_W}\cdot\overrightarrow{x}_s)\,(\overrightarrow{P_H\,CG}\cdot\overrightarrow{x}_s)}{c_W} \tag{3.4}$$

where $C^{\text{global}}_{m_q@P_W}$ can be obtained from stability analyses of the composite one-point model with respect to $P_W$.

Furthermore, to complete the clean two-point model, the coefficients $C^W_L(\alpha)$, $C^W_D(\alpha)$ and $C^W_{m@P_W}(\alpha)$ are found by analyzing the wing isolated in XFLR5 following the same procedure as described at the beginning of this section. Additionally, the coefficients $C^H_L(\alpha_H)$ and $C^H_D(\alpha_H)$ are found by isolating the HTP in XFLR5 analysis. It is crucial to be aware of the tilt angles of the airfoils when simulating. The main wing of the Falk is tilted 4° upward relative to the body frame x-axis, and the HTP is tilted 1.5°. The body frame's x-axis is aligned with a level fuselage and tail boom. It is worth noting that the difference in tilt angles causes the airfoils to encounter different angles of attack.

### 3.2.3 Downwash and Sidewash gradient

Finding the downwash angle at the tail from eq. (2.20) need the usage of table lookup in [16] for determining $\kappa_v$ and $\kappa_b$. The tables request the wing taper ratio, $R^W_T$, and the wing aspect ratio, $R^W_A$. The inner part of the wing of the Falk is more tapered than the outer, which is seen in figure A.1. The figure shows that the taper ratio for the inner part is lower than the outer part for the Falk. The final taper ratio is calculated by summing the taper ratio of each part multiplied by the proportion the part takes of the wing length. Table A.1 shows the chord lengths and distances between chords. Repeating the necessary values

The final taper ratio for the Falk is calculated as

$$R^W_T = \frac{c_{\text{chord 2}}}{c_{\text{chord 1}}}\cdot\frac{\text{inner wing length}}{\text{wing length}} + \frac{c_{\text{chord 3}}}{c_{\text{chord 2}}}\cdot\frac{\text{outer wing length}}{\text{wing length}} = 0.57$$

| | length [mm] |
|---|---|
| $c_{\text{chord 1}}$ | 600 |
| $c_{\text{chord 2}}$ | 350 |
| $c_{\text{chord 3}}$ | 200 |
| inner wing | 250 |
| outer wing | 1100 |
| wing | 1350 |

The aspect ratio for the Falk is calculated straightforward with $b = 3.1\,\text{m}$ and $S^W = 1.2\,\text{m}^2$

$$R_A^W = \frac{b^2}{S^W} = 8$$

Using the found taper ratio and aspect ratio for the wing for table lookup, which gives the following result

$$\kappa_v = 0.98$$
$$\kappa_b = 0.8$$

For further investigation of the Falk downwash angle, the vector from the HTP quarter chord point to the wing quarter chord point is needed

$$\overrightarrow{P_W P_H} = \begin{bmatrix} 0.9690 \\ 0 \\ 0.2530 \end{bmatrix}$$

which gives the necessary information to calculate the tail position factor, $\kappa_p$, from equation (2.21)

$$\bar{x} = 0.6252\,, \quad \bar{y} = 0.1632\,, \quad \bar{z} = 0$$

$$\Rightarrow \kappa_p = 0.5193$$

The Falk has a wing sweep angle of $\Lambda = 10°$ , which is needed in the calculation of the wing sweep factor, $\kappa_s$ from equation (2.23)

$$\bar{r} = 0.6461\,, \quad \bar{s} = 0.2599\,, \quad \bar{t} = 0.8944\,, \quad \bar{t}_0 = 1.0283$$

$$\Rightarrow \kappa_s = 1.0634$$

The downwash angle is then estimated by

$$\epsilon_H = 0.0846\, C_L^W$$

### 3.2.4 Sidewash gradient

Calculation of the sidewash gradient by eq. (2.29) need the tail sidewash factor, $\kappa_\beta$, that are obtained from eq. (2.30). Specific for the Falk, it is

$$\kappa_\beta = 0.0162$$

Further, can the sidewash gradient from eq. (2.29) be estimated as

$$\epsilon_{s,\beta} = -0.0025 C_L^W$$

## 3.3 Iced model

Icing significantly affects the aerodynamics of the UAV, and different icing structures affect the aerodynamics differently. This makes modeling the icing effects on a UAV a unique challenge due to the complex influence of weather conditions. The iced model found in this thesis is limited to ice accretions on the airfoils leading edges. This type of icing lead to a significant reduction of lift force and increase of drag force[1]. This could result in significant performance degradation, disrupting the balance of aerodynamic forces.

The primary basis of the icing modeling approach pivots on aerodynamic lifting force reduction and increase of drag force. Firstly, it is desired to quantify the lift reduction and drag increase for every airfoil for all icing formations of interest. Subsequently, the consequences of the icing are found in terms of forces and moments. Some of the forces and moments lead to an increase in energy consumption, while some lead to variations in stability. Moreover, the moments mentioned are a product of the aerodynamic forces and geometric distances of the UAV. The modeling in this chapter aims to capture both increased energy consumption and variations in stability. In terms of stability, the variations in lift forces are the most influential parameter [24]. Thus, the variations in stability can be evaluated when the change in lift forces is known. In addition, the lifting forces can be evaluated using lifting coefficients or lift slopes.

The iced model will take shape by first reviewing the longitudinal model and then the lateral.

### 3.3.1 Iced longitudinal model

The longitudinal model includes the static coefficients $C_L$, $C_D$, and $C_m$ for both the wing and HTP. As stated in section 3.2.2 is the two-point model utilized to make advanced CFD analyses manageable. Ansys FENSAP-ICE is utilized to determine the coefficients for the iced Falk. This is the same approach as in [4]. As stated in section 2.4, the analyses done in Ansys FENSAP-ICE are powerful and advanced, which require lots of background understanding. The three coefficients describing the static longitudinal iced Falk in this thesis are found by Markus Lindner, where the analysis and results are presented in his paper [12]. Lindner is at the time of writing a Ph.D. student and is currently researching ice accretion and performance degradation of UAVs [25].

The FENSAP-ICE analyses obtain the coefficients for every airfoil separately. In the case of the Falk, the wing and tailplanes have to be analyzed separately. Looking in table A.1 reveals that the wing is shaped as an airfoil named RG-15 and the tailplanes as SD8020. Both airfoils have been analyzed in multiple icing conditions, which makes it possible to analyze the Falk longitudinal performance in different icing conditions. In all icing analyses, the ice has accumulated on the airfoil leading edge for 1290 seconds, 21,5 minutes. The static coefficients are also found for the clean case in FENSAP-ICE. Further is the ratio of change from clean to iced cases found for all icing cases

$$Q_{C_k} = \frac{C_{k,\text{iced,F}}}{C_{k,\text{clean,F}}}, \quad k \in \{L, D, m\} \tag{3.5}$$

The notation with subscript F indicates that the coefficients are obtained in FENSAP-ICE. Since the clean model is found with XFLR5, obtaining the iced longitudinal two-point model out of the corresponding XFLR5 coefficients is desirable. This is

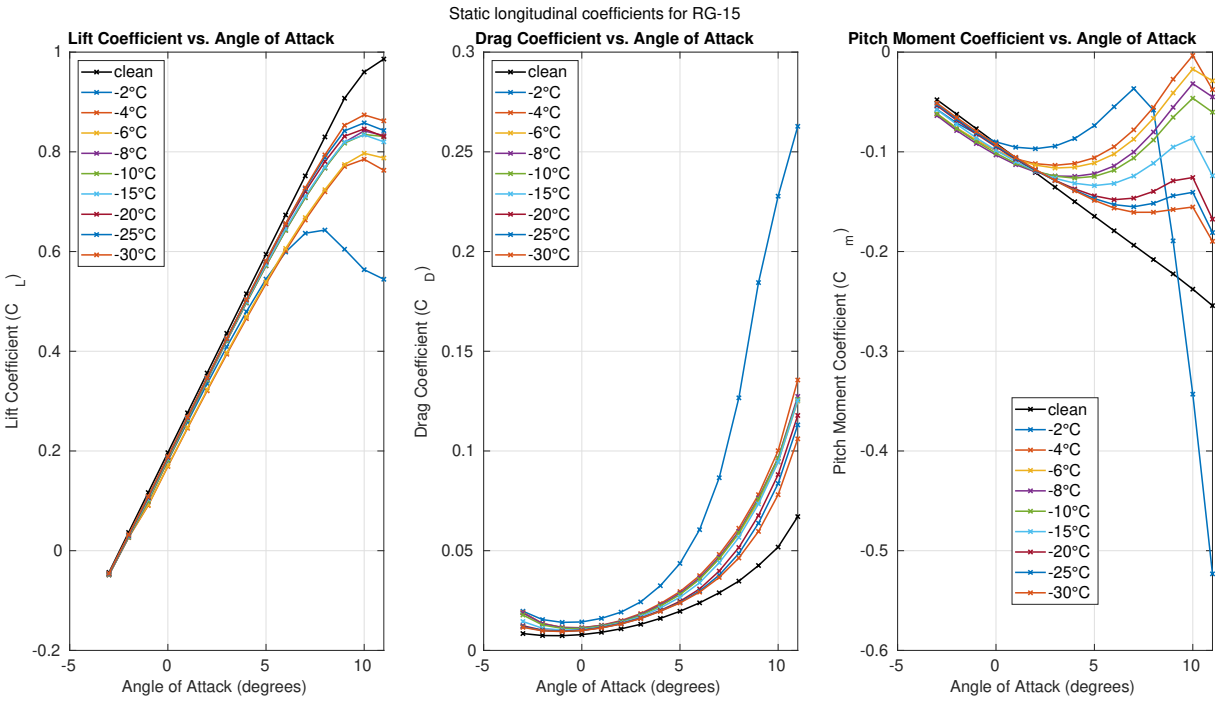


**Figure 3.2:** The static longitudinal coefficients $C_L$, $C_D$ and $C_m$ for the RG-15 airfoil in icing conditions after 21 minutes with droplet size 20 $\mu m$ and different air temperatures

done by transforming the static longitudinal XFLR5 coefficients to iced coefficients by using the ratio of change from the FENSAP-ICE analyses as

$$C_k = C_{k,\text{clean}} Q_{C_k}, \quad k \in \{L, D, m\} \tag{3.6}$$

This is done to be faithful to the coefficients from just one CFD program.

The plots in figure 3.2 show the static longitudinal coefficients for the RG-15 airfoil on the first axis and the angle of attack on the second axis. It is three plots that present $C_L$, $C_D$, and $C_m$, respectively. All three plots have a black graph representing the clean wing's coefficients. The spectral-colored graphs represent the coefficients in specific icing conditions. The icing conditions are characterized by a water droplet size (MVD) of 20$\mu m$, and different air temperatures ranging from $-2$°C to $-30$°C. These ice-affected coefficients are obtained by multiplying the clean coefficients with the ratio of change from the FENSAP-ICE analyses, as in eq. (3.6). The left plot shows the lift coefficients and the expected lift degradation is clearly shown. The degradation increases with increasing angle of attack. The ice structure formed in $-2$°C have the most degradation, followed by $-30$°C and $-6$°C. The middle plot shows that the ice also affects the drag coefficient. Increasing drag due to ice is expected, and that is what the plot shows. Also, for this coefficient, there is a growing difference from the clean case with respect to the angle of attack. Not surprisingly, the $-2$°C case has the most increase. The decrease in lift and increase in drag can be explained by the fact that the wing's intended aerodynamic structure gets troubled by the ice. How the ice has shaped on the leading edge is shown in figure 3.3. This figure illustrates the airfoil leading edge in black and the ice accretion structures in spectral colors. The phenomenon of lift decrease and drag increase is recognized and is described in more depth in the work of Hann [1].

The lift and drag coefficient for the SD8020 airfoil at different temperatures with

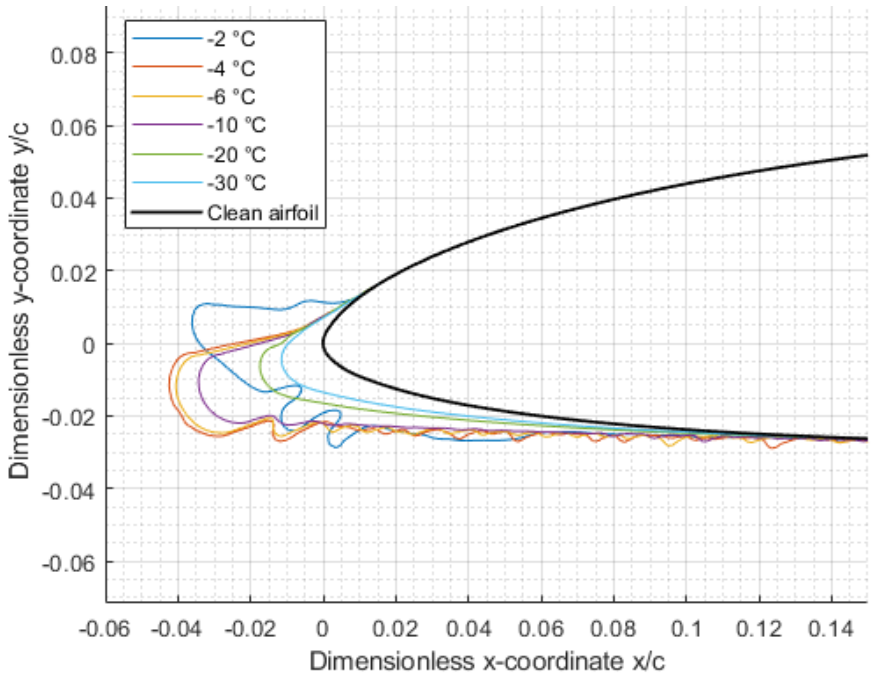


**Figure 3.3:** Ice accretion on the RG-15 airfoil leading edge after exposure to icing conditions with droplet size 20 MVD and different temperatures for 21,5 minutes. The airfoil is colored black, and the ice structures are in spectral colors.

MVD 20$\mu m$ is shown in figure 3.4. They are calculated in the same way as the RG-15 airfoil.

### Longitudinal stability derivatives

In order to evaluate how Falk's dynamics are affected by ice, it is important to calculate how the ice affects the dynamic coefficients. The longitudinal coefficients in question are $C_{L_q}$ and $C^{\text{global}}_{m_q@P_W}$. The change of mass distribution significantly affects the stability derivatives due to the ice mass. Since the added mass is located away from the center of gravity, it will increase the moment of inertia. In simple words, this will make the UAV more resistant to changes in attitude rate. Thereby the stability derivatives are affected.

The approach for modeling the stability derivatives is to first analyze the clean model with the added mass where the ice accumulates, namely on the leading edge. The ice weight is found in [12] for every type of ice accretion. The weight changes with temperature and MVD. In this thesis, the stability derivatives and inertia found for the icing scenarios iced wing, iced tail, and fully iced for the ice types of interest. To clarify, fully iced denotes iced wing and iced tail. Additionally, the iced tail includes both iced HTP and iced VTP. These coefficients are denoted with the subscript *weighted* to indicate that they are found by analysis with the added ice mass. Furthermore, these coefficients are transformed with respect to the change of lift.

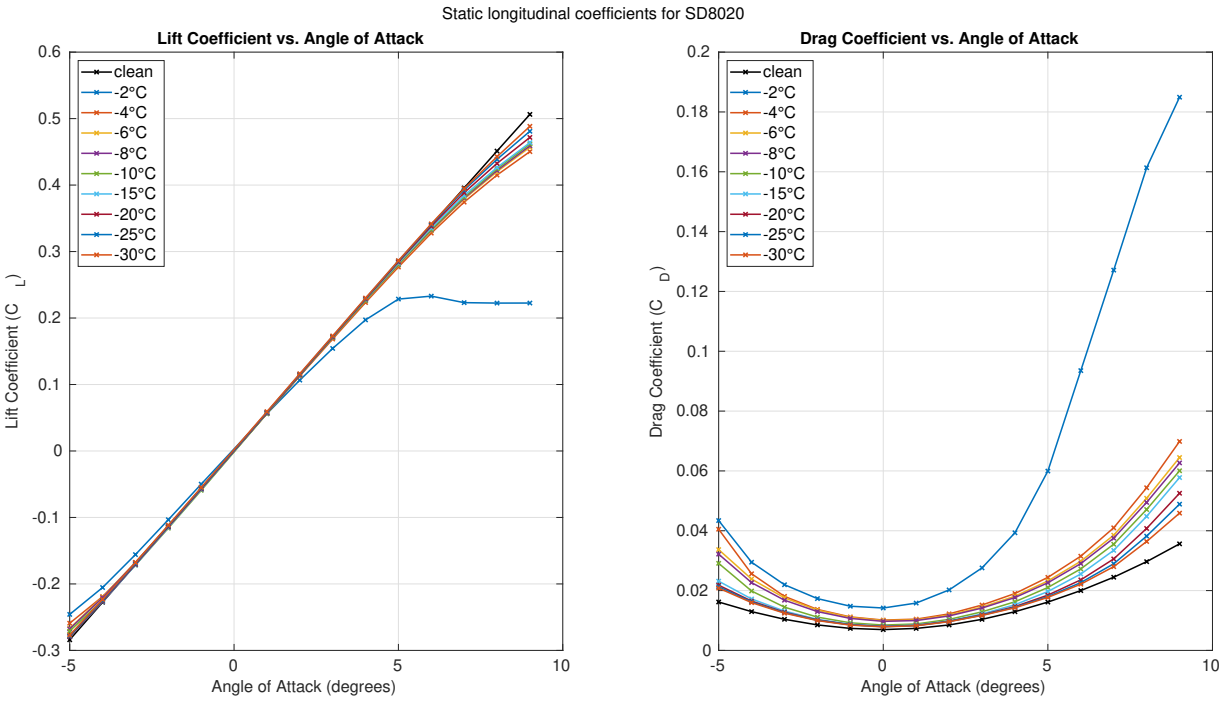


**Figure 3.4:** The static longitudinal coefficients $C_L$ and $C_D$ for the SD8020 airfoil in icing conditions after 21,5 minutes with droplet size 20 $\mu m$ and different air temperatures

Phillips [16] calculate estimates of these coefficients analytically by

$$C_{L_q,\text{calc}} = 2\,\frac{|\overrightarrow{P_G P_W}|}{c_W}\,C^W_{L,\alpha} + 2\,\frac{S_H\,|\overrightarrow{P_G P_H}|}{S_W\,c_W}\,\eta_H\,C^H_{L,\alpha} \tag{3.7}$$

$$C_{m_q,\text{calc}} = -2\,\frac{|\overrightarrow{P_G P_W}|^2}{c_W^2}\,C^W_{L,\alpha} - 2\,\frac{S_H\,|\overrightarrow{P_G P_H}|^2}{S_W\,c_W^2}\,\eta_H\,C^H_{L,\alpha} \tag{3.8}$$

Where the notation with subscript calc indicates calculation by analytical estimation. Furthermore, $\eta_H$ is the ratio of dynamic pressure on the HTP to the freestream dynamic pressure. According to Phillips [16], this ratio is very difficult to determine. However, it is typically quite close to the freestream value. Thus, in this thesis, $\eta_H = 1$ is assumed. Moreover, shows equation (3.7) and (3.8) that the change of

| Case | Main wing | HTP |
|---|---|---|
| Clean | 4.553 | 3.242 |
| −2°C | 3.822 | 2.697 |
| −4°C | 4.071 | 3.032 |
| −6°C | 4.095 | 3.065 |
| −8°C | 4.337 | 3.077 |
| −10°C | 4.335 | 3.106 |
| −15°C | 4.337 | 3.130 |
| −20°C | 4.384 | 3.153 |
| −25°C | 4.412 | 3.175 |
| −30°C | 4.422 | 3.187 |

**Table 3.1:** Lift slopes for the main wing and HTP for the clean case and in icing conditions for 21 minutes with MVD 20 $\mu m$

the dynamic coefficients is proportional to the change in the lift slopes of the main wing and HTP. Thus, the dynamics can be modeled by utilizing the lift curves. Table 3.1 shows the lift slopes for the lift curves in figure 3.2 and 3.4. The slopes are calculated by linear least-squares fit in the range −3° to 8° AoA for both wing and HTP. Furthermore, the lift slopes are used in simulation by interpolating using the same method as for coefficients, where $\zeta$ is the icing level

$$C^k_{L,\alpha}(\zeta) = \zeta\, C^k_{L,\alpha,\text{iced}} + (1-\zeta)\, C^k_{L,\alpha,\text{clean}}\,, \quad k \in \{W,H\} \tag{3.9}$$

Rewriting (3.7) and (3.8) to

$$C_{L_q,\text{calc}} = K_{L_{q,W}}\, C^W_{L,\alpha} + K_{L_{q,H}}\, C^H_{L,\alpha} \tag{3.10}$$

$$C_{m_q,\text{calc}} = K_{m_{q,W}}\, C^W_{L,\alpha} + K_{m_{q,H}}\, C^H_{L,\alpha} \tag{3.11}$$

shows how the dynamic coefficients change relative to the lift slopes multiplied with the constants $K_{L_{q,W}}$, $K_{L_{q,H}}$, $K_{m_{q,W}}$ and $K_{m_{q,H}}$. The constants indicate the importance or influence each lift curve holds when calculating the ice-affected coefficients, and are expressed as

$$K_{L_{q,W}} = 2\,\frac{|\overrightarrow{P_G P_W}|}{c_W} \qquad K_{L_{q,H}} = 2\,\frac{S_H\,|\overrightarrow{P_G P_H}|}{S_W\, c_W}\,\eta_H \tag{3.12}$$

$$K_{m_{q,W}} = -2\,\frac{|\overrightarrow{P_G P_W}|^2}{c_W^2} \qquad K_{m_{q,H}} = -2\,\frac{S_H\,|\overrightarrow{P_G P_H}|^2}{S_W\, c_W^2}\,\eta_H \tag{3.13}$$

By calculating these constants for Falk specifically, they get the values

$$K_{L_{q,W}} = 0.4548 \qquad K_{L_{q,H}} = 0.6683$$

$$K_{m_{q,W}} = -0.1034 \qquad K_{m_{q,H}} = -1.4050$$

which shows that a change in $C^H_{L,\alpha}$ has a greater influence on the dynamic coefficients than a change in $C^W_{L,\alpha}$.

It is important to have in mind that equation (3.10) and (3.11) are just estimates, and it is the change of the dynamic coefficients relative to the lift slope that is of interest in this thesis. Thus, to still be faithful to the XFLR5 coefficients, the analytical coefficient change ratio is calculated as

$$Q_{C_{L_q,\text{calc}}} = \frac{C_{L_q,\text{calc}}}{C_{L_q,\text{calc,clean}}} \tag{3.14}$$

$$Q_{C_{m_q,\text{calc}}} = \frac{C_{m_q,\text{calc}}}{C_{m_q,\text{calc,clean}}} \tag{3.15}$$

And the clean coefficients are transformed by

$$C_{L_q} = C_{L_q,\text{weighted}}\, Q_{C_{L_q,\text{calc}}} \tag{3.16}$$

$$C^{\text{global}}_{m_q@P_W} = C^{\text{global}}_{m_q@P_W,\text{weighted}}\, Q_{C_{m_q,\text{calc}}} \tag{3.17}$$

**Longitudinal control derivatives**

In addition to the stability derivative, the control derivative plays a large role when it comes to dynamics. In the longitudinal model, there are two such coefficients, named $C_{m_{\delta_e}}$ and $C_{L_{\delta_e}}$. These are preferably modeled in the same way as the stability derivatives. That means running a new set of CFD analyses, in this

case, stability analysis with small perturbations in control deflection, where the ice mass is added. Multiplying the coefficients from XFLR5 by a ratio. $C_{L_{\delta_e}}$ is zero, so it can omitted. When it comes to modeling the pitch moment control derivative, $C_{m_{\delta_e}}$, it can be seen in equation (2.13) that lift in the HTP is a significant component when calculating the pitch moment. This is reflected in Phillips' [16] estimate of the pitch moment control derivative for small angles of attack

$$C_{m_{\delta_e},\text{calc}} = \frac{S_H\, c_H}{S_W\, c_W}\eta_H C^H_{m,\delta_e} - \frac{S_H\, |\overrightarrow{P_G P_H}|}{S_W\, c_W}\eta_H C^H_{L,\alpha}\epsilon_e \tag{3.18}$$

where $C^H_{m,\delta_e}$ is the change in pitching moment coefficient for the HTP about its aerodynamic center with respect to elevator deflection. It has already been argued that the moment at HTP with respect to the HTP quarter chord point can be considered negligible previously in this section.

The control surface deflections change the camber line slope near the trailing edge of a lifting surface and are applicable for changing the lifting forces [24]. A change in elevator deflection results in a change in HTP lift, leading to a change in pitch moment. This results in the expression

$$C_{m_{\delta_e},\text{calc}} = -\frac{S_H\, |\overrightarrow{P_G P_H}|}{S_W\, c_W}\eta_H C^H_{L,\alpha}\epsilon_e \tag{3.19}$$

furthermore, the ratio is calculated by

$$Q_{C_{m_{\delta_e},\text{calc}}} = \frac{C^H_{L,\alpha}}{C^H_{L,\alpha,\text{clean}}} \tag{3.20}$$

when considering the elevator effectiveness, $\epsilon_e$, constant for both clean and iced case. The modeling of the control derivative results in

$$C_{m_{\delta_e}} = C_{m_{\delta e},\text{weighted}}\, Q_{C_{m_{\delta e},\text{calc}}} \tag{3.21}$$

### 3.3.2 Iced lateral model

The lateral model is made slightly differently than the longitudinal one because of its higher complexity. The similarity is that the clean model is also used here as a starting point for the iced model. Nevertheless, the method with ratios between clean and iced models has been replaced. Here, the factors leading to stability are divided into contributions, each evaluated separately. If a stability contribution is reduced due to icing, the reduction is subtracted from the clean model. Also, for the lateral model, lifting forces are seen as the most influential parameter for stability, and it is thus the reduction of these forces that is the premise for developing the model.

Firstly, the vertical tail plane (VTP) contribution to yaw stability is considered. The purpose of the VTP is to provide directional stability for an aircraft. When an aircraft yaw in either direction caused by a disturbance or some other force, it will experience a sideslip. This sideslip angle will cause the VTP to encounter an angle of attack. The VTP then generates a stabilizing force on the UAV that wants to minimize the sideslip angle and hence provide an increase in directional stability. Figure 3.5 visually illustrates the stabilizing VTP force. The contribution of VTP to yaw stability derivative, also referred to as yaw stiffness, is modeled after Phillips [16] as

$$\Delta C^V_{n,\beta} = \eta_V \frac{S_V\, |\overrightarrow{P_G P_V}|}{S_W\, b_W} C^V_{L,\alpha}(1-\epsilon_{s,\beta}) \tag{3.22}$$

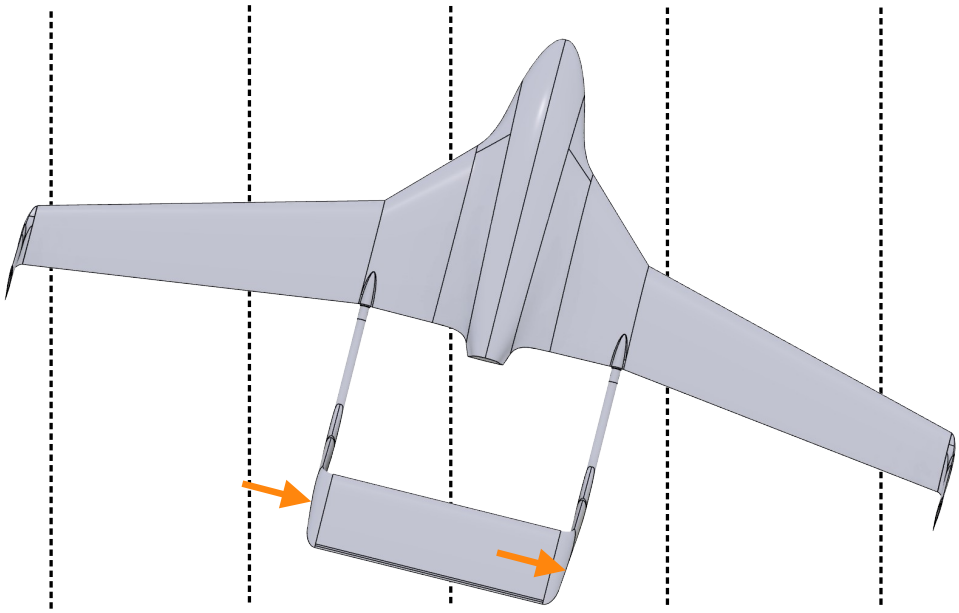

**Figure 3.5:** Illustration that shows how the VTP generates a restoring yaw moment when the UAV sideslips. The dashed lines represent the relative airflow.

Where $\Delta$ denotes a contribution, and $\eta_V$ is the ratio of dynamic pressure on the VTP to the freestream dynamic pressure. In the same way as for $\eta_H$, this ratio is very difficult to determine. However, it is typically quite close to the freestream value. Thus, in this thesis is $\eta_V = 1$ assumed. Furthermore, the sidewash gradient, $\epsilon_{s,\beta}$, is a variable in this expression affected by ice on the main wing. The change of this gradient concerning ice has already been considered in the equation (2.29). This means that with regard to ice on the VTP, there is a change in $C^V_{L,\alpha}$ which leads to a change in yaw stability. Thus, calculating the reduction of VTP contribution to the yaw stability derivative is done by calculating

$$\tilde{\Delta}C^V_{n,\beta} = \eta_V \frac{S_V \, |\overrightarrow{P_G P_V}|}{S_W \, b_W} (C^V_{L,\alpha,\text{clean}} - C^V_{L,\alpha})(1 - \epsilon_{s,\beta}) \tag{3.23}$$

where $\tilde{\Delta}$ denotes contribution reduction. Specific for Falk is the reduction

$$\tilde{\Delta}C^V_{n,\beta} = 0.025(C^V_{L,\alpha,\text{clean}} - C^V_{L,\alpha})(1 - \epsilon_{s,\beta}) \tag{3.24}$$

Furthermore, is the yaw stability reduction calculated with regard to the reduction of the yaw moment coefficient

$$C_n(\beta) = C_{n,\text{clean}}(\beta) - \tilde{\Delta}C^V_{n,\beta}\,\beta \tag{3.25}$$

The dihedral of a UAV refers to the upward angle of the UAV's main wings relative to the horizontal line perpendicular to the UAV's longitudinal axis. This dihedral angle plays a crucial role in the UAV's roll stability. When a UAV rolls to either side caused by a disturbance or some other force, it will again experience a sideslip. In this case, the sideslip will cause the lowered wing to encounter a greater angle of attack than the higher wing. Consequently, the lowered wing will generate a greater lift force, which tends to level the aircraft to no roll angle if the UAV is stable. Figure 3.6 shows this effect visually. The contribution of dihedral to roll stability is modeled after Phillips [16] as

$$(\Delta C^W_{l,\beta})_\Gamma = -\frac{2\sin\Gamma}{3\pi\cos^4\Gamma}\kappa_\Gamma\kappa_l C^W_{L,\alpha} \tag{3.26}$$

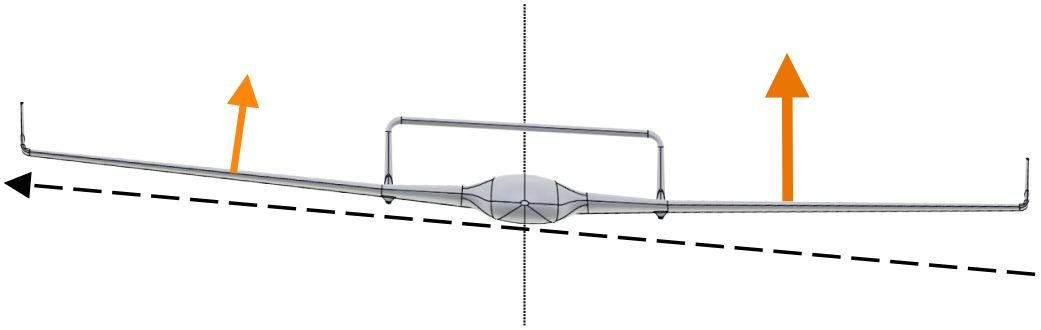

**Figure 3.6:** Illustration that shows how the dihedral makes the lowered wing generate more lift when the UAV sideslips. The dashed arrow represents the relative airflow. The thin dotted line is a vertical mark.

where $\Gamma$ is the dihedral angle. The dihedral angle may change due to flexibility in the wings, but it is assumed constant in this thesis. Additionally, all $\kappa$-terms are constant, which means that the dihedral contribution to rolling stability depends on the lift slope of the main wing. As done previously, the reduction is calculated by

$$(\tilde{\Delta}C^W_{l,\beta})_\Gamma = -\frac{2\sin\Gamma}{3\pi\cos^4\Gamma}\kappa_\Gamma\kappa_l(C^W_{L,\alpha,\text{clean}} - C^W_{L,\alpha}) \tag{3.27}$$

and calculating the constants with respect to Falk's physical measurements, the reduction becomes

$$(\tilde{\Delta}C^W_{l,\beta})_\Gamma = -0.0131(C^W_{L,\alpha,\text{clean}} - C^W_{L,\alpha}) \tag{3.28}$$

The roll stability reduction due to ice is calculated with regard to the reduction of the roll moment coefficient

$$C_l(\beta) = C_{l,\text{clean}}(\beta) - (\tilde{\Delta}C^W_{l,\beta})_\Gamma\,\beta \tag{3.29}$$

### Lateral stability derivatives

The lateral stability derivatives are modeled with the same approach as the longitudinal. They are affected by the added mass and changed inertia of the UAV, and are obtained from the same analyses as for the longitudinal ones. They are obtained from cases where ice has accumulated on the wing, tail, and wing and tail.

### Lateral control derivatives

Of the same reasoning as for the longitudinal model, control derivatives for the lateral model have to be modeled with regard to icing. From the clean lateral UAV model equations (2.4-2.6) it is used six control derivatives, two of which are modeled with regard to icing in this thesis. It is $C_{l_{\delta_a}}$ and $C_{n_{\delta_r}}$ that are modeled, and it is done in the same way as for the lateral control derivatives. The analytical estimates of the yaw moment control derivatives are given by

$$C_{n_{\delta_r},\text{calc}} = \frac{S_V\, c_V}{S_W\, b_W}\eta_V C^V_{m,\delta r} - \frac{S_V\,|\overrightarrow{P_G P_V}|}{S_W\, b_W}\eta_V C^V_{L,\alpha}\epsilon_r \tag{3.30}$$

where $C^V_{m,\delta_r}$ is the change in yawing moment coefficient for the VTP about its aerodynamic center with respect to rudder deflection. Using the argument that

the lever arm from the tail to the CG makes the moment generated by the lift forces much greater than the moment in the VTP aerodynamic center, the term $C^V_{m,\delta r}$ can be assumed negligible. This results in the expression

$$C_{n_{\delta_r},\text{calc}} = -\frac{S_V\,|\overrightarrow{P_G P_V}|}{S_W\,b_W}\eta_V\,C^V_{L,\alpha}\epsilon_r \tag{3.31}$$

furthermore, the ratio is calculated by

$$Q_{C_{n_{\delta_r},\text{calc}}} = \frac{C^V_{L,\alpha}}{C^V_{L,\alpha,\text{clean}}} \tag{3.32}$$

when considering the rudder effectiveness, $\epsilon_r$, constant for both clean and iced case. The modeling of the control derivative results in

$$C_{n_{\delta_r}} = C_{n_{\delta r},\text{weighted}}\,Q_{C_{n_{\delta r},\text{calc}}} \tag{3.33}$$

The estimate of the roll moment control derivative is based on a simple theory called strip theory. The process entails multiplying the local section lift increment by the local rolling moment arm and integrating over the wing sections containing the ailerons [16]. The expression is given by

$$C_{l_{\delta_a},\text{calc}} = -\frac{2\tilde{C}^W_{L,\alpha}}{S_W\,b_W}\int_{y_i}^{y_o} y_b\tilde{\epsilon}_a c_W\,dy_b \tag{3.34}$$

where $\tilde{C}^W_{L,\alpha}$ is the lift slope section coefficient, and $\tilde{\epsilon}_a$ is the section effectiveness. The wing section containing the ailerons is the same for the clean and iced case. Assuming the section effectiveness to be constant and equal for clean and iced cases, and assuming the lift slope section coefficient to be constant and equal to the lift slope for the entire wing, the reduction ratio can be calculated by

$$Q_{C_{l_{\delta_a},\text{calc}}} = \frac{C^W_{L,\alpha}}{C^W_{L,\alpha,\text{clean}}} \tag{3.35}$$

Like the other control derivatives is then the yaw moment control derivative calculated by

$$C_{l_{\delta_a}} = C_{l_{\delta a},\text{weighted}}\,Q_{C_{l_{\delta a},\text{calc}}} \tag{3.36}$$

## 3.4 Propeller model

The Falk uses a propeller named Mejzlik 21x10 EL, which has a length of 0.53m and a pitch of 0.254m. In comparison to the propeller used by Müller in the modeling of the Mejzlik 21x13 2B E [5] described in section 2.3.5, the pitch is slightly different. Even though the propellers have differences, the model from [5] is used in the Falk model. The justification of this choice can be supported by the following arguments

1. **Focus on higher-level dynamics**. The primary focus of this thesis is on a higher-level aspect of Falk's performance. Even if the propeller may have to rotate a few revolutions per minute faster to get the right thrust, it will not detract from the high-level performance. It is more important to see the effect of ice than to see the exact forces acting on the Falk.

2. **Limited availability to accurate model**. Using a propeller model that resembles an actual propeller allows for more meaningful analysis and simulations. This approach is preferred over tweaking the parameters to match the pitch difference, as doing so may compromise the study's overall validity.
3. **Similarity in propeller geometry**. Despite the pitch difference, the overall geometry is nearly identical. The propeller diameter is identical, and the surface area is nearly identical.
4. **Propeller pitch influence**. The propeller pitch affects the performance characteristic of a propeller, such as thrust and efficiency. However, for small variations in pitch, the variations can be negligible when considering the broader context of the Falk flight dynamics and performance. The propeller should still provide good results for simulation and analysis purposes.

The parameters used in [5] are also used in this thesis, and are shown in table 3.2 and 3.3.

**(a)** Thrust coefficient estimation parameters

| Parameter | Value |
|---|---|
| $C_{T,0}$ | 0.109 |
| $C_{T,1}$ | -0.0230 |
| $C_{T,2}$ | -0.131 |

**(b)** Power coefficient estimation parameters

| Parameter | Value |
|---|---|
| $C_{P,0}$ | 0.0348 |
| $C_{P,1}$ | 0.0782 |
| $C_{P,2}$ | -0.121 |

**Table 3.2:** Clean propeller parameters for Mejzlik 21x13 2B E

**(a)** Ice thrust performance degradation parameters

| Parameter | Value |
|---|---|
| $\Delta C_{T,0}$ | 0.0233 |
| $\Delta C_{T,1}$ | 0.0254 |
| $\Delta C_{T,2}$ | 0.0233 |

**(b)** Ice power performance degradation parameters

| Parameter | Value |
|---|---|
| $\Delta C_{P,0}$ | -0.00890 |
| $\Delta C_{P,1}$ | -0.0166 |
| $\Delta C_{P,2}$ | $-5.79 \cdot 10^{-4}$ |

**Table 3.3:** Iced propeller performance degradation parameters for Mejzlik 21x13 2B E

# Chapter 4

# Simulated Flight Performance Results

## 4.1 Simulation assessment

This section provides the simulation results of the flight performance tests in varied icing conditions. The simulation results include a pitch step response, a roll step response, and a steady coordinated turn test, simulated in identical conditions. These tests are designed to evaluate the dynamic stability, response of the UAV and actuator deflections in different icing scenarios.

The pitch step test aims to examine the UAV's longitudinal stability and response characteristics. By assessing the pitch response and other corresponding aerodynamic data, it can later be discussed how different icing affects the pitch stability margins and control inputs. These aspects are crucial for understanding how icing influences the UAV's ability to maintain stable flight and respond to control inputs. Both aspects are critical for ensuring flight safety. On the other hand, the roll step test aims to assess the UAV's lateral stability and response in varying conditions. The investigation of the results will provide an understanding of how icing impacts roll stability and the ability to maintain controlled turns.

### 4.1.1 Longitudinal assessment

For the longitudinal flight performance test, a pitch step response is chosen. The tests are done by simulating the model in a straight horizontal line before the pitch step is commanded after 50 seconds. The step has a magnitude of 20°, and after 10 seconds, there is a new step down 20°. The tests are done for four different icing scenarios: clean, iced wing, iced tail, and fully iced (iced wing and tail). Figure 4.1 shows the plot of the pitch response for the model with an ice type generated in $-6$°C and water droplet size of $20\mu m$. It is important to emphasize that the icing level is set to 1.

Together with the pitch step response are the AoA, elevator deflection, and motor rotational speed plotted in the same figure. The aerodynamic variable AoA is essential since it is directly related to the aerodynamic forces generated by the wing and HTP. The elevator deflection is essential since the primary function of the elevator is to control the UAV's pitch, which is achieved by increasing or decreasing the elevator deflection angle. At last, the motor rotational speed is plotted to visualize the motor thrust when the UAV changes altitude due to the pitch angle with ice accumulation.

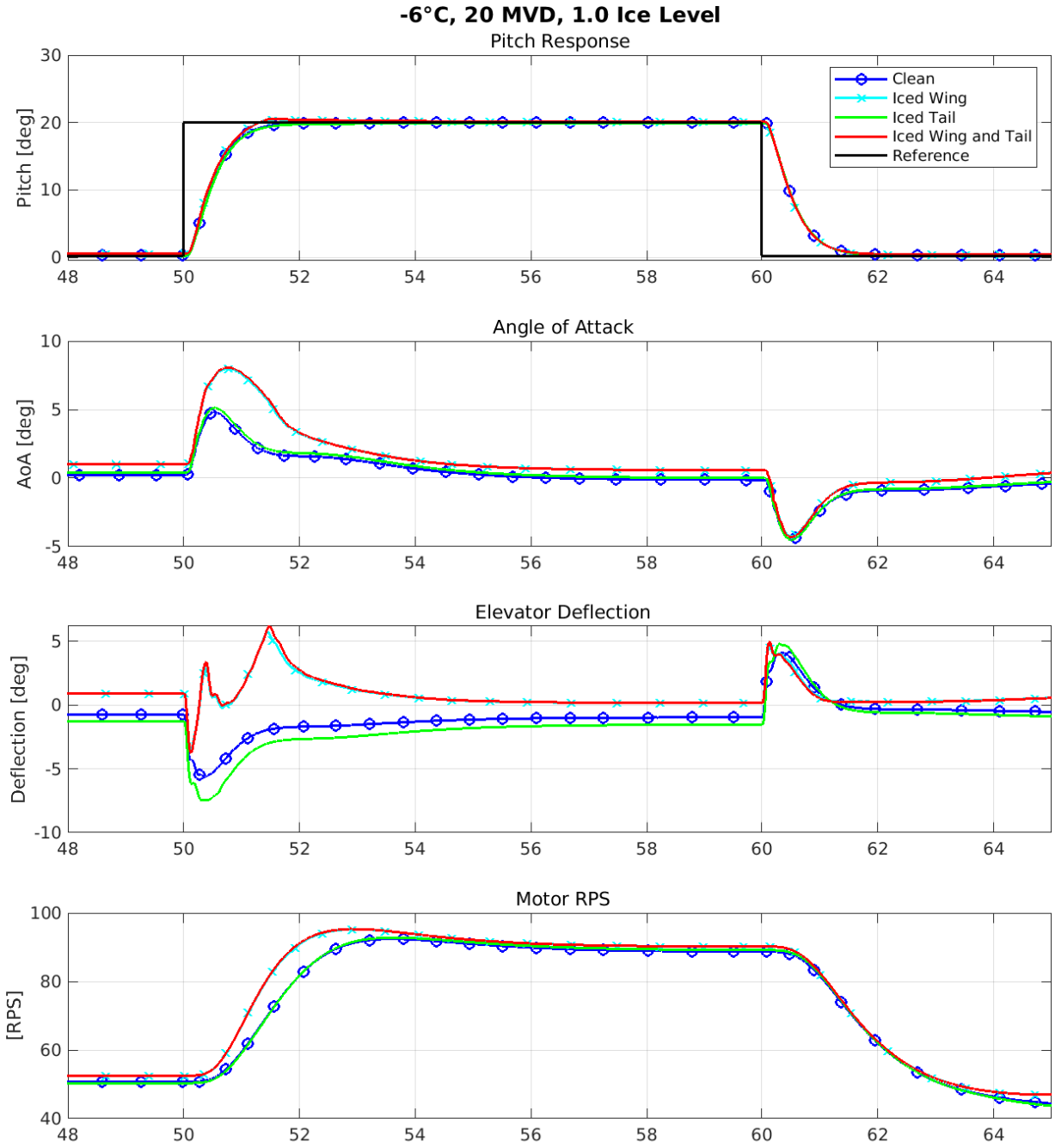


**Figure 4.1:** Comparison of flight dynamics parameters during a pitch step response in four different icing scenarios at −6°C with a water droplet size of 20$\mu m$ and icing level of 1.0

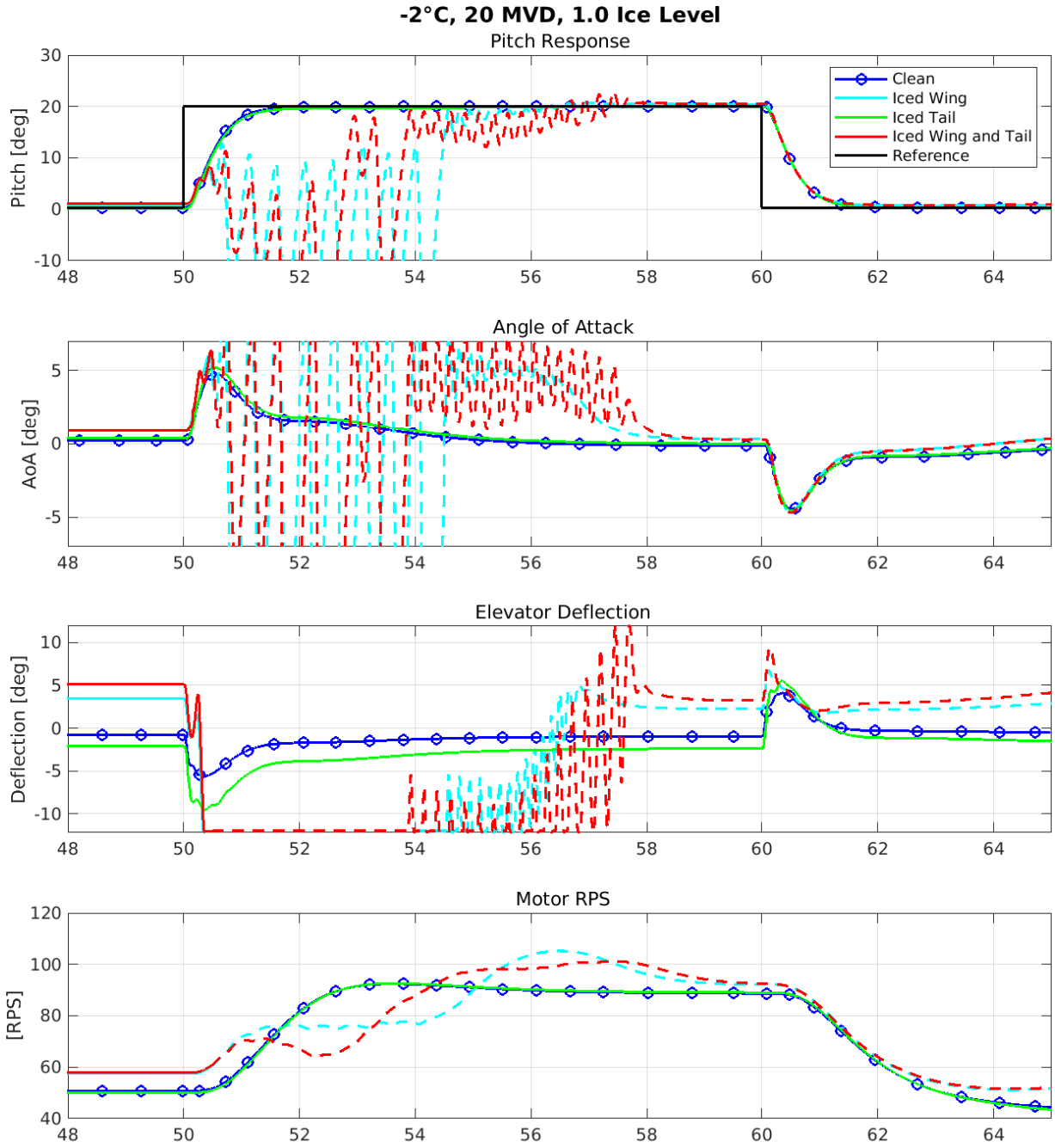


**Figure 4.2:** Comparison of flight dynamics parameters during a pitch step response in four different icing scenarios at −2°C with a water droplet size of 20$\mu m$ and icing level of 1.0

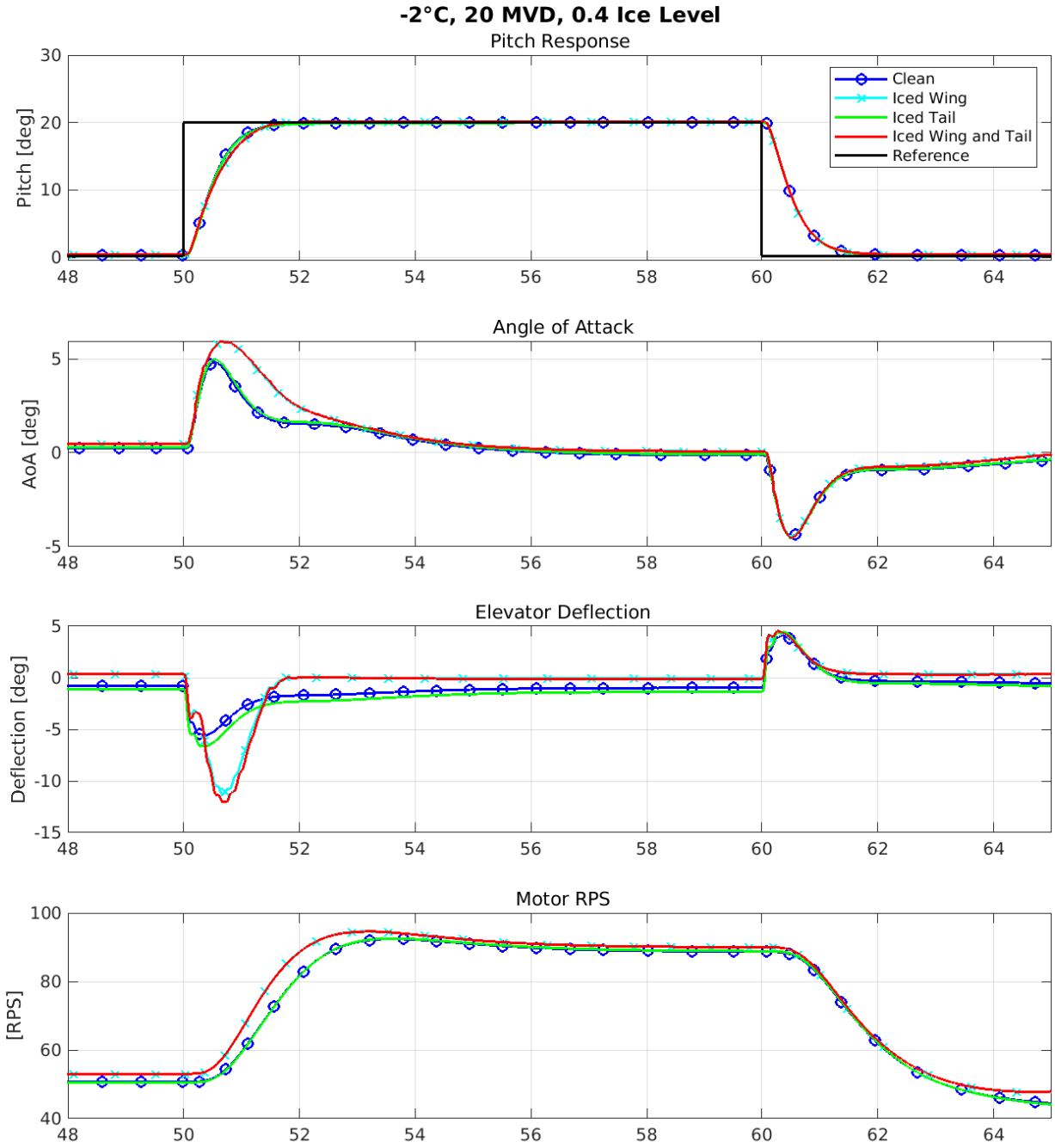


**Figure 4.3:** Comparison of flight dynamics parameters during a pitch step response in four different icing scenarios at −2°C with a water droplet size of 20$\mu m$ and icing level of 0.4

Figure 4.2 and 4.3 show the response for identical test scenarios as described above, just with a different type of ice. In these figures is the iced model generated at $-2$°C with a water droplet size of $20\mu m$. It is important to note that the difference between the test in these figures is the icing level. The test results in figure 4.2 are done with an icing level of 1, while the results in figure 4.3 are done with an icing level of 0.4. In figure 4.2, the cases for the iced wing and iced wing and tail are shown as dashed graphs after 51 seconds. The dashed graphs start when the angle of attack is far from the span the CFD analyses have been made.

Figure 4.4 has been assembled to highlight the differences in the pitch responses more effectively. This figure contains the response from figure 4.1 and 4.3, explicitly emphasizing the step response for a closer examination.

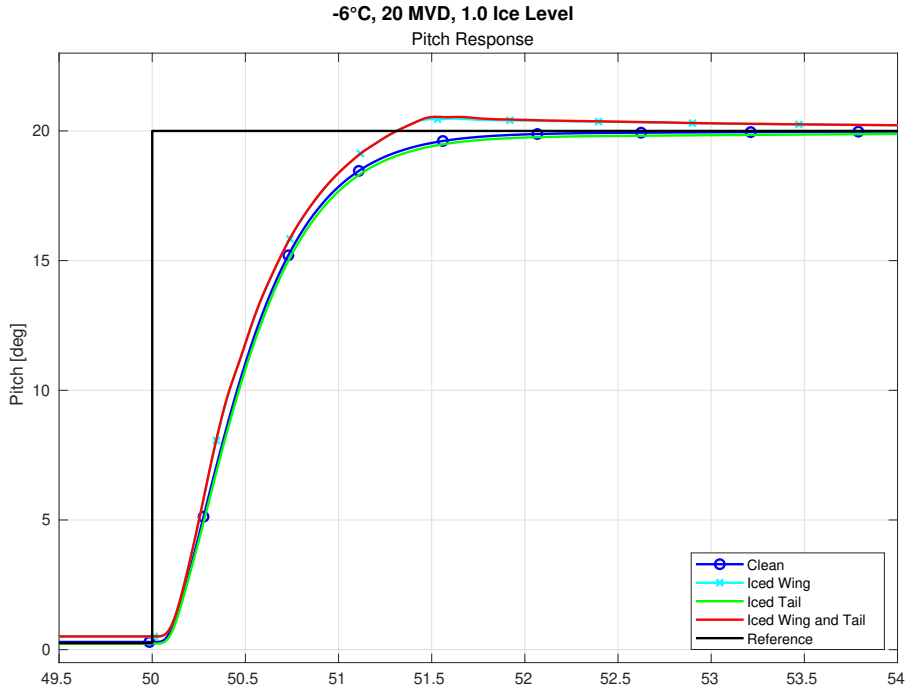


**(a)** Focused comparison of a pitch step response in four different icing scenarios at −6°C with a water droplet size of 20µ$m$ and icing level of 1.0

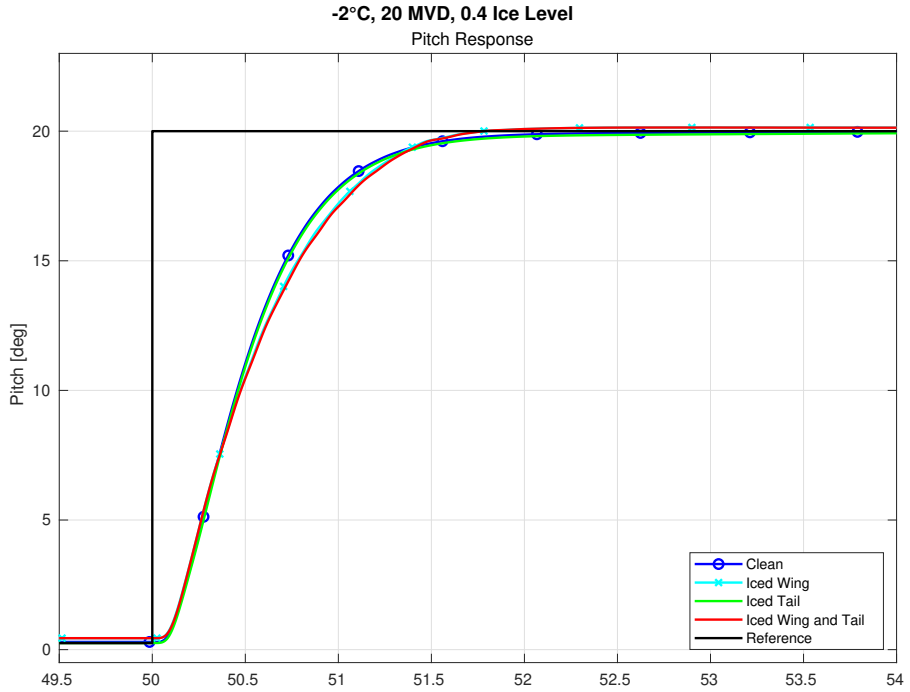


**(b)** Focused comparison of a pitch step response in four different icing scenarios at −2°C with a water droplet size of 20µ$m$ and icing level of 0.4

**Figure 4.4:** Focused pitch step responses

### 4.1.2 Lateral assessment

For the lateral flight performance test, a roll step response is chosen. The tests are done like the longitudinal tests by first simulating the model in a straight horizontal line before the roll step is commanded after 50 seconds. The step is set to be 20° and lasts for 10 seconds. The tests are done for four different icing cases: clean case, iced wing, iced tail, and at last iced wing and tail. Figure 4.5 shows the plot of the roll response for an ice type generated in −6°C and water droplet size of 20$\mu m$. It is crucial to underline that the icing level is specified as 1.

Furthermore, the sideslip angle and all actuators are shown in the same figure. The sideslip angle, a vital lateral aerodynamic parameter, holds significance due to its direct correlation with the aerodynamic forces generated in the lateral plane. When it comes to the actuators, all are shown since the simple roll step is not done alone. It is done in conjunction with an altitude controller that tries to maintain an equal altitude throughout the maneuver. This maneuver needs all actuators to be carried out, and discussing their deflection angle will be interesting later.

Analogously to the longitudinal tests is the roll step test done with the iced model in −2°C and with a water droplet size of 20$\mu m$. In contrast to the other tests, these tests are done with icing levels of 1 and 0.6. The test results are shown in figure 4.6 and 4.7, respectively. The iced tail and fully iced results in figure 4.6 are shown as dashed graphs after 51 seconds because the sideslip angle is outside the CFD analysis span.

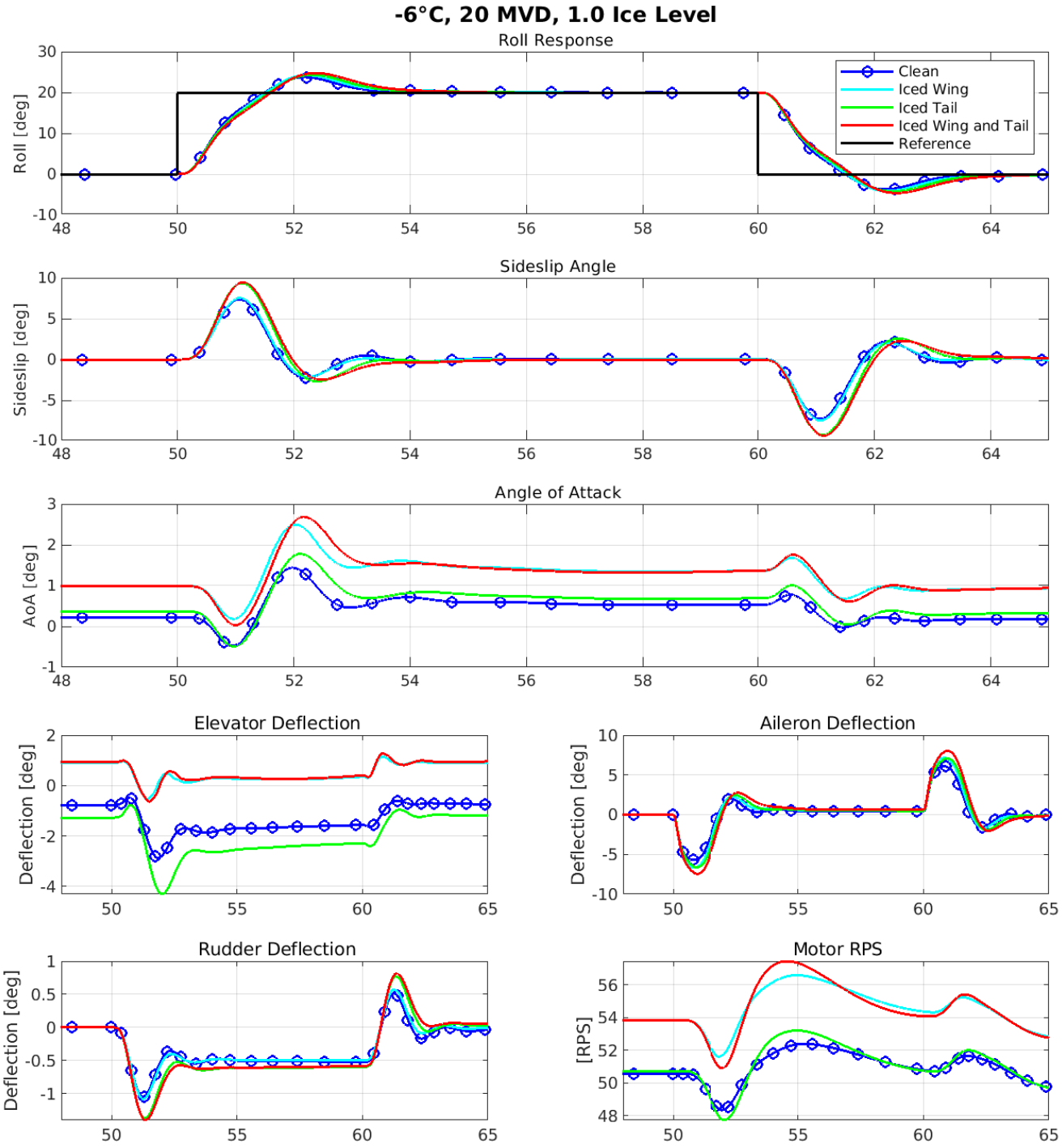


**Figure 4.5:** Comparison of flight dynamics parameters during a roll step response in four different icing scenarios at −6°C with a water droplet size of 20$\mu m$ and icing level of 1.0

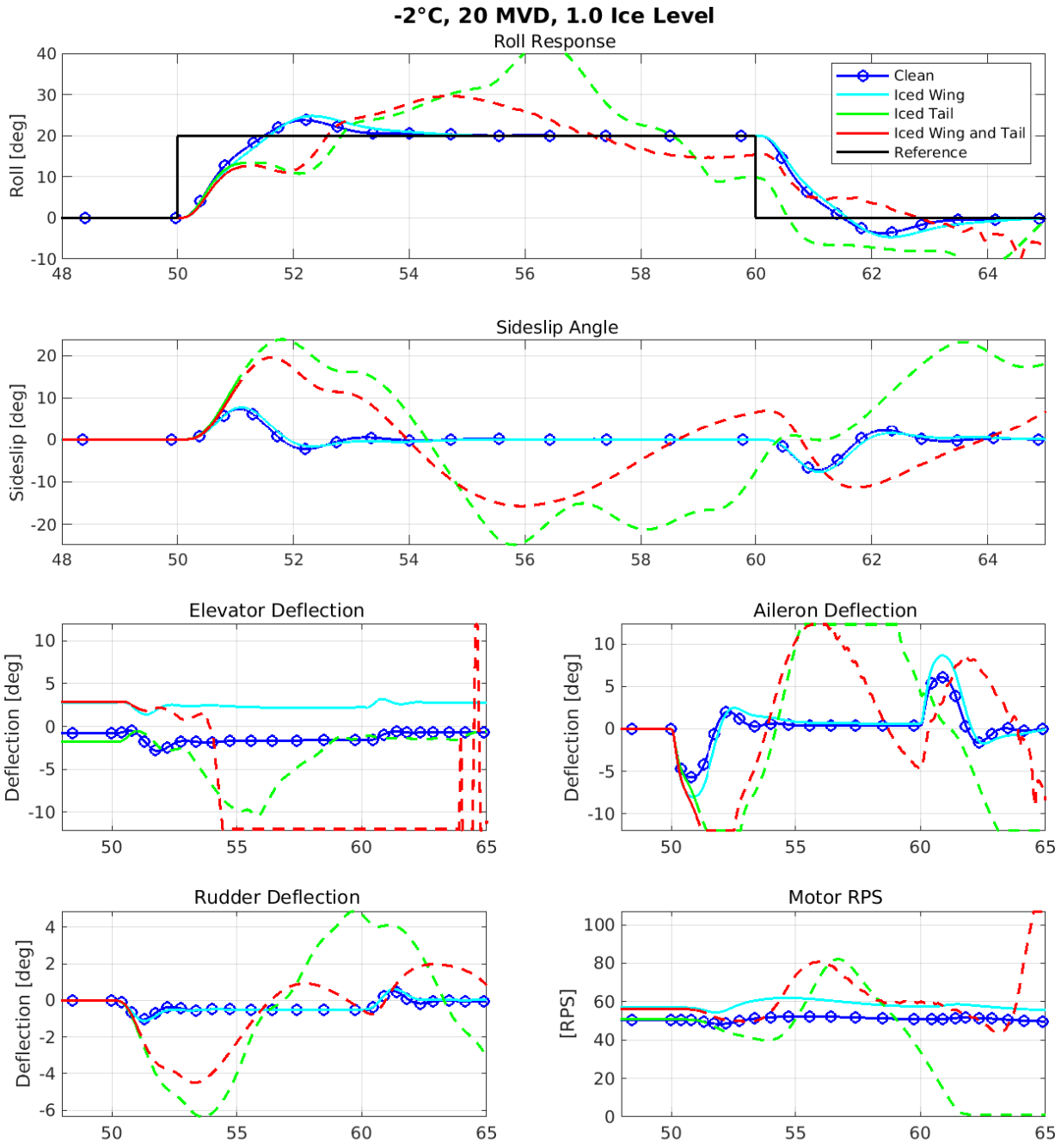


**Figure 4.6:** Comparison of flight dynamics parameters during a roll step response in four different icing scenarios at −2°C with a water droplet size of 20$\mu m$ and icing level of 1.0

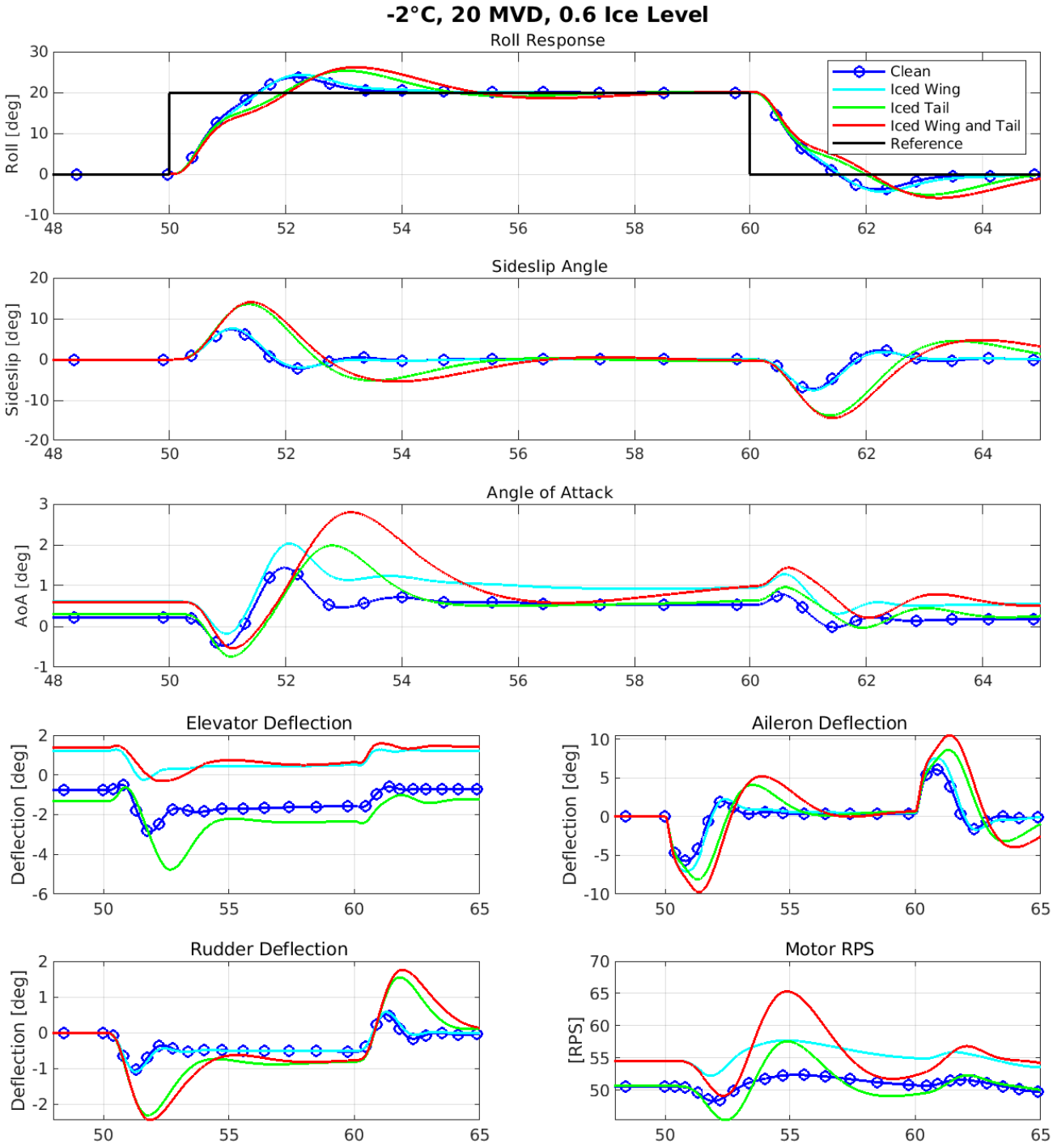


**Figure 4.7:** Comparison of flight dynamics parameters during a roll step response in four different icing scenarios at −2°C with a water droplet size of 20$\mu m$ and icing level of 0.6

### 4.1.3 Steady coordinated turn

All control surfaces must make an effort to carry out a steady coordinated turn. A steady coordinated turn can be explained as a turn where the altitude is kept constant and the sideslip angle is zero. In simple terms, the aileron initiates the bank angle, the altitude is kept constant with the elevator, and the sideslip is kept zero by the rudder. How the icing affects the control surface deflections in such a turn is interesting for knowing the iced UAV's limitations. Running a set of simulations where the model performs a steady coordinated turn with different bank angles will produce the results of interest. Figure 4.8 shows the bank angle on the first axis and the control surface deflections on the second axis. The tests are done in a span from $-50°$ to $50°$ bank angle with an interval of $5°$. A ramp reference signal gradually obtains the desired roll angle. The solid graph indicates the clean model and the dashed graph indicates iced. The iced model is used for two different icing conditions, where the $-6°$C and MVD 20 case is shown in figure 4.8b, and the $-2°$C and MVD 20 case in figure 4.8b

The position trajectory of the UAV while performing the steady coordinated turn for a selection of bank angles is shown in figure 4.9. It is shown that the UAV flies in a straight horizontal line before the turn is initiated. Each bank angle is assigned a color, and it can be seen that each angle leads to a different turn radius. To get a clear overview of the relationship between bank angle and turning radius, table 4.1 has been created. The table presents the equivalent turning radius for each bank angle during a steady coordinated turn executed by the clean UAV.

| Roll angle (°) | Turn radius (m) |
|---|---|
| 5 | 463 |
| 10 | 230 |
| 15 | 151 |
| 20 | 111 |
| 25 | 87 |
| 30 | 70 |
| 35 | 58 |
| 40 | 48 |
| 45 | 40 |
| 50 | 34 |

**Table 4.1:** Turn radius in meters for different bank angles in steady coordinated turn

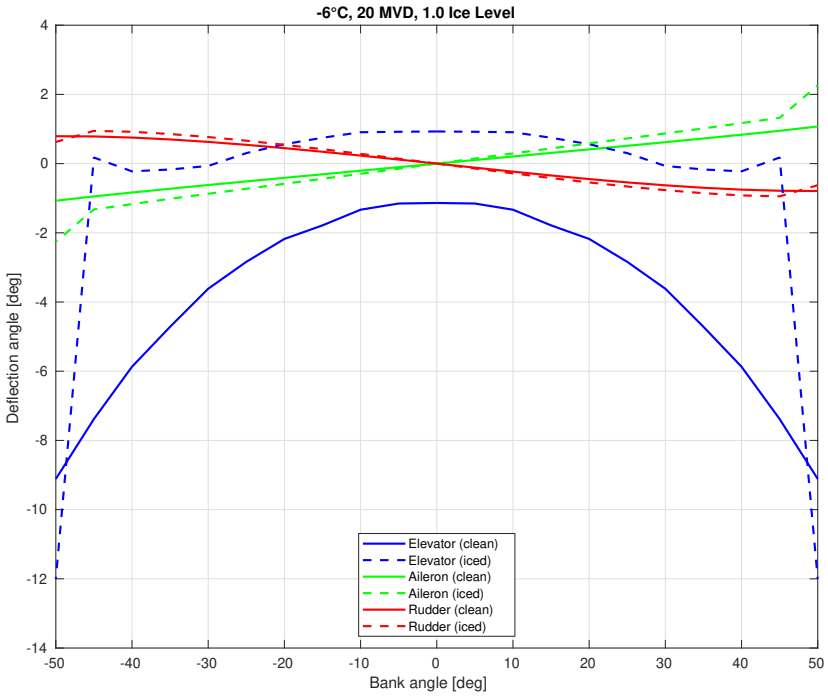


**(a)** Comparison of control surface deflections in steady coordinated turn in clean and icing conditions at −6°C with MVD 20µ$m$ and icing level of 1.0

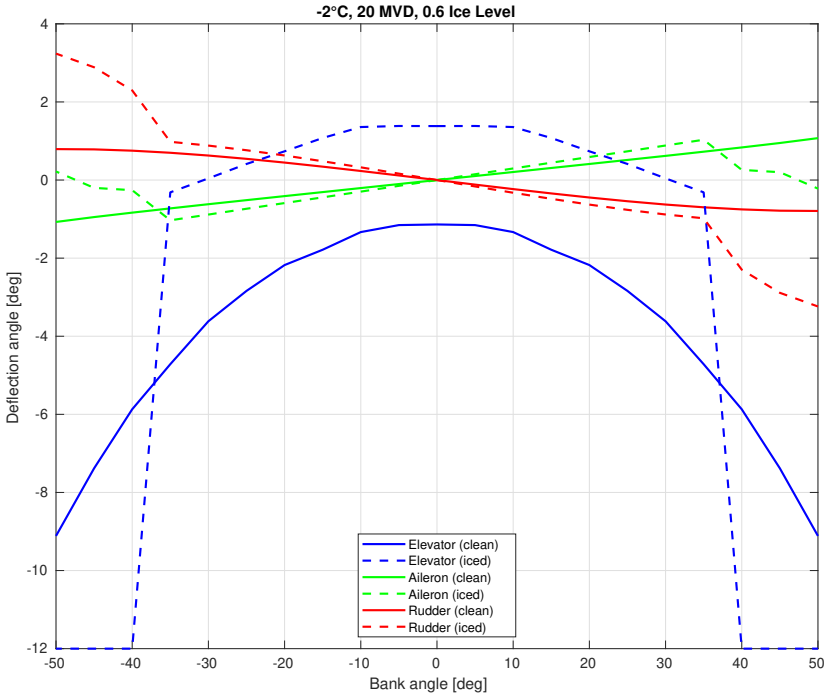


**(b)** Comparison of control surface deflections in steady coordinated turn in clean and icing conditions at −2°C with MVD 20µ$m$ and icing level of 0.6

**Figure 4.8:** Comparison of control surface deflections in steady coordinated turn of clean and two different iced scenarios

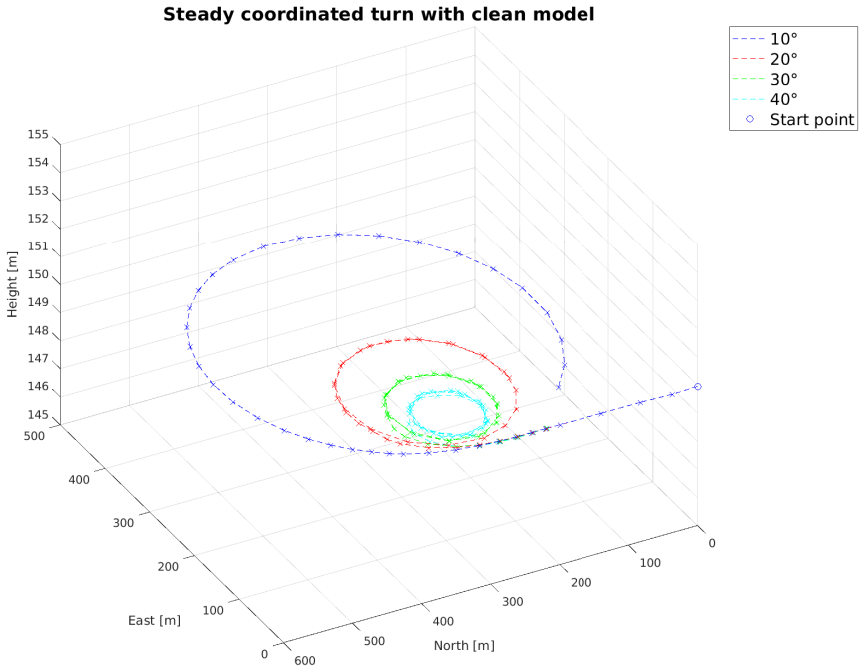


**Figure 4.9:** Steady coordinated turn with the clean model with different bank angles

# Chapter 5

# Modeling and Flight Performance Discussion

In this chapter, the discussion of the modeling and simulation assessments is presented. First, it is discussed whether the model is accurate and comprehensive enough. Then the flight performance of the model will be discussed based on the results from the previous chapter.

## 5.1 Accuracy and composition of the iced model

Obtaining an accurate model that can be used in simulations was one of the most essential tasks in this thesis. A combination of CFD analysis and analytical calculations obtains the model. The model equations are taken from accepted textbooks, and the two-point model is verified to correspond with the one-point model in the author's previous work [4]. Furthermore, the clean model is used as a base to develop the iced model. Here, the main focus has been to evaluate all coefficients that significantly impact flight characteristics.

Aerodynamic lift is the main parameter when it comes to aircraft stability. For instance, the HTP lift generates pitch stability, and it will thus be important to include the change in HTP lift due to ice when the iced model is to be obtained. Likewise, generate the VTP lift yaw stability and the dihedral roll stability. When all coefficients affected by ice accretion and contribute to stability are modeled, the model can be assumed to be complementary enough to represent the physical version.

### 5.1.1 Longitudinal model

The longitudinal model is likely the most accurate if it is to be favored. This favoritism is because the two-point model is custom-made to use static coefficients obtained from advanced CFD analyses. The lift coefficients and the corresponding pitch moment coefficient are calculated precisely for both airfoils in different icing conditions using high-performance computers. All of these coefficients are affected by ice and are important in terms of stability. As for the dynamic pitch damping coefficients, $C_{L_q}$ and $C^{\text{global}}_{m_q@P_W}$, they are modeled based on analytical calculations with variables $C^{W}_{L,\alpha}$ and $C^{H}_{L,\alpha}$, obtained from CFD analyses. Questions can be raised about the accuracy of these coefficient estimations, but they are the most applicable method that can be used given the origin of this thesis. In any case, only the estimated coefficients reductions form the iced model. The use of

reduction ratios strengthens the validity of the iced coefficients since none of the coefficients are calculated directly analytically.

### 5.1.2 Lateral model

When it comes to the iced lateral model, it is purely based on reductions from analytical expressions with lift reduction as the primary variable. Similarly to the derivatives in the longitudinal model, the analytical procedure is the most applicable for the lateral model. The lateral dynamics of an aircraft are more complex than the longitudinal, and therefore analytical expressions are used for modeling. The complexity originates from more strongly coupling in the dynamics. Roll, yaw, and sway lateral motions are interdependent in ways that the longitudinal motions of pitch, surge, and heave are not. For instance, the phenomenon known as adverse yaw is a classic lateral dynamics coupling example. *Adverse yaw* is a flight situation in which the aircraft yaws in the opposite direction to a roll input due to differential drag on the wings [16]. When a roll is initiated by deflecting the ailerons, the aileron that moves down increases the wing's lift and rises the wing up. The consequence of increased lift is increased drag, which results in a net moment that tends to yaw the aircraft in the opposite direction of the intended roll. This effect demonstrates the complexity of the lateral dynamics coupling and the challenges in modeling the coupling.

Modeling the iced model in this thesis focuses on including the ice affections of the main contributions to lateral stability. The included main contributions are how dihedral effects roll stability and how VTP affects yaw stability. Since the lateral dynamics of an aircraft is very complicated and extensive, other factors affect its stability in icing conditions.

Both Phillips [16] and Etkin [26] explain that dihedral is the main contributor to roll stability. The wing sweep angle and tail aerodynamics also play a role in roll stability. Wing sweep generates a dihedral effect when an aircraft rolls. The forwarded wing in a roll advances into the oncoming airflow, increasing its relative velocity. Increased relative velocity causes the forwarded wing to generate more lift, creating a restoring moment that tends to roll the UAV back to level flight. As lift is modeled proportional to the square of airspeed, this contribution becomes marginal for low airspeed, where the Falk operates. According to Bertin [27], swept wings were originally designed to prevent boundary-layer separation, a problem for high-speed aircraft. Boundary-layer separation is a problem that can cause increased drag, loss of lift, and potentially cause a stall condition. However, the Falk has a wing sweep angle of 18°, so a small contribution could be evaluated to obtain a more comprehensive model.

The tail aerodynamics also influence the roll moment through the forces generated by the VTP. As described in section 3.3.2, the VTP generates a force when the UAV sideslips, as illustrated in figure 3.5. The aerodynamic center of Falk's VTP is offset from the UAV's rolling axis. Thus the force will produce a rolling moment. The force depends on the VTP lift coefficient, which is affected by icing. With this in mind, the small contribution from VTP to the rolling moment could be included in the iced model, especially for noticeable sideslip angles.

Because lateral dynamics are complicated, neither lateral stability derivatives are modeled with respect to the reduction of lift slopes. It is generally possible to obtain estimates of the longitudinal aerodynamic derivatives with greater confidence than can usually be ascribed to estimates of lateral–directional aerodynamic derivatives [15]. Using flight test measurements is a more suitable approach for

pursuing these coefficients. A technique called *parameter identification* involves analyzing the responses of multiple variables at once, where the responses are obtained from actual flight tests. From this complex analysis, it is possible to create a complete estimate of the aircraft's mathematical model that includes all stability derivatives. *Parameter identification* is an analytical process in which full use is made of state space computational tools to estimate the aircraft state description that best matches the input–output response measured in flight. Essentially, it is a multi-variable curve fitting procedure. However, this method is complicated. Its success largely hinges on the correct choice of computational algorithm, which should suit the specific experiment. It is essential to remember that the flight tests must be done with natural ice accretion or some ice accretion replica on the UAV to obtain the most realistic coefficients. Since it is unknown how the ice will affect the aircraft, such a flight test entails great risk. It is uncertain where the stability margin is, and the chance of a crash increases significantly. On the other hand, the modeling done in this thesis is completely harmless to people and hardware, unfortunately at the expense of simplifications that reduce the iced model's accuracy. Nevertheless, the change in weight distribution has been taken into account, leading to a change in dynamics from the clean to the iced model.

### 5.1.3 Control derivatives

Of the eight control derivatives from the equations (2.1-2.6), are all of them modeled with regard to change in mass distribution, which also leads to a change in iced model dynamics. Furthermore, three of the eight are modeled with regard to lift reduction. This applies to $C_{m_{\delta e}}$, $C_{l_{\delta a}}$ and $C_{n_{\delta r}}$. Two coefficients, $C_{L_{\delta e}}$ and $C_{l_{\delta r}}$, are equal to zero, which makes them insignificant. This means that three coefficients remain the same for the iced model as for the weighted model. This applies to $C_{Y_{\delta a}}$, $C_{Y_{\delta r}}$ and $C_{n_{\delta a}}$. Of these coefficients, it is most likely $C_{n_{\delta a}}$ that has the greatest impact on stability margins. This coefficient relates to the adverse yaw effect that occurs when rolling with the ailerons. Unfortunately, due to the dynamic coupling, this coefficient is difficult to model with regard to ice. This also applies to the two other coefficients, representing the additional side force due to aileron and rudder deflection.

The aileron's, elevator's, and rudder's primary effects are rolling, pitching, and yawing the UAV. Closed loop stability of a UAV depends on these effects, and since they are the actuator's primary purpose, they are the most important to model.

### 5.1.4 Ice accumulation

As for the ice itself, it is modeled to accumulate on the airfoil leading edges and propeller. Ice can also accumulate on other surfaces, affecting the UAV's flight performance, for example, on the fuselage. Ice on the fuselage can disrupt the smooth airflow and potentially increase the parasitic drag. Additionally, icing effects from the winglets are not evaluated in the model. The winglets contribute to the UAV's characteristics, such as reducing vortex drag. To clarify, the iced model in this thesis does not include the effects of ice on fuselage or winglets. However, including these effects has led to a more comprehensive and accurate model.

## 5.2 Longitudinal performance

In essence, the simulations of the pitch step tests carried out in different icing conditions offers valuable insights into the Falk model's dynamic stability and control

characteristic. The test scenarios clean, iced wing, iced tail, and fully iced have been chosen to investigate where the ice affects flight characteristics the most. Knowing its limitations for a UAV to operate in icing conditions is essential. Being in possession of the limitations will help determine how much ice is accepted during a flight and determine the location of this accepted ice.

### 5.2.1 Clean scenario

Understanding the clean pitch step response is a fundamental prerequisite before investigating more complex iced scenarios. The core aspects of this response are anchored on the angle of Attack (AoA), elevator deflection, and the moments generated by the wing and tail. Starting in figure 4.1 where the clean flight dynamics parameters are shown in blue color. This figure shows plots from scenarios other than clean, but still, it is the clean scenario to be discussed. The pitch response in this figure is just an overview. Figure 4.4a is more suitable for a closer view of the pitch step response. Both figures show that the Falk model performs a pitch step from 0.25° to 20° pitch angle with no overshoot or stationary deviation. A consequence of a change in pitch is a change in the UAV's longitudinal axis with the relative airflow, thus a change in the AoA. Figure 4.1 shows that the AoA increases from 0.2° to a maximum of 4.8° during the pitch change. The elevator deflection plot shows how the elevator has to deflect upward (negative angle) to initiate the maneuver. This deflection leads to a reduced lift generated by the HTP. The HTP is designed to counterbalance the moment generated by the wing without the usage of elevator deflection. Balancing the aircraft without an elevator is preferred, as this preserves the elevator's availability for performing maneuvers. The state in which all the forces and moments acting on the UAV balance each other out, leading to a steady and stable flight without requiring any control input, is called trim state. When the HTP lift is reduced due to elevator deflection, the UAV is out of trim state, generating a nose-up pitch moment. This response is shown mathematically in equations (2.13) and (2.12), where the moment about CG depends on the lift at HTP. The generated moment about CG changes the UAV's pitch angle, consequently changing the AoA, subsequently altering the lift and moment from the wing. This interplay continues until the UAV achieves a new steady state. Because of this interaction, explaining a pitch response at a detailed level is extensive. Coefficients in the equations of motion depend on the AoA with different relationships. When the clean model's response is compared to the iced model, the coefficients also become dependent on the ice. Thus, the following comparisons present and discuss the most important contributions to the resulting responses.

### 5.2.2 Icing conditions at -6°C and 20 µm MVD

In figure 4.1, the clean model is compared with the model in icing condition at -6°. The MVD value has been chosen not to be noted further in this thesis since only $20\mu m$ have been used. One interesting observation in this figure is that the pitch response is slightly faster for the iced wing and fully iced scenario. This is despite the increased moment of inertia due to ice mass. It is easier to make this observation in the more focused figure 4.4a. The physical reason for this response is that the iced wing generates a significantly smaller nose-down pitch moment than a clean wing in angles of attack above 2°. This effect is shown in figure 3.2 where the static longitudinal coefficients are shown. The UAV is designed to obtain a trim state in clean condition. Thus, an imbalance occurs when the icing reduces the moment from the wing. This imbalance has to be compensated by the elevator to keep the correct pitch angle. The elevator deflection plot shows a

positive deflection before the pitch maneuver, which means that the HTP needs more lift, generating a nose-down moment about CG to keep a level flight. It can also be observed that the elevator deflection curves for the iced wing and fully iced scenario are almost identical. It might be expected that an iced HTP would necessitate a more significant elevator deflection, but this is not the case. The reason is that lift is not significantly reduced by ice accumulation on the HTP. The lift curve for the HTP is shown in figure 3.4, and it shows that the lift in all temperatures except -2°C is close to the clean curve. This is fortunate for the elevator since it does not need to compensate significantly more when ice is on the HTP.

As a result of the decreased wing lift due to the ice, the Falk model with an iced wing compensates by increasing the AoA. This is clearly shown in the figure where the AoA increases to a maximum of 8° for iced wing scenarios. An increase of AoA towards 10° leads to even more nose-down pitch moment reduction from the wing. Thus the elevator has to compensate even more by increasing its deflection through the pitch maneuver. At maximum, the deflection is 6°. Notably, the elevator saturates at 17° deflection downward. Thus there is a large downward saturation margin for the iced wing and fully iced scenario.

When it comes to the scenario where only the tail is iced, the wing will generate a similar nose-down pitch moment as the clean scenario since the AoA plot for the clean and iced tail scenario is quite similar. The AoA for the iced tail scenario is just slightly increased by 0.3° compared to the clean for compensating the small drag increase at the HTP. It is worth knowing that in level flight, the HTP produces some negative lift, i.e., downward force, to balance the aircraft. Figure 3.4 shows that when the HTP has a negative AoA, the downward force is degraded towards zero when it is affected by ice. As shown in figure 4.1, the elevator has slightly more deflection in level flight before the step. This deflection generates a slightly stronger downward force to balance the additional nose-up pitch moment due to increased HTP drag.

A more interesting observation in figure 4.1 is that the elevator must make a larger upward deflection to initiate the maneuver for the iced HTP scenario. This is mainly due to the reduced HTP lift curve, which determines the efficiency of the elevator, as shown in eq. (3.21). At a minimum, the elevator is deflected to -7.5°, and the limit is at -11.9°. Given this, the elevator is closer to saturation in this scenario than the ones with iced wings. This also means that the pitch response becomes somewhat slower, mostly due to the dynamics of the control surface.

At last, the figure shows a significant increase in motor speed for the iced wing and fully iced scenario. Their motor speed is almost identical, and the motor speed of the clean and iced tail scenario is almost identical. This emphasizes the importance of the wing's drag, and at the same time, the drag is insignificant for the tail. The full explanation for this involves the airfoil shape and ice structures, while the short explanation is that the wing has a much longer span than the tail. With regard to drag, the short explanation is sufficient for this thesis and will be used later when the path planner is to be presented.

For this specific type of icing, where the ice accumulates highly influences the problems encountered during the pitch maneuver. Ice on the wing causes a drastic increase in AoA, and thus drag. On the other hand, the elevator is closer to saturation when the ice is only at the tail, which appears to be the main problem for the iced tail scenario.

### 5.2.3 Icing conditions at -2°C and 20 µm MVD

The icing that occurs in -2°C with 20 $\mu m$ MVD has been chosen to be used in the test because of its characteristic as very fatal in terms of lift reduction and increased drag. Both of these characteristics are shown in figures 3.2 and 3.4.

Starting by investigating the performance of the scenario iced HTP, figure 4.2 shows that the pitch response is slower than the clean response. This is for the same reason as the previous icing condition: the elevator must be deflected more to provide the desired moment from the HTP. For this icing type, the elevator has to deflect to -9.5°, which leaves minimal margin against saturation.

Furthermore, investigating the iced wing and fully iced scenarios enlightens the severe implications that UAV icing can potentially incur. What happens in both of the scenarios is that the maneuver is initiated by an upward elevator deflection, as expected. Then the low nose-down pitch moment from the wing makes the UAV to change pitch angle quickly, consequently changing the AoA. With this type of icing, it is shown in figure 3.2 that the nose-down pitch moment from the wing quickly decreases for AoAs above 7° for the wing. This is equivalent to a longitudinal axis AoA of just 3° after taking account of the wing tilt angle. The figure shows that the longitudinal axis quickly reaches 3° AoA, and the increased nose-down pitch moment generated by the wing sends the elevator straight up into saturation (-12°). After the elevator saturates, the pitch angle and AoA start to oscillate. The AoA reaches values far from the CFD analyses span, and the simulated dynamic parameters are most likely unreliable. Thus the figure shows dashed curves after 50.5 seconds to present dynamics roughly after the elevator reaches saturation. The model balanced itself after several oscillations for almost 8 seconds in the simulations, yet this behavior is highly undesirable. Thus, elevator saturation is highly unacceptable for stable flight.

The tuning of the PID controllers plays a crucial role in the rate of actuator deflection, a point underscored by this test case. A pitch PID controller with a high proportional gain will aggressively deflect the elevator, thus rapidly altering pitch and AoA. Indeed, AoA is the most impactful variable in flight dynamics. However, it is worth noting that rapid AoA changes can also occur from variations in speed and wind conditions. Simulations like this provide valuable data on the operational limitations of the UAV.

Reducing the icing level from 1.0 to 0.4 for this type of icing gives the results in figure 4.3. These results have the same explanation as the previous test, where the moment from the wing increases drastically above AoA 7°. However, the elevator is able to compensate when the icing level is reduced. Nevertheless, the elevator is deflected completely upward to its limit, especially when the tail is iced together with the wing. Then, as is well known, elevator efficiency is also reduced. The figure illustrates that the aircraft successfully executes the maneuver, albeit with a more marginal approach and a slower response time than the clean model's response.

### 5.2.4 Longitudinal test findings

The analyses of the pitch step responses and associated aerodynamic variables reveal a significant variation in the effect of different icing conditions on the UAV's longitudinal performance. Such diversity arises due to the unique properties of each icing condition. Consequently, this impacts the stability margins and the behavior of the control surface, which varies across different icing conditions and

ice levels. This means there is no universal rule to predict the impact of ice accumulation on flight performance.

Furthermore, the findings emphasize that each icing scenario influences flight performance uniquely. Moreover, the favored scenario can shift based on specific icing weather conditions. Regarding elevator deflection margin, the iced wing scenario is favorable for the -6°C conditions, but the favorable scenario shifts to the iced tail for the -2°C condition. This would indicate the need for thorough case-by-case analysis if an IPS were applied to airfoils individually.

This is the start of understanding the Falk affections by ice, but further research is necessary to know how other icing types affect the UAV. Furthermore, research is necessary on how ice impacts more complex maneuvers.

## 5.3 Lateral performance

The steady coordinated turn response of an Unmanned Aerial Vehicle (UAV) under various icing conditions provides critical insights into its performance and handling characteristics. The motivation for conducting the lateral tests mirrors the longitudinal tests, which investigate the alterations in dynamics and limitations arising from icing. Like pitch step tests, roll step tests have been performed under the same icing conditions and scenarios. The steady coordinated turn is most suitable for changing the UAV's flight path while maintaining altitude, which makes it the ideal choice for the roll step test.

### 5.3.1 Icing conditions at -6°C and 20 µm MVD

The lateral iced model is primarily influenced by the reduction of VTP yaw stability and reduction of dihedral roll stability, together with the decreased control surface effectiveness and increased inertia. In figure 4.5, the iced model has a slower roll response compared to the clean model, which applies to all icing scenarios. When ranking the scenarios from slowest, the order is the fully iced, iced tail, and then the iced wing. The iced wing scenario has the most minor difference in sideslip angle, 0.2° from the clean scenario. Iced tail and fully iced have a significantly higher difference, 2°, which indicates that the VTP strongly influences reducing sideslip.

The simulations also reveal changes in control surface deflections. The elevator has to deflect upward for the iced wing and fully iced scenarios, just like in the pitch step test. The reasoning is also the same as in the pitch step test: the nose-down pitch moment from the wing is reduced, and the elevator has to compensate. Conversely, for the iced tail scenario, the elevator deflects more upward. The ice accumulation alters the balance of forces and moments in the longitudinal model, requiring compensatory defections to maintain level flight.

Aileron deflections have the most significant change for the fully iced scenario, while the separately iced wing and tail have an intermediate impact on the UAV's roll dynamics. Nevertheless, the aileron is at worst deflected -7.5°, while it reaches saturation at -12.3°.

The rudder's deflection also shows variations according to the icing condition. The iced tail and fully iced scenarios necessitate more significant rudder deflections than the iced wing scenario, which demands slightly more than the clean scenario. This reinforces the importance of the tail, specifically the VTP, in maintaining yaw

stability. Remarkably, the rudder is far from saturation. It saturates at 15°, but deflects only 1.4° at maximum for the fully iced scenario.

### 5.3.2 Icing conditions at -2°C and 20 µm MVD

The simulation results for the icing conditions at -2°C in figure 4.6 indicate an increase in the sideslip angle in the iced tail and fully iced UAV scenarios. The sideslip angle is far out of the CFD analyses span, and the flight dynamics parameters are shown in dashed curves after the reach of sideslip angle 10°.

Control surface deflections also exhibit significant variations across the different icing scenarios. Specifically, under full icing, the elevator reaches its maximum upward deflection, indicating saturation. The elevator almost saturates when the tail is iced. Notably, the ailerons reach saturation for both the iced tail and fully iced scenarios, which indicates that the ice is very severe in terms of stability.

Regarding rudder deflection, the most significant deflection is required for the iced tail case, followed by the fully iced scenario.

In the iced wing scenario, the roll response is just slightly slower than without ice, and with slightly more overshoot. Consequently, the sideslip angle is almost identical to the clean one. Regarding the control surfaces, the elevator deflects more downward, but far from saturation. The ailerons have to deflect 2° more compared to the clean scenario, and are deflecting at maximum -8°. Furthermore, the rudder deflects almost identically as to the clean scenario. All this makes icing only on the main wing less dangerous regarding roll stability. Nevertheless, the use of motor thrust increases considerably to counteract the increased drag.

The control surface saturations are avoided by applying the same decrease of the icing level approach as used in the pitch step test. The response and flight dynamics parameters may remind of the -6°C roll test but with a slower roll response and increased amplitude in sideslip angle and control deflections. In fact, the ailerons are nearly at their saturation point, suggesting that the aileron deflection might constrain the steady coordinated turn under this type of icing condition.

### 5.3.3 Lateral test findings

The type and level of icing are central for determining flight performance, mirroring the findings in the longitudinal test. Notably, regardless of ice type and icing scenario, the roll responses are slower. This is due to a higher moment of inertia and reduced control effectiveness due to ice accumulation.

Additionally, severe icing conditions could lead to saturations of two out of three control surfaces, posing a severe risk to stability. It becomes clear that control surfaces saturations absolutely limit the UAV's performance.

Finally, the impact of icing on the wing alone is less pronounced regarding lateral stability. However, ice on the wing, in combination with ice on the tail, constitutes the greatest danger. This implies that for executing a steady coordinated turn, prioritizing an IPS on the tail could be a beneficial strategy in the context of stability.

## 5.4 Actuator deflection in turn

The findings from the results in figure 4.8 indicate deviations in actuator deflections in a steady coordinated turn for the UAV when comparing clean and iced

UAVs. The most striking observation in this study is the saturation of the elevator for both ice types. This phenomenon can be attributed to a sudden increase in nose-down pitch moment from the wing. For the icing condition at -6°C, the elevator saturate for roll angles above 45°, and for the condition at -2°C and icing level 0.6, it saturates above roll angle 35°. The corresponding turn radius for these roll angles is shown in table 4.1.

There is a noticeable increase in deflection for the iced scenarios compared to the clean for both the aileron and rudder. This additional deflection is an intuitive observation of the reduced roll and yaw control effectiveness due to the ice accretion. Ice reduces the wing lift slope, and VTP lift slope, decreasing aileron and rudder control efficiency. Therefore, larger deflections are required to achieve the same control input effect as in clean conditions.

Moreover, the variation between the icing conditions provides an exciting insight into the effect of different ice types on the UAV wing and tail. The differences show that the ice type is a constraining factor in roll angles and turn radius, even when a ramp reference function gradually obtains the roll angle. Naturally, operating at the roll angle limit leaves no margin for disruptions like wind gusts.

# Part II

# Path Planning in Icing Conditions

# Chapter 6

# Path Planner Background Theory

This chapter presents the most important background theory essential to this second part of the thesis.

## 6.1 Previous work and contribution

Significant previous work that serves as the foundation for this part of the thesis is the contribution of Olsen [10] and Tiller [9], which is work on path planning for autonomous vehicles and weather data acquisition, respectively.

Olsen's work [10] demonstrated that an RRT* path planner for unmanned underwater vehicles (UUVs) could search for paths among fish cages in aquaculture. His implementation of the RRT* algorithm showcased a viable strategy for path planning in complex environments. The RRT* path planner designed by Olsen forms the basis of the work conducted in this study. This path planner is extensively modified and expanded in this thesis to include the Falk model and simulation. Furthermore, incorporating safety constraints for Falk operating in icing aerial conditions is considered.

The second crucial piece of previous work is the program developed by Tiller [9] for obtaining weather data. Tiller's program has the advantage of providing historical real-world weather data from the Norwegian Meteorological Institute (MET). This feature is critical for testing path planning in varied real-world weather. Tiller based his work on previous studies [28] and [29] where he tested the usage of the Particle Swarm Optimization (PSO) algorithm for path planning in icing conditions.

This thesis integrates Tiller's weather data program with the RRT* path planner to create a comprehensive system that considers real-world environmental variables.

## 6.2 Weather Modeling

The complete description of how the weather is obtained from MET is found in [9]. The most important part of this thesis is the icing condition modeling given by [28]. This modeling involves setting icing conditions as a binary variable. This means that there either are icing conditions, or there are not [9]. The binary variable, denoted $I$, is modelled according to [28] as

$$I = (T < 0°\text{C}) \wedge (\phi_r > 0.99) \wedge (\text{LWC} \geq 0.01g \cdot m^{-3}) \tag{6.1}$$

where $\wedge$ is the logical *and* operator, $T$ is the air temperature, $\phi_r$ is the relative humidity, and LWC is the liquid water content. How the different variables are calculated according to the MET weather data is described in [9]. Nevertheless, the explanation of how an icing condition occurs is simple. The air temperature has to be below 0°C, relative humidity above 99%, and LWC above 0.01 g per $m^3$.

## 6.3 Rapidly Exploring Random Trees

The algorithm, Rapidly Exploring Random Trees (RRTs) [30] explores the free space by generating a tree structure that spans the entire region of interest through random sampling. There are many RRTs variants, and all of them are based on the same basic principles. These basic principles will be reviewed in the following subsection, before the variant RRT* and its implementation are reviewed in the next subsection.

### 6.3.1 RRT

The basic RRT is a fairly straightforward path-planning algorithm that can be graphically reviewed. The algorithm starts by constructing a tree rooted at the start point. The tree expands iteratively by choosing a random point in the free space and connecting it to the nearest node in the tree. The random point is adjusted relative to the nearest node to compact the tree. The connection of the new point is made by following a feasible path that avoids any obstacles in the space. If the connection is successful, the random point becomes a node of the tree. The process of connecting random points to the tree is repeated until the goal point is reached, or another termination criterion is met. If the algorithm is terminated and the goal is found, the path can be obtained by tracing the parent nodes from the goal point backward to the start point.

List of RRT main steps:

1. **Initialize tree** rooted at start point.
   The free space span is also initialized with constraints $\left[c^i_{min}, c^i_{max}\right]$ where $i \in [x, y, z]$ denoting the axes in three dimensions.
2. **Sample a random point** in the free space.
   The random point $\mathbf{q}_{rand}$ has to lie in the free space $C_{free}$. Hence the random point can be found by
   $$\begin{aligned} q^i_{rand} &= \text{rand}(c^i_{min}, c^i_{max}), \quad i \in [x, y, z] \\ \mathbf{q}_{rand} &= \left[q^x_{rand}, q^y_{rand}, q^z_{rand}\right] \end{aligned} \tag{6.2}$$
   where the rand$(\cdot)$ function chooses a random number between its two arguments.
3. **Find the nearest node** in the tree to the sampled random point.
   This step is done by calculating the distance between the random point and all the points in the tree. The node with the shortest distance is, of course, the nearest node. Mathematically the node is found by
   $$\mathbf{q}_{nearest} = \text{argmin}\{||\mathbf{q} - \mathbf{q}_{rand}||\}, \quad \mathbf{q} \in \mathbf{T} \tag{6.3}$$
   where $\mathbf{q}$ is a node in the tree $\mathbf{T}$.
4. **Adjust the random point** relative to the nearest node.
   This step is for reducing the maximal length of the tree branches to a tuneable length $\epsilon$. If the distance $d$ from the random point to the nearest node

is longer than the maximal branch length, the random point is adjusted to

$$\mathbf{q}_{new} = \mathbf{q}_{nearest} + \frac{\epsilon}{d}(\mathbf{q}_{rand} - \mathbf{q}_{nearest}) \tag{6.4}$$

and if the distance is shorter than the maximal branch length, the random point is not adjusted

$$\mathbf{q}_{new} = \mathbf{q}_{rand} \tag{6.5}$$

5. **Try to connect** the nearest node to the adjusted random point with a feasible path that avoids obstacles. If the path is not feasible or does not avoid obstacles, start from step 2. This step is also somewhat misleadingly called collision avoidance. An obstacle does not necessarily have to be a physical object which leads to a collision by hitting it, but can be an area that is desired to be avoided. The collision avoidance algorithm for circular areas is explained in [10].
6. **Add the adjusted random point** to the tree as a node if the connection is successful.

   $$\mathbf{q}_{new} \in \mathbf{T}$$

   This results in a tree with one more node, and the algorithm has explored more of the free space.
7. **Repeat step 2-6** until goal is found or termination criterion is met.
8. **Trace the parent nodes** from goal to start to obtain path.
   When the algorithm has terminated and a path is found, the path extraction is done by tracing all parents from the goal to the root parent, which is the start. Reversing this path gives the path from start to goal.

### 6.3.2 RRT* (RRT-star)

RRT* is a more advanced version of the RRT algorithm, with the primary objective of improving efficiency and optimality. Paths found by RRT* are called near-optimal paths because of the algorithm's ability to discard sub-optimal paths. Instead of only connecting the sampled random point to the nearest node in the tree, RRT* tries to connect it to the node that results in the lowest path cost. It is essential to know the lowest cost to every node to achieve this reconnection. The cost between nodes guides the expansion of the tree towards a near-optimal path. To know the lowest cost to every node, it is necessary to consistently evaluate the costs when a new node is added to the tree. This step is called rewiring and allows the exploration of new areas of the free space more efficiently, which can improve the solutions.

In steps, the expansion to RRT* follows after step 6 of RRT. The steps are illustrated in figure 6.1, which will help with understanding. Figure 6.1a shows a tree that has expanded over five iterations. The tree has found a path from start to goal around the obstacle on the downside. If the cost is calculated as a function of distance, it is clear that a more cost-effective path runs on the upper side. All nodes have an associated cost shown in red beneath the node. A random point is sampled above the obstacle and is about to be evaluated by the algorithm. In figure 6.1b, the sampled random point has been connected to the nearest node, 4, and is now a part of the tree. The illustration series is to show how the RRT* works when a more cost-effective path appears.

1. **Cost calculation** of the newly added node. This is done by calculating the cost from the nearest node to the newly added node and adding this cost to the cost of the nearest node. As shown in figure 6.1b, the new node has been

assigned a cost of 3.5. The new node's neighborhood is also shown as a light blue circle around it. The neighborhood in this illustration is calculated as $N = 1.1\epsilon$, where $\epsilon$ is the step length.

2. **Rewire the new node** if any other node in the neighborhood of the new node gives a lower cost for the new node. All nodes in the neighborhood of the new node are seen as candidates to serve a lower cost to the new node. Therefore, the cost from every node in the neighborhood to the new node is calculated and evaluated. The node serving the minimum cost is rewired to be the parent node to the new node. This node is called the lowest-cost parent. In figure 6.1c, it is shown that the start node is within the new node's neighborhood, and it serves the new node at a lower cost. The start node is the lowest-cost node and becomes the new node's parent.
3. **Rewire the new node's neighborhood** if the new node serves a lower cost to any node in the same neighborhood. The cost from the new node to all nodes in the neighborhood, except the parent node, is calculated and evaluated. If the new node serves a lower-cost path to any of the nodes, the new node becomes the parent node to it. The node which gets its cost reduced is called the reduced-cost node. All children nodes of the reduced-cost node must get their cost reduced by the same amount. Figure 6.1c shows that node 4 is within the new node's neighborhood, and therefore the algorithm evaluates whether node 4 should be updated. An update is clearly the case, and figure 6.1d shows that node four has been rewired to have the new node, node 6, as the parent. The associated cost of the node has been reduced. This also applied to the children's cost, which in this case was the goal node. The goal node had a cost reduction of 1.5, implying that the best path had a cost reduction of the same amount.

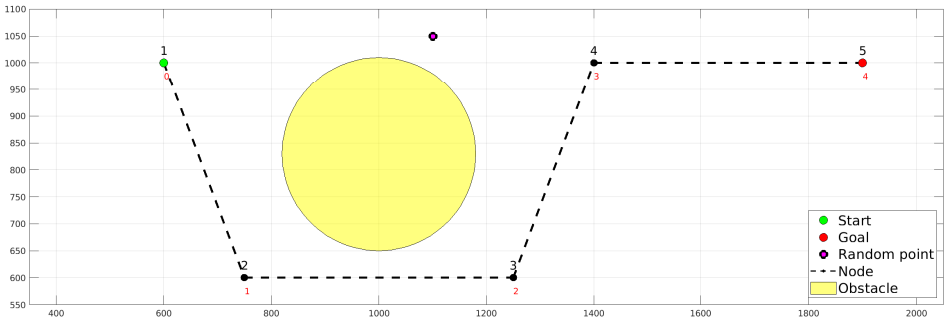


**(a)** Existing tree have found a path from start to goal around the obstacle

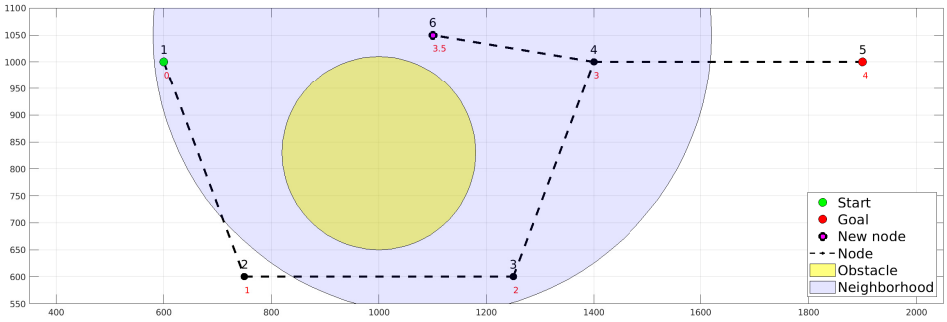


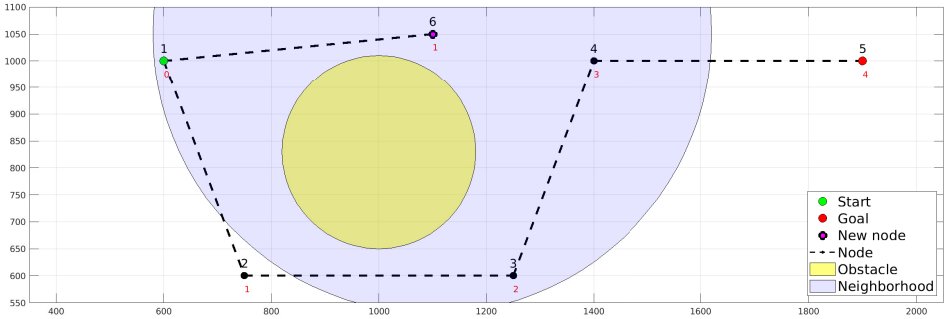


**(c)** The lowest cost to the new node has been found, and the new node has been added

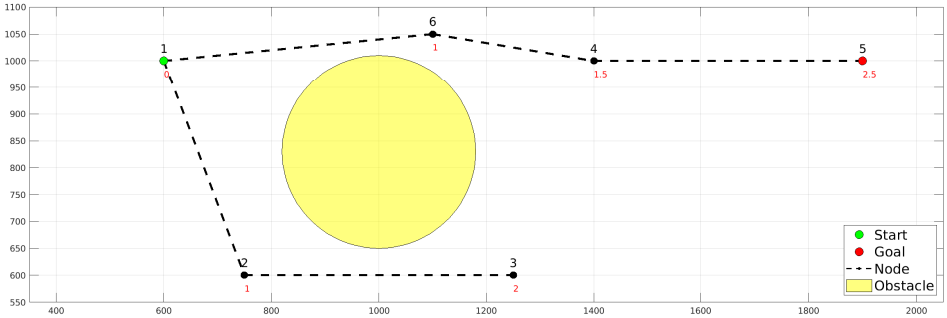


**(d)** All neighbors of the new node have been evaluated, and node 4 got a cost reduction by rewiring to have the new node as parent

**Figure 6.1:** Illustration series of how the rewiring step in RRT* works

# Chapter 7

# Path Planning Through Icing Weather

As witnessed in the previous part of this thesis, ice accretion significantly impacts Falk's model flight performance. For some icing conditions, the simulation even indicated unstable flight. Path planning that omits icing conditions when necessary can be helpful in reducing the risk of instability. In more encouraging words, sufficient path planning can ensure a safe and efficient operation for the UAV model in icing weather.

Path planning refers to the process of determining the optimal path for a UAV to follow based on various factors such as weather conditions, obstacles, and mission objectives. In icing conditions, path planning for UAVs involves identifying areas with potential icing hazards and determining the most efficient path to avoid them. For instance, a UAV can be programmed to avoid flight in conditions with low temperatures and high air humidity, which are prone to icing.

Furthermore, path planning can help reduce the UAV's energy consumption, which is critical in icing conditions where the battery capacity can be significantly reduced due to cold temperatures. Battery-powered UAVs will always have battery capacity as a limiting factor. Specific to Falk, it can carry two to five battery packs, which means that the required capacity from the path planner can be inserted before a flight. Of course, provided that the required capacity is below the maximum capacity.

By utilizing a path planner algorithm that optimizes with regard to energy consumption and icing, the UAV can fly the most energy-effective path that avoids icing hazards. A sufficiently accurate UAV model is crucial to plan such an optimal path. The aircraft model needs the ability to be simulated in icing conditions. The effect of icing on the UAV's energy consumption and aerodynamics is crucial for the path planner to work. Further in this part of the thesis is the Falk model derived in chapter 3 used for path planning.

## 7.1 Implementation of path planner

The implemented path planner algorithm is RRT*, explained in detail in 6.3. According to [31], the RRT* algorithm is suitable for UAV path planning in complex environments. The algorithm has been proven asymptotically optimal and has low algorithmic complexity in 3D space.

### 7.1.1 Mission objective

Simply put, the path planner's objective is to find the path from start to goal that require the least energy and avoids consequences due to ice. There are multiple techniques to avoid ice consequences without changing the path for UAVs, where one of the most used for small UAVs is electrical heating systems [1]. This preferred technique is due to the lower weight and fewer mechanical parts for the electrical heating system compared to the other techniques. This part of the thesis explores the possibilities of using an advanced path planner to get the Falk to complete its mission without using anti-ice or de-ice systems. Running a path planner instead of anti-ice or de-ice systems have the advantages such as

- **Lower complexity** to the overall design of the UAVs. Electrical heating elements with required wiring must be thoroughly integrated into wings, stabilizers, and propellers. This integration will make maintenance and repairs more difficult and time-consuming. All of this could be avoided by using an advanced path planner.
- **Possibly reduced power consumption** due to avoiding electrical heating, which must be drawn from the battery. Electrical heating can be challenging for UAVs that rely on limited battery capacity.
- **Reduced cost** due to less complex design and building. Fewer components and less maintenance do add some extra cost reduction as well.
- **Reduced weight** due to avoidance of the heating elements and wiring. Weight reduction can improve payload capacity, flight time, and even flight performance.
- **Reduction of potential hardware failures.** Hardware failure can lead to damage, injury, and mission incompleteness.

It is clearly expressed in section 6.3 that the cost calculation in RRT* is crucial. The cost used in the path planner is the amount of energy used. Calculation of the energy used is done according to eq. (2.34) in simulation. For the path planner to find a safe path, it must know the limitations of the UAV [32].

In the case of the Falk model, a flight maneuver can be simulated and analyzed to determine whether it is feasible. The results from the previous part give the constraints for the path planner. The path planner's constraints are generally determined based on flight performance, weather, and terrain limitations. The implemented constraints are as follows

1. **Icing time**. The maximum time the Falk model is exposed to icing conditions on a path is constrained, denoted $T_{i,max}$. Since the CFD analyses have been done for an icing time of 21.5 minutes, the most realistic maximum time will be this time.
2. **Turn angle**. The maximum turn radius is obtained as done in 4.8. The path planner can discard paths containing turns that are not feasible with regard to roll angle. As the path planner also searches for the most energy-efficient path, it is implausible that the path contains sharp turns. It is thus sufficient to have the lowest turn angle as a constraint throughout the path planning.
3. **Actuator saturation**. The path planner discards paths that require control surface deflections more than physically possible. Adding a deflection margin to add more safety margin is also possible.
4. **Obstacle avoidance**. In aviation, there are lots of constraints and rules to follow. One of the constraints is to avoid certain geographical areas. The path planner discards a near-optimal path candidate if it crosses such an

area. Another constraint can be the height above ground, which has to be constrained according to rules in aviation.

5. **Terrain**. The terrain and vegetation can be seen as constraints that must always be taken into account. The implemented way to avoid terrain obstacles is to keep a desired constant height above ground.
6. **Airspeed**. The simulator does not handle airspeeds higher than 35 m/s. Thus a path is infeasible if the airspeed reaches such value.

This thesis has yet to focus on the battery capacity of the Falk, so no limitation has been entered for total flight time or distance.

### 7.1.2 Acquisition of weather data

Weather data must be retrieved in advance of path planner execution with the program from [9]. This program retrieves data for a given date and geographic area and saves it in an NC-file. In this file, data is stored as a matrix with corresponding indices for coordinates and values for weather data. If the position of the UAV is known, weather data for that position can then be retrieved. The resolution is 2.5 km × 2.5 km, which leads to a search for the nearest stored coordinate.

### 7.1.3 Application of Falk simulator

Every iteration in the path planner algorithm involves a simulation of the Falk model. It is important to remember that the tree expands with just one branch in the free space for every iteration. This branch is a straight line between two nodes, $\mathbf{q}_{from}$ and $\mathbf{q}_{to}$. This straight line and all other branch candidates for the iteration are simulated. The Falk simulator initializes with the straight line as a mission for every branch candidate with the weather data obtained from the NC file. The initialization involves orientating the Falk in the direction of the straight line. The yaw angle is initialized according to

$$\begin{aligned} \mathbf{p}_{par} &= \mathbf{q}_{to} - \mathbf{q}_{from} \\ \psi_{init} &= \text{atan2}(\mathbf{p}_{par,2}\,,\, \mathbf{p}_{par,1}) \end{aligned} \tag{7.1}$$

where $\mathbf{p}_{par}$ is a vector parallel to the straight line, and $\psi_{init}$ is the yaw angle. The pitch angle is initialized according to

$$\begin{aligned} \mathbf{p}_2 &= \mathcal{R}_{z,\psi_{init}} \mathbf{p}_{par} \\ \theta_{init} &= -\text{asin}(\mathbf{p}_{2,3}) \end{aligned} \tag{7.2}$$

where $\mathbf{p}_2$ is the parallel vector $\mathbf{p}_{par}$ rotated the angle $\psi_{init}$ around the $z$-axis, and $\theta_{init}$ is the pitch angle.

The weather and ice level are initialized as the state is in the first node of the line. The weather is also assumed to be constant throughout the mission. This assumption is based on a short branch length relative to the weather data resolution. Since the resolution of weather data is 2.5 km × 2.5 km [9], it is reasonable to assume that the weather is constant during a mission if the length is much less than 2.5 km.

Two crucial parameters that define the icing characteristics in the simulation are the ice accumulation rate and LWC. The ice accumulation rate indicates how long the model has to be exposed to icing conditions before the icing level reaches 1. Thus, the rate, $A$, have to be set to

$$A = \frac{1}{T_{i,max}}$$

where $T_{i,max}$ have to correspond with the CFD analyses icing time.

The LWC is a variable in calculating the ice accumulation on the propeller in eq. (2.38), and have to be the same as in the used icing type on UAV airfoils. Ideally, the LWC retrieved from the weather data determines icing conditions and propeller ice accumulation. However, the path planner is implemented to handle only one predetermined type of icing. This limitation is further discussed in chapter 9. Regardless, at this point of the path-planner testing, setting the LWC equally for airfoil and propeller icing is important.

### 7.1.4 Examine near-optimal path

The near-optimal path found by RRT* is evaluated based on the simulation of straight-line segments, leaving the potential for unforeseen problems over the whole path. In order to examine the path thoroughly, the implementation in this thesis includes a simulation of the entire path. This simulation ensures that the identified flight path remains feasible even when assessed as a continuous path rather than a series of segments.

A vital aspect of this simulation is the evaluation of potential control surface saturation. As identified from chapter 4, control surface saturation poses a significant challenge for UAV operation. If the execution of the chosen flight path leads to control surface saturation, the path is deemed infeasible, and alternative paths must be considered.

### 7.1.5 Pseudocode

The implemented RRT* algorithm is shown as pseudocode in Algorithm 1. $\boldsymbol{S}_{init}$ includes all parameters necessary for simulation. The parameters are icing scenario, weather data, icing formation, max icing time, max control surface deflections, and the Falk model. The tree initialization with $\boldsymbol{Q}_{init}$ includes start and goal position, environment span, and obstacles.

**Algorithm 1** RRT* Algorithm

**procedure** RRT*($\boldsymbol{S}_{init}, \boldsymbol{Q}_{init}, \boldsymbol{T}, C, K, \epsilon$)
  InitializeSimulator($\boldsymbol{S}_{init}$)
  $\boldsymbol{T} \leftarrow$ InitializeTree($\boldsymbol{Q}_{init}$)
  **for** $k \leftarrow 1$ to $K$ **do**
    $\boldsymbol{q}_{rand} \leftarrow$ SampleRandomPoint($C$)
    $\boldsymbol{q}_{nearest} \leftarrow$ FindNearestNode($\boldsymbol{T}, \boldsymbol{q}_{rand}$)
    $\boldsymbol{q}_{new} \leftarrow$ AdjustRandomPoint($\boldsymbol{q}_{nearest}, \boldsymbol{q}_{rand}, \epsilon$)
    Simulate($\boldsymbol{q}_{nearest}, \boldsymbol{q}_{new}$)
    **if** CollisionFree($\boldsymbol{q}_{nearest}, \boldsymbol{q}_{new}$) **then**
      $\boldsymbol{T} \leftarrow$ AddNode($\boldsymbol{T}, \boldsymbol{q}_{new}$)
      $\boldsymbol{q}_{min} \leftarrow \boldsymbol{q}_{nearest}$
      $\boldsymbol{Q}_{near} \leftarrow$ FindNearNodes($\boldsymbol{T}, \boldsymbol{q}_{new}$)
      **for** $\boldsymbol{q}_{near} \in \boldsymbol{Q}_{near}$ **do**
        Simulate($\boldsymbol{q}_{near}, \boldsymbol{q}_{new}$)
        **if** CollisionFree($\boldsymbol{q}_{near}, \boldsymbol{q}_{new}$) **then**
          **if** Cost($\boldsymbol{q}_{near}$)+Cost($\boldsymbol{q}_{near}, \boldsymbol{q}_{new}$) < Cost($\boldsymbol{q}_{min}$)+Cost($\boldsymbol{q}_{min}, \boldsymbol{q}_{new}$) **then**
            $\boldsymbol{q}_{min} \leftarrow \boldsymbol{q}_{near}$
          **end if**
        **end if**
      **end for**
      $\boldsymbol{T} \leftarrow$ ConnectNodes($\boldsymbol{T}, \boldsymbol{q}_{min}, \boldsymbol{q}_{new}$)
      **for** $\boldsymbol{q}_{near} \in \boldsymbol{Q}_{near}$ **do**
        Simulate($\boldsymbol{q}_{new}, \boldsymbol{q}_{near}$)
        **if** CollisionFree($\boldsymbol{q}_{new}, \boldsymbol{q}_{near}$) **then**
          **if** Cost($\boldsymbol{q}_{new}$) + Cost($\boldsymbol{q}_{new}, \boldsymbol{q}_{near}$) < Cost($\boldsymbol{q}_{near}$) **then**
            $\boldsymbol{T} \leftarrow$ ReconnectNodes($\boldsymbol{T}, \boldsymbol{q}_{new}, \boldsymbol{q}_{near}$)
          **end if**
        **end if**
      **end for**
    **end if**
  **end for**
  $path \leftarrow$ ExtractPath($\boldsymbol{T}, \boldsymbol{Q}_{init}$)
  **return** $path$
**end procedure**

# Chapter 8

# Path Planner Results

This chapter presents the results after executing the path planner in artificial and real-world environments.

## 8.1 Path planner in artificial environment

This section presents the results of the path planning algorithm from chapter 7 for two separate test cases. The primary objective of these test cases is to evaluate the performance and adaptability of the proposed path planner. In the later discussion of the tests, the algorithm's capability to avoid icing conditions while maintaining a balance between cost-efficiency and safety will be involved.

The path planner has been executed in two different artificial environments. This approach gives a simple overview of how the path planner explores the space, as well as being able to highlight its capabilities. Icing areas, winds, temperature, liquid water content (LWC), and terrain are the essence of constructing an artificial environment replicating a real-world environment. The following table 8.1 describes the construction of the environments and how the environments later are illustrated in colors.

The icing accumulation rate in table 8.1 means that ice accumulates 10 times faster than it did in this thesis's previous part's analyses. To give the propeller a 10 times faster accumulation rate as well, the LWC set 10 times higher. In all path planner tests, ice accumulates on the wing and tail, equivalent to "fully iced" from part **I**. As for the propeller, it is generally exposed to icing, but one simulation has also been made where icing is neglected on the propeller.

After running the path planner through the first artificial environment, the result is presented in figure 8.1, where the green path is found after 180 iterations. The figure shows how the RRT* has explored the space. All dashed lines are alternative paths the algorithm has evaluated. In this execution is propeller icing neglected. Table 8.2 shows the path planner parameters.

Figure 8.2 shows four different path trajectories, where two of the paths are found by the path planner. The dark green trajectory is from simulating the path in figure 8.1. The dark blue trajectory is from simulating the near-optimal path found by the path planner when ice also accumulates on the propulsion propeller. This path uses the same nodes as in figure 8.1. The remaining light green and red trajectories are trajectories of two manually plotted paths. These paths avoid obstacles but have no information about the weather conditions. One of the manual paths

| Parameter | Environment 1 | Environment 2 |
|---|---|---|
| Ice accumulation rate | Ice level rate of change is set to 1/120 s, which means that icing level 1 is reached after 120 seconds. Grey areas indicate icing areas. | |
| Wind | The northwest segment has winds from the west, and the southwest segment has winds from the east. The west wind area is colored green, and the east wind area is red. All winds have a magnitude of 5 m/s | The south red area have strong wind from the north with a magnitude of 14 m/s |
| Temperature | -6°C in the entire space | -6°C and -20°C |
| LWC | 5.1 $g/m^3$ | 5.1 $g/m^3$ and 2.13 $g/m^3$ |
| MVD | 20 μm | 20 μm |
| Terrain | Flat ground | 30 m elevation in the green area |
| Physical obstacles | There are three obstacles that can be seen as upright cylinders in the space. They are illustrated with yellow color | None |

**Table 8.1:** Description of every parameter that builds the artificial environments used for path planner test.

| Parameter | Description |
|---|---|
| Step length | 500m |
| Neighborhood region | 1.8×step length |
| Max. icing time | 120s |
| Desired height above ground | 300m |

**Table 8.2:** Path planner parameters of execution in artificial environments

goes on the north side of the obstacle, while the other is on the south side. Some selected results from the simulations of the paths are shown in table 8.3.

Figure 8.3 shows the resulting trajectories after simulating the found paths in the second artificial environment. The path planner has searched for the near-optimal paths when the icing area represents two different icing conditions. The green trajectory is simulated when the icing area has a temperature at -6°C and LWC at 5.51 $g/m^3$, while the blue have an icing area at -20°C and LWC at 2.13 $g/m^3$. Moreover, the red area has strong winds at 14 m/s, and the green area has a ground level 30 meters higher than the rest.

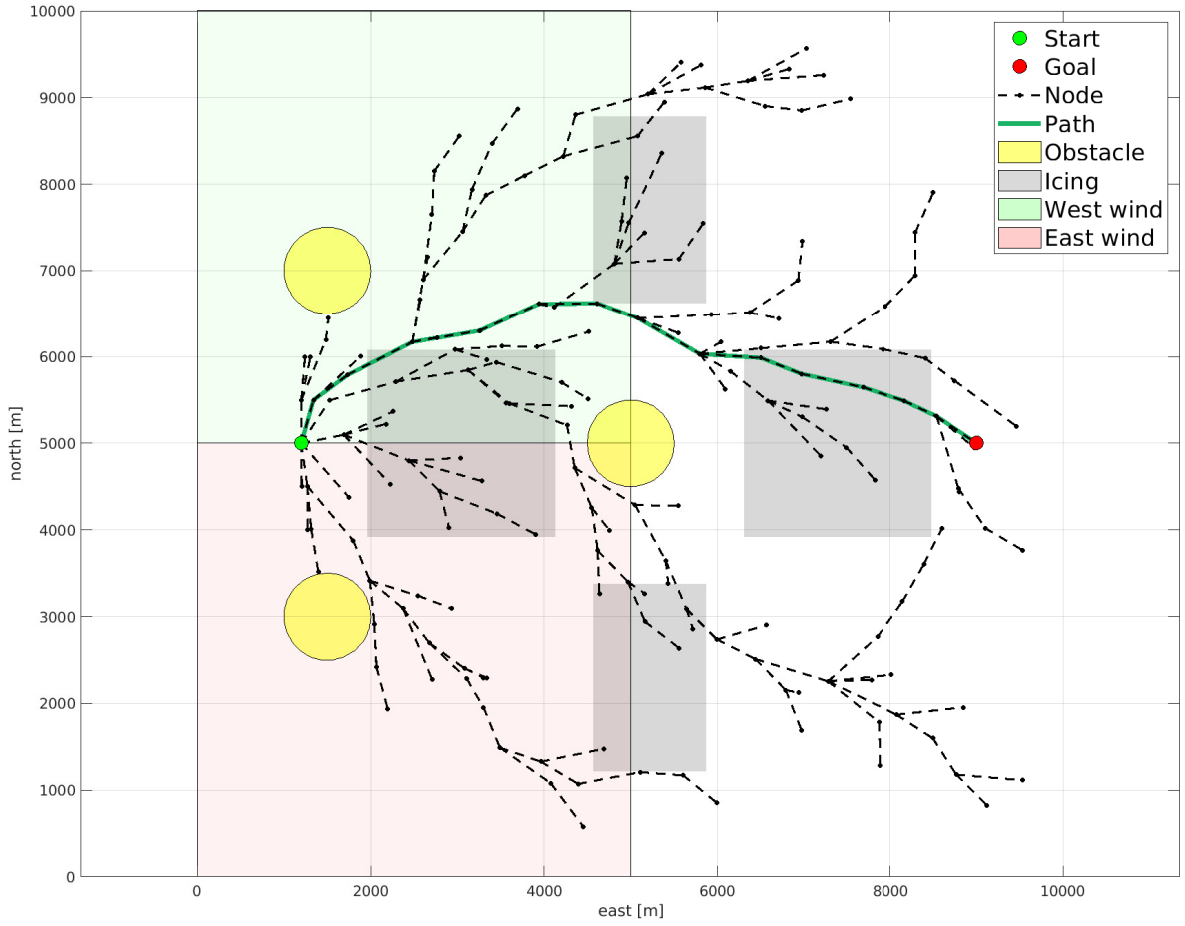


**Figure 8.1:** Path planner tree expansion in artificial environment 1 after 180 iterations.

| | Cost [Wh] | Flight time [s] | Icing time [s] |
|---|---|---|---|
| Path Planner (clean prop.) | 19.13 | 400 | 108 |
| Path Planner (iced prop.) | 19.42 | 421 | 22 |
| Manually north | 21.71 | 383 | 91 |
| Manually south | 29.98 | 503 | 107 |

**Table 8.3:** Results after simulation of four different paths in artificial environment 1. Corresponding trajectories are found in figure 8.2. Two paths are found by the path planner, where one is done without propeller icing and the other with propeller icing. The other two paths are manually plotted concerning avoiding obstacles but not concerning the weather.

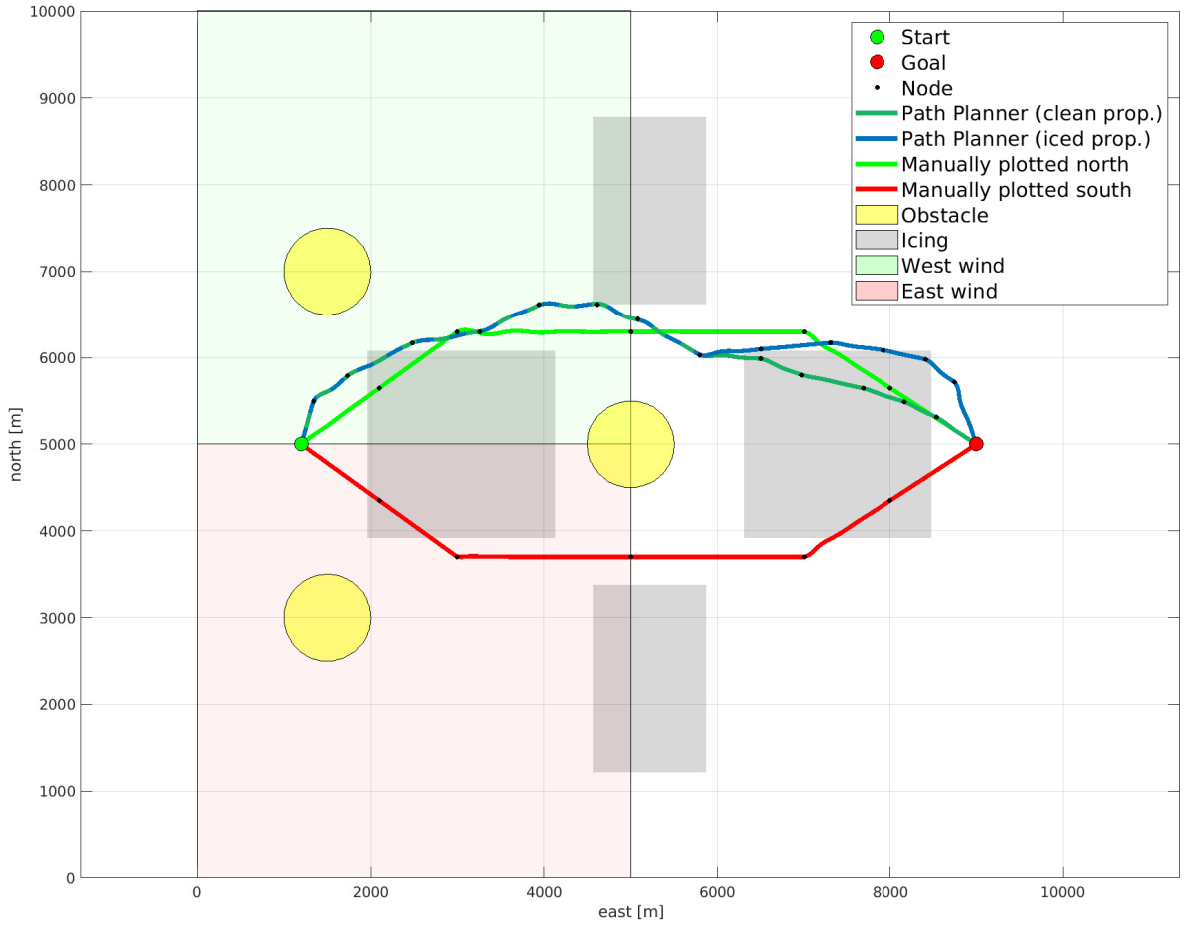


**Figure 8.2:** Four different simulation trajectories in artificial environment 1. The trajectories from simulating the best paths found by the path planner are compared with the simulation of two manually plotted paths. The dark green colored path is found when the propulsion propeller is clean, and the blue path is found when ice accumulates on the propeller in icing areas.

| | Cost [Wh] | Flight time [s] | Icing time [s] |
|---|---|---|---|
| Path Planner (-6°C) | 21.64 | 429 | 0 |
| Path Planner (-20°C) | 20.89 | 382 | 105 |

**Table 8.4:** Results after simulation of two different paths in artificial environment 2. The path planner finds the green path when the temperature is -6°C and LWC is 5.1 g/m$^3$, while the blue path is found at -20°C and LWC 2.13 g/m$^3$.

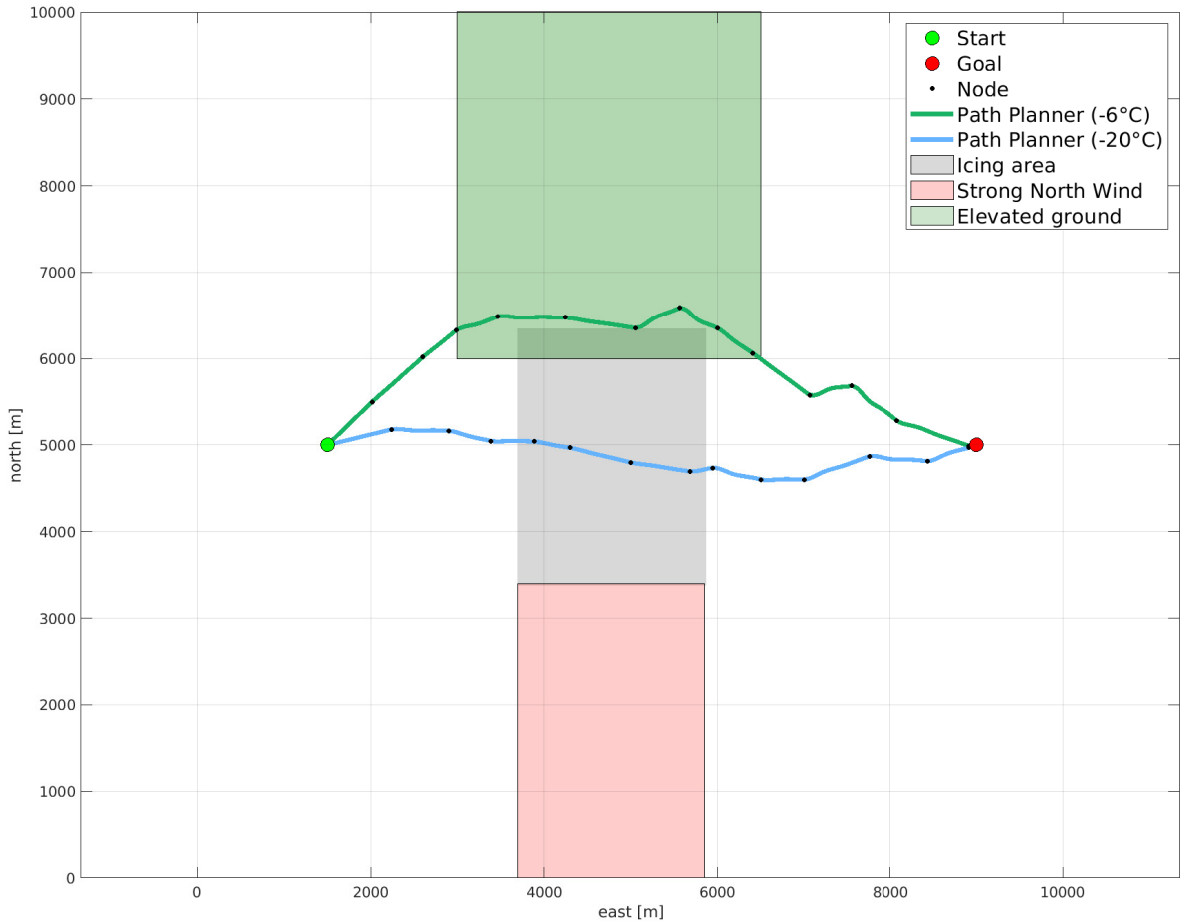


**Figure 8.3:** Two different simulation trajectories in artificial environment 2. The trajectories are from simulating the best paths found by the path planner after 120 iterations when the icing area has different characteristics.

## 8.2 Real world mission

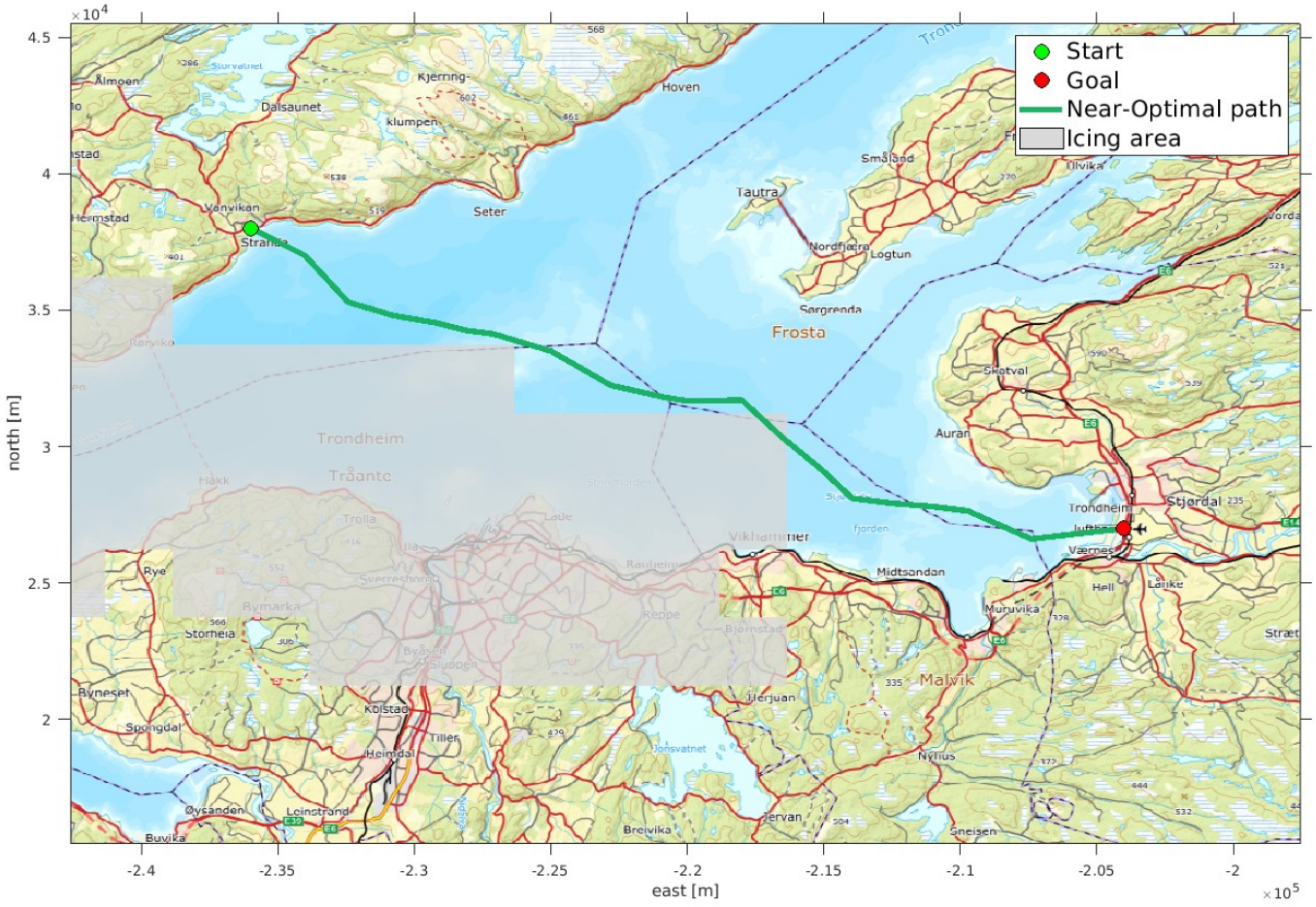


**Figure 8.4:** Pathplanner tree expansion in a real environment after 150 iterations.

Figure 8.4 shows the result after testing the path planner in real-world weather conditions. The weather is historical and obtained from MET on the 14th of January, 2023. The mission is to fly from Vanvikan to Stjørdal over Trondheimsfjorden in Norway. The icing condition area is shown in gray, and the path found by the path planner is shown in dark green. Simulation of the path resulted in a power consumption of 100,5 Wh and an icing time of 105 seconds. Table 8.5 shows the path planner parameters. The wind in the area is generally from the southwest, and the wind strength is around 5m/s at the start of the path but calms down to around 2m/s towards the end.

| Parameter | Description |
|---|---|
| Step length | 1500m |
| Neighborhood region | 1.8×step length |
| Max. icing time | 1200s (20min) |
| Desired height above ground | 300m |

**Table 8.5:** Path planner parameters of execution in real-world environment

# Chapter 9

# Path Planner Discussion

The research findings regarding implementing and testing the RRT* algorithm for determining a near-optimal flight path for Falk through icing conditions present meaningful content to the field of autonomous UAV path planning. This chapter will discuss the results detailed in Chapter 8.

## 9.1 RRT* Algorithm's Path Planning Capabilities in Icing Conditions

An RRT* algorithm in an icing weather path planner is tested in two artificially constructed environments specifically designed to emphasize the path planner's capabilities. The testing yielded interesting results and potential directions for future work.

### 9.1.1 Test case 1

In figure 8.1, where the search for a path through artificial environment 1 is shown, icing accumulation on the propeller is absent. The path planner effectively found a path that used the west wind advantageously as a tailwind. The planner also strategically avoided early icing but tolerated some icing toward the end of the path. This strategy could be interpreted as the planner's inherent trade-off mechanism, where it intentionally avoids the potentially initial icing risk but accept a certain degree of icing towards the goal. This approach can be seen as the planner's attempt to optimize energy consumption since it constantly searches for paths that use the least energy. The last leg through the icing area is a trade-off between flying with ice accumulation or spending more airtime by flying around the icing area.

Figure 8.2 shows four different simulation trajectories. The two trajectories from the path planner are clearly different towards the end. When icing also accumulates on the propeller in icing conditions (blue trajectory), the path planner avoids most of the last icing area by flying around the north side. The increased energy consumption due to propeller icing leads to the choice of flying around the icing area instead of through it. This choice highlights the importance that icing on the propeller needs to be modeled, as it significantly affects the resulting path.

Looking at table 8.3, it can be seen that the clean propeller case required the least energy use. Since this is an unrealistic case, as icing on the propeller is a fact in icing conditions, comparing the three other trajectory results is more interesting.

From table 8.3, it turns out that the path planner found a path that used 2,29 Wh less energy compared to the path manually plotted on the northern side of the obstacle. Still, the northern manual path was 38 seconds faster. The southern manual path used significantly more energy and time than the other paths. This result makes it clear that manual plotting of paths without information about the weather can severely impact time efficiency and energy usage. Manual path planning without information about the weather can, of course, also lead to undesirably high ice accumulations and instabilities.

The planner's ability to bypass obstacles effectively is another demonstration of its robustness and adaptability. This capability, coupled with the planner's ability to near-optimize for wind and icing conditions, establishes the planner as a practical solution for path planning in this environment.

### 9.1.2 Test case 2

In exploring the work of the path planner in artificial environment 2, two specific icing conditions were evaluated, -6°C and -20°C. Both trajectories from the path simulations are shown in figure 8.3.

When the environmental temperature was set at -6°C, the path planner chose a path that circumvented the area prone to icing entirely. It is worth noting that the path planner chose the northern path, involving incline and decline, instead of a southern path through the region with strong winds. This decision indicates that the weather conditions led to control surface saturation, and the path planner effectively avoided that area. Contrarily, when the temperature is lowered to -20°C, the path planner took a notably different path, directing the UAV straight through the icing area. At this temperature with MVD 20µm, the LWC is 2.13 $g/m^3$, which is significantly lower than 5.1 $g/m^3$, which is the value at -6°C. It is clearly shown in figure 3.3 that the ice structure formed at -20°C forms a significantly smaller ice structure than at -6°C, which can be related to higher drag. This increase in drag can also be seen in figure 3.2.

These contrasting outcomes highlight the planner's capacity to evaluate the environment's complexity, consider the characteristics of different weather conditions, and plan a path accordingly. This ability to adapt to various weather conditions makes the path planner valuable for ensuring safe UAV operations.

### 9.1.3 Artificial environments test findings

A noteworthy aspect of this study is the comprehensive UAV model utilized for path simulation. This model allowed for the cost estimation to be based on a realistic energy consumption of the UAV model. This model incorporates detailed aspects like aerodynamic drag due to the wing and empennage and an experimentally processed propeller model. This focus on drag and energy consumption allows for a more nuanced cost estimation of the paths. However, it does not consider drag from the fuselage and other structures. Thus the total energy consumption would be higher if such drag was considered. Moreover, the advanced functionalities of the simulator further strengthen the reliability of the study as it accounts for crucial environmental factors like icing and winds. This level of sophistication leads to more accurate simulations, replicating a wide array of real-world weather conditions the UAV might encounter.

The complexity and certain degree of unpredictable nature of weather conditions, spanning a wide range of scenarios, pose significant challenges to effective path

planning. The RRT* path planner takes advantage of the simulated comprehensive Falk model. Rather than predicting the effect of various weather conditions on the flight path, the planner tests the model within these conditions to see if any control surfaces reach saturation. If this situation arises during a simulated path, that path is discarded as a feasible option. This process of testing and discarding problematic paths showcases the planner's dynamic problem-solving capabilities, demonstrating its adaptation to complex and unpredictable weather conditions. To further enhance this safety, adjusting the criteria for what constitutes a feasible path is possible, allowing a greater safety margin before control surfaces reach saturation. After discarding a potentially dangerous path, the planner evaluates alternative routes. This test-and-evaluation cycle dramatically reduces the risk of encountering problematic conditions but comes at the expense of time spent on simulation.

Exploring the RRT* path planner in artificial environments has provided the basis for further improvements. The most significant area of potential improvement lies in the path planner's handling of different types of icing. In the concept testing, the path planner uses a simplified icing model, accounting for only one type of ice accumulation for each execution. However, in reality, ice accumulation can vary greatly depending on numerous factors, including temperature, LWC, and MVD. Implementing an icing model that calculates which type of ice accumulates based on weather data will be a manageable task. Nevertheless, both the UAV model and simulator have demonstrated their ability to simulate flights under *various* icing conditions. However, they cannot simulate flights under *varying* icing conditions. In reality, the weather can vary within a specific area, and flying through such an area could result in an icing formation being a mixture formed by multiple different icing conditions.

Another notable observation in exploring the path planner's functionalities is its inherent constraint in encountering broad areas of icing conditions. Specifically, when the icing area in an environment is too vast, the path planner may need help finding a feasible path. This leads to a potential improvement that involves the inclusion of an ice protection system (IPS). It is essential to consider that relying solely on a path planner to avoid icing conditions may not always be feasible. Unpredictable weather conditions and mission locations may expose the UAV to weather hazards. In such cases, having a backup IPS or a combination of path planning and IPS can provide additional safety and operational flexibility. If an IPS were to be incorporated into the path planner, the planner would need to account for the additional energy consumption of the system. Such a system is used in work [28] and [9], which are further investigated in [33].

There is also room for improvement in the efficiency of executing the path planner. Especially the way the path planner expands the RRT-tree by simulating every branch between nodes. The planner might simulate a flight between two nodes multiple times, even when the weather conditions are constant. Optimizing this process to perform a single simulation between two nodes and store the result could significantly reduce simulation time and computational load. However, it is essential to note that if the path planner is to be executed in real-time weather, the weather will most likely change dynamically during execution. Then multiple simulations between nodes might still be necessary to ensure the accuracy and safety of the flight path.

Another aspect that could enhance the performance of the path planner is considering the effect of air temperatures above 0°C. In such conditions, ice accumula-

tion on the UAV would likely reduce or even disappear. Incorporating this factor could lead to more effective flight paths, accounting for variations in weather conditions and their impact on ice accumulation. Furthermore, the effect of different cost models on the planner's decision-making process is worth investigating. In this study, the cost is primarily based on the UAV's energy consumption, but other factors, such as flight time or distance, could also be considered in future studies.

## 9.2 Real-World application of the path planner

The results in figure 8.4 provide insights into the practical application of the RRT* path planner in a real-world environment. By incorporating historical real-world weather data into the algorithm simulations, the path planner demonstrated its capability to search for paths in adverse weather conditions, including icing areas. This inclusion of real-world environmental factors strengthens the applicability of the path planner, offering a more realistic evaluation of its completion. The successful avoidance of icing hazards in the test underlines the practical value of the planner.

However, it is worth noting that the study's test case considered only one type of icing, limiting the complexity of the icing conditions the path planner had to face. Despite this limitation, including variable winds obtained from the actual weather data added another layer of legitimacy to the test, reinforcing the validity of the found path.

The choice of day to fetch historical weather data is a random day that had icing conditions in a specific area. That said, when the weather data was retrieved, it was never discovered that an icing area covered the entire environment.

One field that needs further development is the path planner's coordinate mapping. The planner operates in the cartesian xy weather data coordinates, explained in [9]. These coordinates need to be converted into latitude and longitude coordinates to plot the path on a map accurately. Due to this limitation, the plotted path on the map is an approximation in this test. Developing a method for converting the cartesian xy coordinates to latitude and longitude would enhance the practical usage of the path planner for real-world applications.

# Part III

# Conclusion and Further Work

# Chapter 10

# Conclusion

This thesis has provided an in-depth investigation into the effects of ice accumulation on a fixed-wing unmanned aerial vehicle (UAV) named Falk. The developed exhaustive mathematical model has been concluded to capture the most significant effects of ice accumulation on the UAV's performance.

The investigation of pitch and roll step responses and related aerodynamic variables has brought to light substantial variations in how different icing conditions affect the performance of the Falk. The characteristics of each icing condition influence stability margins and the behavior of control surfaces. The performance fluctuates depending on specific icing conditions and icing levels.

Furthermore, the results highlight that every icing scenario uniquely alters flight performance. The preferred iced scenario does also fluctuate based on specific icing conditions. This fluctuation indicates that comprehensive, situation-specific simulations are required if an ice protection system (IPS) is to be applied to airfoils individually.

All results imply that developing a universal rule to predict the impact of ice accumulation on flight performance may be challenging. Thus, the developed path planner using RRT* algorithm uses the extensive model to simulate its way toward a near-optimal path.

The model simulations facilitated the calculations of energy consumption and stability margins, which proved helpful in the search for the most energy-efficient path that ensures the UAV's safe arrival at its goal.

The path planner was tested in artificial and real-world environments, demonstrating its ability to effectively identify a safe, energy-effective path while avoiding weather hazards and obstacles. Setting constraints on the icing exposure time and control surface deflections demonstrates a practical approach to identifying a safe and feasible flight path.

## 10.1 Further Work

The most important improvements of this study are regarding the path planner. Some improvements to the path planner will increase its adaptability and practical usability. They are as follows:

- Path planner calculation of icing conditions. This will make the path planner adapt to a mission's different icing conditions.
- Conversion from cartesian xy-coordinates to lat/long coordinates for practical visualization of the path on a map.
- Implement a function that reduces airspeed if necessary. This can be done, for example, by flying with turns during descent.
- Explore the 3D search functionality of the RRT* algorithm. This can increase the algorithm's chances of finding a feasible path. It is important to be aware of aviation regulations if that function is to have practical value.

This thesis also suggests adding a new step to the RRT* algorithm. This step is intended to be implemented as a fourth step in the list from section 6.3.2, and will improve the algorithm.

- **Rewire the children's neighborhood** if any of the reduced-cost children serve a lower cost to any node in their neighborhood. This procedure is a recursive step of step 3 from section 6.3.2 with respect to the children's neighborhood. This step is done when all children's neighborhoods are evaluated.

# Bibliography


[1] R. Hann and T. Johansen, 'Unsettled topics in unmanned aerial vehicle icing,' *SAE EDGE Research Report*, 2022.

[2] M. Bragg, A. Broeren and L. Blumenthal, 'Iced-airfoil aerodynamics,' *Progress in Aerospace Sciences 41.5*, pp. 323–362, 2005.

[3] M. Robotics. 'The falk.' (), [Online]. Available: `https://www.maritimerobotics.com/falk`. (accessed: 05.6.2023).

[4] E. Skogan, 'Modelling and control of fixed-wing unmanned aerial vehicle in icing conditions,' *NTNU*, 2023.

[5] N. Müller, 'Uav icing: A performance model for a uav propeller in icing conditions,' *AIAA AVIATION 2022 Forum*, 2022.

[6] K. Gryte, 'High angle of attack landing of an unmanned aerial vehicle,' *MS thesis, NTNU*, 2015.

[7] R. Kleiven, 'Robust and gain scheduled flight control of fixed-wing uavs in wind and icing conditions,' *2022 IEEE Aerospace Conference (AERO)*, 2021.

[8] S. Högnadóttir, 'Inner-loop adaptive control of fixed-wing unmanned aerial vehicles in icing conditions,' *AIAA SCITECH 2023 Forum*, 2022.

[9] M. Tiller, T. A. Johansen and R. Hann, 'Path planning for fixed-wing uavs in wind and icing conditions,' *MS thesis, NTNU*, 2020.

[10] T. Olsen and M. Føre, 'Collision free path planning for operations in dynamically changing underwater environments,' *NTNU*, 2022.

[11] A. Winter, 'Systems identification, flight performance, and control of a fixed-wing uav in icing conditions,' *MS thesis, NTNU*, 2019.

[12] M. Lindner, 'Uav icing: Numerical simulation of icing effects on wing and empennage,' *No. 2023-01-1384. SAE Technical Paper*, 2023.

[13] S. E. Bansmer, 'Aircraft icing - a challenging problem of fluid mechanics,' 2020.

[14] R. W. Beard, *Small Unmanned Aircraft*. Princeton University Press, 2012, ISBN: 978-0-691-14921-9.

[15] M. V. Cook, *Flight Dynamics Principles* (Elsevier Aerospace Engineering Series). Elsevier Ltd., 2007, ISBN: 978-0-7506-6927-6.

[16] W. F. Phillips, *Mechanics of Flight*. John Wiley & Sons, 2004, ISBN: 0-471-33458-8.

[17] N. Fezans, 'A model of horizontal tailplane damage for use in flight dynamics,' *International Congress of the Aeronautical Sciences (ICAS)*, 2012.

[18] B. W. McCormick, *Aerodynamics, Aeronautics, and Flight Mechanics*. Wiley, 1994, ISBN: 978-0-471-57506-1.

[19] E. Coates, 'Propulsion system modeling for small fixed-wing uavs,' *2019 International Conference on Unmanned Aircraft Systems (ICUAS)*, 2019.

[20] B. Prasad and P. S., 'Automatic landing system design using feedback linearization method,' *AIAA infotech@ Aerospace 2007 conference and exhibit*, 2012.

[21] T. I. Fossen, *Handbook of Marine Craft Hydrodynamics and Motion Control*. John Wiley & Sons, 2011.

[22] U. of Illinois in Urbana-Champaign. 'Uiuc airfoil coordinates database.' (), [Online]. Available: `https://m-selig.ae.illinois.edu/ads/coord_database.html`. (accessed: 19.12.2022).

[23] Y. J. Hasan and F. Sachs, 'Preliminary design study for a future unmanned cargo aircraft configuration,' *CEAS Aeronautical Journal*, pp. 5–6, 2018.

[24] D. A. Caughey, 'Introduction to aircraft stability and control course notes for m&ae 5070,' 2011.

[25] N. U. I. Lab. 'People.' (), [Online]. Available: `https://uavicinglab.com/people/`. (accessed: 8.05.2023).

[26] B. Etkin, *Dynamics of Flight*. John Wiley & Sons, 1996, ISBN: 0-471-03418-5.

[27] J. Bertin, *Aerodynamics for Engineers*. Pearson Education, 2009, ISBN: 978-0-13-235521-6.

[28] E. Narum, R. Hann and T. A. Johansen, 'Optimal mission planning for fixed-wing uavs with electro-thermal icing protection and hybrid-electric power systems,' *2020 International Conference on Unmanned Aircraft Systems (ICUAS)*, 2020.

[29] A. R. Hovenburg, 'Flight performance optimization for small unmanned aerial vehicles using path planning methods,' *Ph.D. dissertation, NTNU*, 2019.

[30] S. LaValle, 'Rapidly-exploring random trees: A new tool for path planning,' 1998.

[31] Y. Guo and X. Liu, 'Fc-rrt*: An improved path planning algorithm for uav in 3d complex environment,' *ISPRS International Journal of Geo-Information 11.2*, 2021.

[32] L. Wei, Z. Zheng and C. Kaiyuan, 'Adaptive path planning for unmanned aerial vehicles based on bi-level programming and variable planning time interval,' *Chinese Journal of Aeronautics 26.3*, pp. 646–660, 2012.

[33] M. Cheung, T. A. Johansen and R. Hann, 'Energy consumption model route planning for an uav with electro-thermal icing protection system,' *MS thesis, NTNU*, 2021.

# Appendix A

# Falk Specifications

## A.1 Chord locations and lengths

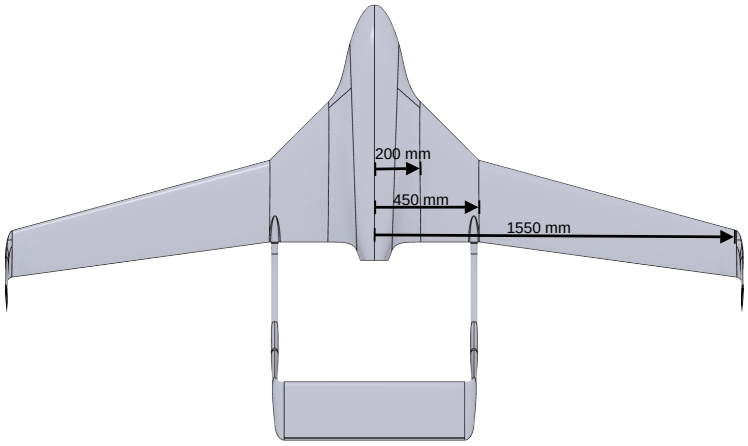


**Figure A.1:** Illustration that shows the length from the longitudinal axis to the chords

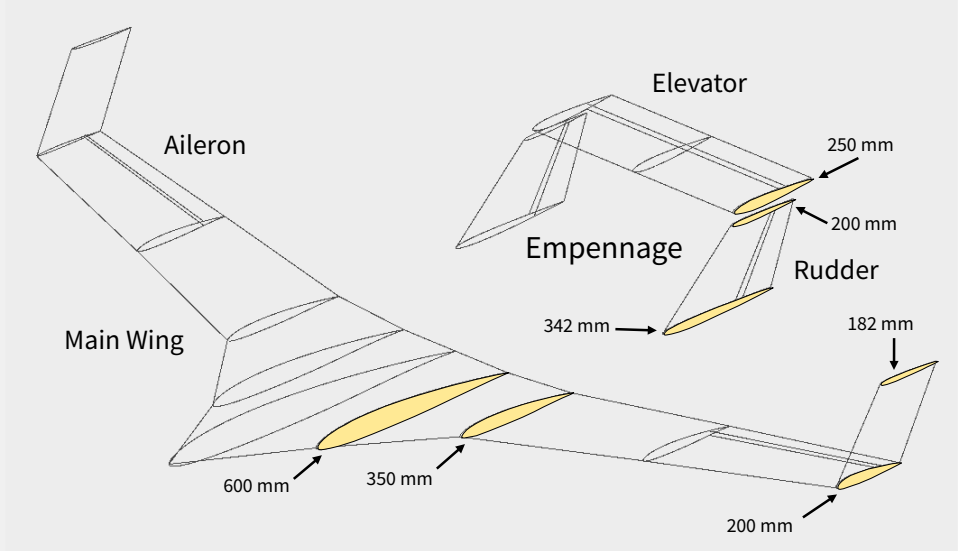


**Figure A.2:** Illustration that shows chord lengths of Falk

## A.2 Specifications table

| | | | |
|---|---|---|---|
| **Main wing** | Shaping | Airfoil | RG-15 |
| | Geometry | Dihedral | 4° |
| | | Tilt | 4° |
| | | Planform area [$m^2$] | 1.227 |
| | | Span [m] | 3.1 |
| | | Sweep | 18° |
| | | Aspect ratio | 8 |
| | | Taper ratio | 0.57 |
| | | Mean chord [mm] | 312 |
| | Control surface | Chord ratio | 0.24 |
| | | $\delta_{max}$ down | 17.5° |
| | | $\delta_{max}$ up | 12.3° |
| **Horizontal tail plane** | Shaping | Airfoil | SD8020 |
| | Geometry | Dihedral | 0° |
| | | Tilt | 1.5° |
| | | Planform area [$m^2$] | 0.195 |
| | | Mean chord [mm] | 250 |
| | Control surface | Chord ratio | 0.32 |
| | | $\delta_{max}$ down | 17.0° |
| | | $\delta_{max}$ up | 11.9° |
| **Vertical tail plane** | Shaping | Airfoil | SD8020 |
| | Geometry | Planform area [$m^2$] | 0.110 |
| | | Mean chord [mm] | 271 |
| | Control surface | Chord ratio | 0.30 |
| | | $\delta_{max}$ right | 15.0° |
| | | $\delta_{max}$ left | 15.0° |

**Table A.1:** Important specifications and geometry of Falk.

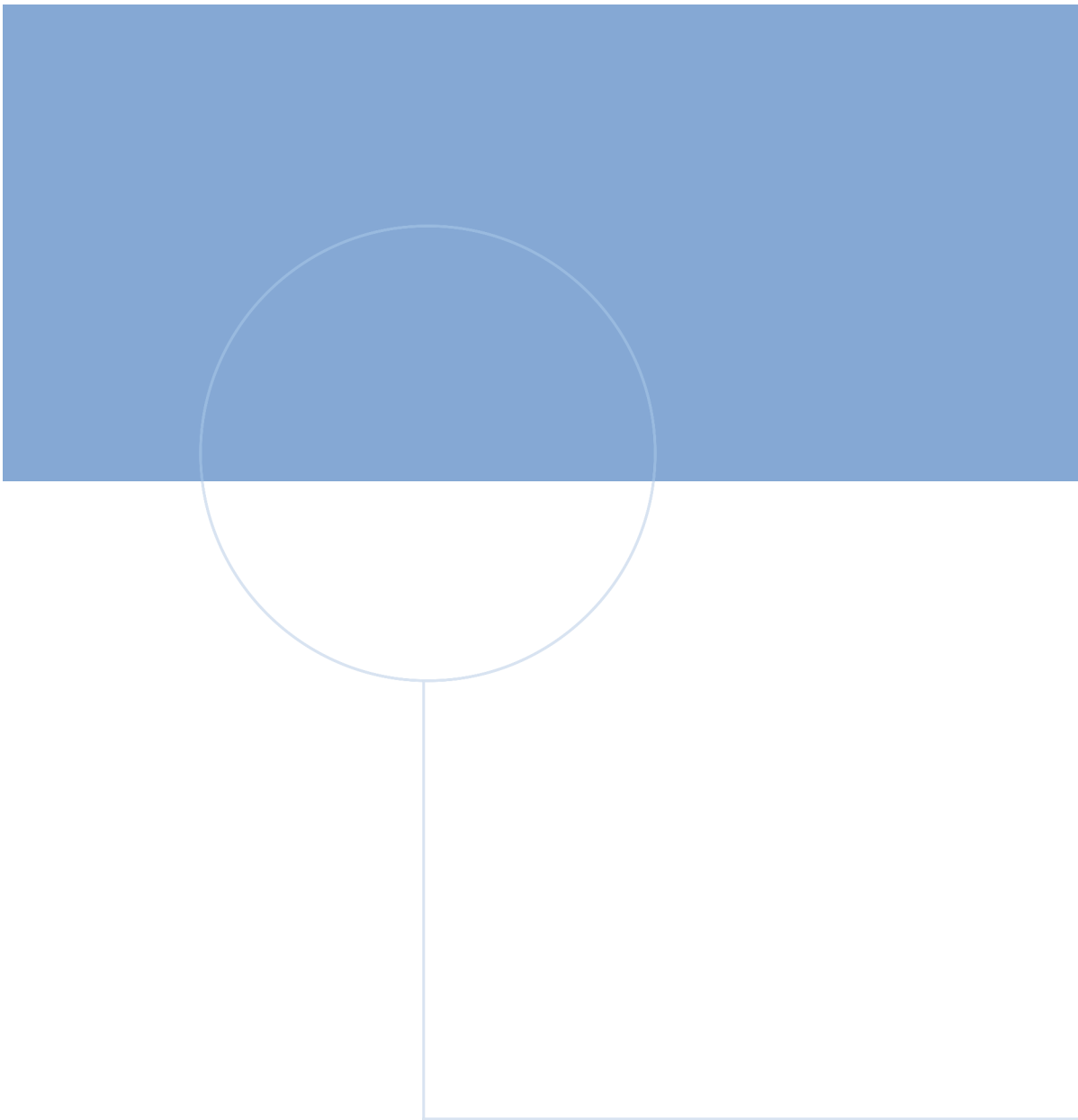

NTNU

Norwegian University of
Science and Technology